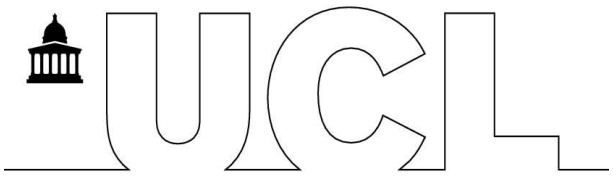

A high-accuracy synthetic H_2O line list: computation and applications.

A Thesis submitted for the Degree of:
Doctor of Philosophy of the University of London

Robert J Barber

September 2006

Department of Physics & Astronomy
University College London
University of London

I Robert John Barber, confirm that the work presented in this thesis is my own. Where information has been derived from other sources, I confirm that this has been indicated in the thesis.

'Eppur si muove'

This work is dedicated to all those who have suffered incarceration, torture, death or other persecution on account of their sex, colour, race, religion, or for holding beliefs that are counter to the accepted norm.

Hail, holy Light, offspring of Heav'n first born,
Or of th' Eternal co-eternal beam
May I express thee unblam'd? since God is light,
And never but in unapproachéd light
Dwelt from Eternitie, dwelt then in thee,
Bright effluence, of bright essence increate.

John Milton: Paradise Lost, Book III

'This is the best of me; for the rest I ate, and drank, and slept, loved and hated, like another: my life was as the vapour and is not; but this I saw and knew: this, if anything of mine, is worth your memory'

Sir Edward Elgar: August 13 1900, on finishing 'Dream of Gerontius'.
It is a quote from John Ruskin's 'Sesame and Lilies'.

Acknowledgements

The four years spent in carrying out the research that I now present for your approval represent the most sustained period of intellectual effort of my life, which is now in its sixtieth year. I have been fortunate, for the work has been engaging, and stimulating, and I have been rewarded by the knowledge that the BT2 line list is a valuable tool for astronomers and experimentalists. However, only great men can reach the heights unaided, and I make no claim to have trodden a solitary path.

First and foremost I have received moral support from my wife, Marie-Christine. She has also been unstinting in her financial support, continuing to work in the City at a time when the stresses and tedium of that world were taking their toll on her spirits. Only now has she turned her back on that life. I thank her with all my heart.

I have also been fortunate and privileged to have had as my Supervisor, Professor Jonathan Tennyson. His unequalled knowledge of molecular spectroscopy has enabled him to answer my very many questions, but even more important, he has provided motivation and injected a sense of direction and purpose into my work. He has also fostered a freedom of approach that is an essential ingredient in original research.

Thanks are also due to those people, outside UCL, with whom I have collaborated. I am particularly grateful to those colleagues who have allowed the line list to be applied within their particular areas of investigation. Their generous spirits have enabled us to demonstrated the accuracy and capabilities of BT2, and so have paved the way for its wider use. I hope, that through having had access to BT2 data, they too have derived some benefit from these collaborations. They are, in alphabetical order:
N.M. Ashok, D.P.K. Banerjee, P.F. Bernath, B.P. Bonev, N. Dello Russo,
M.A. DiSanti, P. Hauschildt, H.R.A. Jones, H. Kawakita, Y. Lyubchik, M.J. Mumma,
Y.V. Pavlenko, V.V. Smith, N.F. Zobov.

Amongst my many colleagues at UCL, the I would like to thank two friends: Greg

Harris, who has provided sound advice on matters relating, *inter alia*, to astronomy and quantum mechanics, and James Munro, who has provided invaluable assistance in solving very many problems related to computers.

Finally, I wish to thank my examiners, Professor Peter Sarre of the University of Nottingham and Dr. Serena Viti of University College London, for their careful reading of this Thesis, and for their decision to accept it as submitted, without correction.

Abstract

The subject matter of this Ph.D. thesis is the production and application of the Barber-Tennyson line list, BT2, a computed list of $H_2{}^{16}O$ transition frequencies and intensities. BT2 was produced using a discrete variable representation two-step approach for solving the rotation-vibration nuclear motions (Tennyson et al., 2004, Comp. Phys. Comm., 163, 85). It is the most complete water line list in existence, comprising over 500 million transitions (~65% more than any other list) and it is also the most accurate (over 90% of all known experimental energy levels are within 0.3 cm^{-1} of the BT2 values). Its accuracy has been confirmed by extensive testing against astronomical and laboratory data.

The line list has already found application in a wide range of astrophysical environments. It has been used to identify individual water lines in: the spectra of comets, sunspots, cool stars, brown dwarfs and the enigmatic object V838 Mon, and in a number of cases physical parameters have been derived from the intensities of the lines. The line list has also been used to model the atmospheres of cool stars and brown dwarfs and the chemistry of the circumstellar molecular shell ejected by V838 Mon.

In addition to our own work with BT2, we have supplied various data, derived from BT2, to other astrophysical research groups including: N. Dello Russo and co-workers for cometary applications; J.M.C. Rawlings for modelling the time-dependent chemistry of the shell ejected by V838 Mon; and P. Hauschildt's stellar atmospheric modelling group, which has included the complete BT2 line list in its 'PHOENIX' database.

Practical applications of BT2 are not confined to the field of astronomy. The line list is now the preferred reference tool for many groups engaged in the identification of water lines in high temperature laboratory torch spectra, and we have been pleased to supply them with appropriate BT2 spectral data.

The final chapter of the thesis looks to the future, which includes further applications of BT2 and the production of an NH_3 line list.

Contents

List of Tables

List of Figures

Chapter 1

Introduction

Water is the third most abundant molecule in the universe after H_2 and CO. It is present in many astrophysical environments including the atmospheres of: M dwarfs (Allard et al., 1994), brown dwarfs (Allard et al., 1996), K and M giants and supergiants (Jennings and Sada, 1998; Ryde et al., 2002; Tsuji, 2001) and oxygen-rich AGB stars (Barlow et al., 1996). It occurs in: sunspots (Wallace and Livingston, 1992; Polyansky et al, 1997c), the 'nova-like' object V838 Mon (Banerjee et al., 2005), Mira variables (Hinkle and Barnes, 1979), T Tauri eruptive variables (Shiba et al., 1993), dark molecular clouds (Gensheimer et al., 1996), young stellar objects (Carr et al., 2004), comets (Mumma et al., 1996; Dello Russo et al., 2000), the ISM (Cernicharo et al., 1994), masers (Cheung et al., 1969; González-Alphonso et al., 1995) and planetary atmospheres. An accurate water line list is thus essential for interpreting spectra from all of these sources and in modelling stellar atmospheres up to 4 000 K.

The importance of water has given rise to many laboratory investigations of its spectrum. Ludwig (1971); Camy-Peyret et al. (1977) and Bernath (1996), all investigated hot water line positions. However, technical problems and the huge number of transitions (many of which appear blended) mean that only in the region of 80 000 (out of a total of more than a billion) transitions are known experimentally and there are few hot water lines for which intensities have been determined.

The spectrum of water, which extends over a wide wavelength range from the near ultra-violet to the sub-millimetre, is the result of a huge number of transitions between the quantised ro-vibration energy states of the atomic nuclei moving in the electronic potential well. In most astrophysical environments water molecules only exist in the ground electronic state, since the energy of the first stable excited electronic state is above the dissociation energy of the molecule. However, in rar-

efied environments, some higher energy absorptions by short-lived excited electronic states are possible. The detection of ultra-violet water absorption lines in diffuse interstellar clouds is suggested by Smith et al. (1981), and they provide wavelengths, oscillator strengths and detection limits.

Water is a triatomic asymmetric top molecule and in common with other non-linear triatomics, H_2O, classically, has six degrees of internal freedom (three of rotation and three of vibration). However, the rotation-vibration spectrum of water is more complicated than those of most other triatomic molecules. The lightness of the hydrogen atoms means that the rotation constants are large, and this gives rise to an open spectrum that extends over a wide frequency range. Moreover, the 'floppy' nature of the molecule means that the movement of the hydrogen atoms is generally anharmonic and consequently transitions involving changes of more than one vibrational quanta often occur. Also, since many of the energy levels are nearly resonant with other levels, it is common for vibrational bands to overlap and for states to interact in ways that cannot easily be predicted by perturbation theory.

The importance of the H_2O molecule in astronomy and the complexity of its spectrum have created a great deal of interest in the possibility of generating the spectrum synthetically. Previous synthetic line lists are discussed in Section 3.5.1 and include: MT (Miller et al., 1994), VT1 (Viti et al., 1997), VT2 (Viti, 1997), PS, otherwise called AMES, (Partridge and Schwenke, 1997) and SCAN (Jørgensen and Jensen, 1993; Jørgensen et al. 2001).

All previous synthetic line lists have been incomplete and inaccurate, which has limited their usefulness in astronomical applications (Polyansky et al, 1997a, 1997b; Allard et al., 2000; Jones et al., 2002). The most successful attempts have employed similar variational nuclear motion procedures to that used in producing the Barber-Tennyson water line list, BT2, that is the subject of this Ph.D. thesis. However, for reasons discussed in Chapter 3, none of the earlier lists is considered to be satisfactory: BT2 also suffers from inaccuracies, and certainly for transitions involving highly excited states does not achieve $\sim$0.02 cm^{-1} 'spectroscopic' accuracy. However, this is less of a criticism than may appear to be the case at first sight, as high resolution astronomical spectra in the near infrared are only accurate to $\sim$0.05 cm^{-1} and the combined effect of Doppler and pressure broadening, which in the case of laboratory torch spectra at 3 000 K typically amounts to $\sim$0.15 cm^{-1}, also prevents accurate experimental determination of line positions. BT2 represents a major improvement on all previous line lists and, unlike the earlier lists, it is sufficiently complete and accurate to enable it to find widespread application in astronomical spectroscopy, stellar atmospheric modelling and in laboratory investigations.

Chapter 2

Synthetic spectra

The practical limitations on experimentally obtaining the huge amounts of data that are required by astronomers working with high resolution spectra, or involved in stellar atmospheric modelling mean that workers in these fields are largely dependent on 'synthetic', that is to say, computed, molecular spectra. The current chapter is in two parts. Section 2.1 is an introduction to the techniques employed in the production of synthetic line lists and Section 2.2 describes how the DVR3D suite of programs (Tennyson et al., 2004) was used to generate the BT2 water line list.

2.1 Techniques

2.1.1 Introduction

An atom consists of a nucleus surrounded by one or more electrons. Quantum mechanically, the system is described by the Schrödinger equation. However, apart from the simplest cases: the hydrogen atom and single electron ions such as He^+, this equation defies exact solution.

Molecules are much more complex systems than atoms, and in order to render the equations of motion tractable it is normal to adopt the Born-Oppenheimer approximation (Born and Oppenheimer, 1927; Bernath, 2005), and we have done so in producing BT2.

The Born-Oppenheimer approximation assumes that the wavefunction for the complete atom/molecule may be separated into two parts: nuclear and electronic, and that these may be considered independently. This is justified since the mass of the electrons is small compared to that of the nuclei, and the electrons may be assumed to adjust their positions instantaneously in response to any change in the nuclear geometry. Consequently, at any instant in time, the electronic potential

well within which nuclei are moving may be assumed to be independent of earlier geometries, and only a function of the nuclear configuration at that time.

Within the Born-Oppenheimer approximation the total wavefunction, Ψ, is therefore written:

$$\Psi = \psi_n \times \psi_e \tag{2.1}$$

where ψ_n and ψ_e are the nuclear and electronic wavefunctions respectively.

The Hamiltonian can also be separated into nuclear and electronic parts:

$$\hat{H} = \hat{T}_n + \hat{H}_e \tag{2.2}$$

where $\hat{T}_n$ is the nuclear kinetic operator and $\hat{H}_e$ is the electronic operator.

The electronic potential energy can be determined at any given nuclear geometry. If many nuclear geometries are studied, an effective electronic potential energy surface (PES) can be calculated and fitted.

It is normal to treat the rotational and vibrational motions separately (ignoring Coriolis coupling). Most approaches adopt the rigid rotor approximation for rotational motion and the harmonic approximation for vibrational motion.

Despite the simplification introduced to the computations by invoking the Born-Oppenheimer approximation and the use of the rigid rotor and harmonic oscillator models, the computations of the wavefunctions and ro-vibrational eigenvalues for nuclear motion on the PES can be extremely demanding in terms of computer time, and in addition the methodology outlined above introduces errors which need to be eliminated as far as is possible by making a number of *ab initio* corrections (Schwenke, 2001). These include: adiabatic, non-adiabatic and relativistic correction, some of which involve adjustments to the PES, and others are affected by modifications to the program used to solve the Schrödinger equation (see Section 2.2.4).

A variety of approaches have been adopted by different researchers, with varying degrees of success. We now describe several of these methods.

2.1.2 Perturbation techniques

In perturbation theory (Hoy et al., 1972), the full Hamiltonian is assumed to be, within a small perturbation, the same as a Hamiltonian with known solutions.

$$\hat{H} = \hat{H}_0 + \alpha\hat{H}' \tag{2.3}$$

where α is a constant of small value, $\hat{H}$ is the full Hamiltonian, $\hat{H}_0$ is the Hamiltonian with known solutions and $\hat{H}'$ is the perturbing Hamiltonian. The accuracy of the method is determined by the ability to select a known Hamiltonian, $\hat{H}_0$, that approximates closely to $\hat{H}$, so that the required perturbation, $\alpha\hat{H}'$, is small.

As indicated in Section 1, harmonic oscillator functions are frequently used for the unperturbed vibrational component of the nuclear motion (here the potential varies as the square of the displacement from the equilibrium position) and the small perturbations are represented by higher order terms. This can be a good approximation at low energies, but increasingly breaks down at higher energies. Similarly, rigid rotors are used to describe the unperturbed rotational motion. For all rotational motion, the Hamiltonian is proportional to the square of the total angular momentum, and inversely proportional to the moment of inertia of the molecule. In nature, these two parameters are mutually dependent, since rotational distortion alters the moment of inertia. However, under the rigid rotor approximation, the moment of inertia does not vary. Small perturbations are therefore introduced to account for the fact that the molecule is not rigid, but distorts due to the stretching of the bond by centrifugal (rotational) and also vibrational forces. For higher ro-vibrational states, the perturbations required to describe the system are no longer small, and hence perturbation theory fails in these cases. This is a major problem for H_2O for those ro-vibrational states having J>7. In addition, perturbation techniques are not able to take account of the resonances between ro-vibrational energy states, mentioned in Chapter 1. However, these interactions, which arise from Coriolis couplings are included naturally in variational calculations (see below) based on the use of exact nuclear motion kinetic energy operators (Polyansky et al., 1999).

2.1.3 Variational techniques

The failure of perturbation techniques to adequately describe systems with large amplitude motion led to the adoption of variational approaches. These aim at exact solutions to the full nuclear motion Hamiltonian.

The Variational Principle states that the energy expectation values of the approximate eigenvalue solutions are always higher than the exact solutions.

The Variational Principle is able to be usefully applied in a number of different approaches, including finite basis representation (FBR) and discrete variable representation (DVR), even though the latter is not strictly variational. In both FBR and DVR, which are described below, the wavefunctions are expanded in terms of a basis set (the nature of these basis sets differing in the two methods). In accordance with the Variational Principle, the most accurate eigenvalue solutions are computed

using those sets of constants which, when applied to the basis set, yield values that are local minima.

In theory, this method is capable of delivering exact solutions for the full nuclear motion Hamiltonian. In practice, however, limitations on computing time mean that the computed eigenvalues are always approximations. In the case of water, variational techniques are capable of providing very accurate solutions, and this part of the calculation introduces negligible error into the results presented below.

2.1.4 Finite basis representation.

In a finite basis representation the wavefunctions are expressed in terms of a 'basis' set, of orthonormal functions.

The expression for each wavefunction takes the form:

$$\psi = c_1\phi_1 + c_2\phi_2 + c_3\phi_3 + ... + c_n\phi_n$$

The values c_i in the above expression are adjusted in order to minimise the eigenvalues, and it follows from the Variational Principle that these minima eigenvalues are the most accurate ones obtainable from this basis.

The computing time required to diagonalise the Hamiltonian matrix increases as the cube of the number of terms in the basis set, and hence there must be a trade-off between accuracy and computing time. Moreover in practice only a small proportion ($\sim$5%) of the solutions obtained by diagonalising the Hamiltonian matrix are of any significance and so due to the demands on computing time, FBR methods perform poorly when a large number of energy levels are required (Tennyson, 1992).

2.1.5 Discrete Variable Representation

The Discrete Variable Representation (DVR) is a more elegant way of defining wavefunctions and it has been comprehensively reviewed by Bačić and Light (1989). Instead of expressing the wavefunctions as weightings to a basis set of orthonormal functions, each wavefunction is expanded in terms of a set of discrete, weighted, Gaussian quadrature points in three dimensional space. This greatly simplifies the diagonalisation of the 3D Hamiltonian, which can be performed in several steps with 1D and 2D Hamiltonians being diagonalised first. This process reduces the size of the 3D Hamiltonian. Moreover, in DVR, the potential matrix elements are diagonal (the quadrature approximation - Dickinson and Certain, 1968), and hence are easily evaluated. Even more important for this work is the fact that the dipoles can be reduced to a similar form (Tennyson et al., 2004).

DVR is capable of generating accurate solutions, the accuracy being determined by the number and appropriateness of the points. It is efficient for a large number of situations.

The current work is not unique in employing a DVR approach to solve the nuclear motion problem for water (see for example, Viti et al., 1997). However, improved physics, in the form of a highly accurate PES, the methodology embodied in the DVR3D program suite (Tennyson et al., 2004), and increases in computational power have made it possible to produce a line list that is more complete and more accurate than any previous list, even those employing similar methodologies.

2.2 The DVR3D suite

The DVR3D suite of programs was developed by Tennyson et al. (1995), and has been subject to subsequent improvement. The latest version is Tennyson et al. (2004). It calculates the bound rotation-vibration energy levels, wavefunctions, and dipole transitions, for the rotation vibration nuclear motion of triatomic molecules. The final part of the DVR3D suite is a Fortran program, spectra-BT2.f90, that is able to compute temperature-dependent spectra over any selected frequency range, convolved with either the natural line width or some other selected width, such as that given by the resolving power of a particular spectrometer. DVR3D uses an exact (within the Born-Oppenheimer approximation - see Section 2.1.1) kinetic energy operator, and in the case of the PES used for BT2 (see Section 2.2.4), makes allowance for the failure of this approximation.

It uses a DVR with two radial and one angular co-ordinate for the nuclear motion problem (vibrational and rotational motions being treated separately). It offers a choice of Jacobi or Radau internal co-ordinate systems. The latter is the one more suited to ro-vibrational computations for H_2X systems, and Tennyson and Sutcliffe (1982) demonstrate that the discrete variable representation of the angular co-ordinate makes it possible to avoid singular regions of the Hamiltonian. Consequently Radau co-ordinates were used for generating BT2.

Prior to being used to compute BT2, the suite (or earlier versions) had been successfully used to calculated ro-vibrational line lists for H_3^+ (Neale et al., 1996), H_2O (Viti, 1997), HCN/HNC (Harris, 2002). However, the current work represents the most extensive application of DVR to-date. The previous largest line list that had been computed using DVR3D was that for HCN/HNC, which contained only 57% of the energy levels and 67% of the number of transitions.

There are four modules in the DVR3D suite that are important for this work:

- DVR3DRJZ calculates the Coriolis de-coupled vibrational wavefunctions,that are the starting point for the computation of the full ro-vibrational wavefunctions. Each run of this module computes these wavefunctions for one vibrational symmetry block 'q' (see Table 2.5).

- ROTLEV3Z performs the rotational part of the computation for a specified J. It takes as its input the first stage, wavefunctions computed by DVR3DRJZ. Its output is the full ro-vibrational wavefunctions and eigenvalues for the specified J. Each ROTLEV3Z run is for a single 'q'. It computes values for both rotational parities 'p', for this 'q'. Consequently, with the exception of J=0, which only has even vibrational symmetry, each value of J requires two runs of ROTLEV3Z and DVR3DRJZ.

- DIPOLE3 takes the outputs of two ROTLEV3Z runs and calculates the Einstein A coefficients for every allowed dipole transition. The combined output of all the possible DIPOLE3 runs is the water line list. For ease of presentation, in the case of BT2, this it is organised into two files (see Tables 3.1 and 3.2) that together contain a total of 12.6 Gb of data.

- Spectra-BT2.f90 takes as its input the BT2 line list and calculates the temperature-dependent spectrum over any selected frequency range, convolved with either the natural line width or some other selected line width.

The first stage of the computation, DVR3DRJZ, requires an accurate PES (see Section 2.2.4) and DIPOLE3 requires a dipole moment surface (DMS) (see Section 2.2.5). In addition, in order to be able to perform ro-vibrational calculations, DVR3D requires values to be specified for a number of computational parameters, detailed below, which are empirical in nature. These are dependent upon the PES being used and are unique to the molecule being investigated. The accuracy of the computed eigenvalues is dependent on the choice of these parameters, particularly so at high ro-vibrational energies.

2.2.1 The eight computational parameters

Eight parameters must be specified before DVR3D can be used to generate a line list using Radau co-ordinates. Their values are determined empirically using trial runs and testing the results for convergence. The accurate identification of the optimum values for these numbers (see Section 2.2.2) is essential in order to achieve the correct balance between computational time and the accuracy of the results.

Once established, the values of these parameters are held fixed for the whole of the line generating process.

Five of these parameters are used to determine the DVR basis grid points on which the wavefunctions will be defined. These parameters must be entered into the first module, DVR3DRJZ, of the DVR3D suite,

A Radau grid is defined by two radial co-ordinates and one angular co-ordinate. Symmetry considerations require that the points in each radial co-ordinate are the same. Section 2.2.2 outlines the methodology used to determine the number of points in the grid for each co-ordinate. The optimum value for n_r, the number of points for each radial co-ordinate, was found to be 28 and the optimum number of angular points, n_θ, was identified as being 44.

The 44 angular grid points are defined in terms of a basis set of associated Legendre polynomials. However, the two sets of 28 radial grid points are defined in terms of a Morse oscillator-like basis set, specified in terms of r_e, ω_e and D_e. These three parameters have physical counterparts which are respectively: the equilibrium bond length, harmonic frequency and dissociation energy of the water molecule. However, the parameters in the Morse oscillator function are purely empirical and differ from the physical values. The values selected were $r_e = 2.05$, $\omega_e = 0.008$ and $D_e = 0.20$, atomic units.

In contrast to the number of grid points which have a major effect on computational times, the values selected for r_e, ω_e and D_e have no such effect, but they are fundamental to the accuracy of the results.

In addition to these five basis parameters, three additional values need to be determined. These affect the number of eigenvalues generated and also their accuracy (within the constraints imposed by the selection of basis functions). These parameters are:

- NVIB: the number of vibrational levels to be retained from the first stage calculation, performed using DVR3DRJZ, for use in the second stage calculation, which uses the rotation module ROTLEV3Z.

- n_H: the maximum dimension of the largest intermediate 2-dimensional Hamiltonian, diagonalised in DVR3DRJZ.

- IBASS: the size of the final stage Hamiltonian that is diagonalised in ROTLEV3Z. It is related to the rotational quantum number J and the rotational parity, p, by: IBASS = m×(J+1-p). The value of the constant m must be less than NVIB. If m is too small, too few of the first step solutions are used in the second stage of the calculation, and the eigenvalues will be poorly converged.

Table 2.1: Extract from the convergence testing log for the determination of values for the Morse oscillator-like basis parameters. n_r, n_θ, are 30 and 44 respectively. n_H is 1 500 throughout. Here r_e and ω_e are 2.10 and 0.01 respectively, and D_e is varied. Σ is the sum of the first 251 eigenvalues in cm^{-1} for J=0, symmetry block 1.

D_e	Σ
0.15	5 536 316.05
0.25	5 536 304.24
0.30	5 536 308.90

2.2.2 Determining the parameters

The methods employed to determine the 5 basis parameters and IBASS are similar and are covered by the general term 'convergence testing'.

Logically, the first parameters to be fixed should be r_e, ω_e and D_e. However, we were fortunate in having the values used by Viti (1997) in computing VT2, which were $r_e = 2.55$, $\omega_e = 0.25$ and $D_e = 0.007$. These values were in fact the ones used by Fulton (1994) and which had been adopted by Viti. It was clear that these values would not be entirely appropriate for our work on BT2 as they are specific to the PES being used, and neither of these two authors had had access to the PES of Shirin et al. (2003), used in the current work. However, Fulton's values provided a useful starting point, and by initially adopting these for the Morse oscillator-like basis parameters, we were able to begin testing for the optimum values for n_r and n_θ

The method is based on the Variational Principle. Although, in principle, DVR3D is not strictly a variational method, in practice it is found that the Variational Principle does apply.

We ran DVR3DRJZ for J=0, symmetry block 1, (see Table 2.5 for an explanation of this coding), with varying values of n_r, keeping n_θ fixed at 40. The sum, Σ, of all the lowest 251 eigenvalues for this combination of n_r, n_θ was recorded. The process repeated until a value of n_r was found, above which there was no significant reduction in Σ. At this stage, n_r was held constant at the determined value and n_θ was altered until a value for this parameter was found, above which there was no significant reduction in Σ. It should be noted that only even values of n_θ are recommended for use in DVR3D. The values of n_r and n_θ, thus determined, were 30 and 44 respectively. However, these were not the final values, as the parameters are dependent on r_e, ω_e and D_e and these values had still to be determined accurately.

Once these 'preliminary' values of r_n and θ_n had been determined, it was possible to establish better estimates of r_e, ω_e and D_e, by holding r_n and θ_n and two of the

Table 2.2: Extract for the convergence testing log for the determination of values for the Morse oscillator-like basis parameters. n_r, n_θ, are 30 and 44 respectively. n_H is 1 500 throughout. Here D_e is set to 0.20 and the values of r_e and ω_e are altered. The values given are the amounts by which the sum of the first 251 eigenvalues for J=0, symmetry block 1, exceeds 5 530 000 cm^{-1}.

	ω_e		
r_e	0.005	0.010	0.020
2.00	3 457.4	6 344.8	11 511.6
2.05	3 094.5	6 327.4	9 713.1
2.10	3 957.3	6 303.2	8 630.9

three parameters: r_e, ω_e and D_e, fixed whilst altering the third until a value was obtained for this parameter, above which there was no significant reduction in Σ. In this manner, more accurate values were obtained for each of the parameters: r_e, ω_e and D_e. The process was then repeated in an iterative manner, obtaining improved values of r_n and θ_n and then r_e, ω_e and D_e until further iterations gave no change in any of these five basis parameters.

Table 2.1 is an extract from our convergence testing log which shows the effect of varying D_e, whilst holding the other parameters constant.

Table 2.2 is an extract from the same log, showing the effect of varying r_e and ω_e whilst holding the other parameters constant.

Table 2.3 is an extract from the part of the convergence testing log dealing with the final determination of n_r. With all the other parameters fixed (r_e, ω_e, D_e set to 2.05, 0.008 and 0.20 respectively, $n_H = 2\,000$ and $n_\theta = 44$), the sum of the first 251 eigenvalues for J=0, symmetry block 1, are listed for various values of n_r. A similar process was used to establish the optimum value for n_θ. Using this procedure, values of n_r and n_θ could be determined relatively easily. However, as will be seen from Table 2.3, the selection of n_r involved a compromise as the computation time rises very rapidly as this number is increased. A value of 33 for n_r would have given an improvement in accuracy (Σ for $n_r = 28$ is 1 part in a million higher than for $n_r = 33$). However, the extra computational time involved in using this higher value of n_r (68% for J=0, symmetry block 1) was considered too high a price for this very slight improvement in accuracy. Except for very highly excited states (see our comments on 'm' below), the compromise over n_r is the single most important factor contributing to convergence error.

In the case of n_θ, values between 40 and 70 were tested(the size of the intermediate Hamiltonian was increased in steps from 2 000 to 3 500 during this exercise to ensure that it was of an appropriate size for each separate computation). It was ob-

Table 2.3: Extract from the convergence testing log for the determination of the optimum value for n_r. n_θ is set to 44, and r_e, ω_e, D_e and n_H have the values 2.05, 0.008 0.20 and 1 500 respectively. Σ is the sum of the first 251 eigenvalues in cm^{-1} for J=0, symmetry block 1.

n_r	Σ
28	5 536 319.3
30	5 536 339.3
33	5 536 314.9
35	5 536 323.0

served that for eigenvalues less than 23 250 cm^{-1}, and to an accuracy of 0.001 cm^{-1}, there were essentially no differences between the eigenvalues computed with our selected value of n_θ=44 and n_θ=70. For energy levels above 23 250 cm^{-1}, increasing the value of n_θ did lead to lower eigenvalues. However, it was observed that even at these higher energies, the large differences (more than 0.4 cm^{-1}) were restricted to a few individual vibrational states, and most eigenvalues up to our cut-off of 30 000 cm^{-1} that were computed using n_θ=44 were within 0.1 cm^{-1} of the value that was computed using n_θ=70. Based on the sum of the eigenvalues of the 251 levels up to 30 000 cm^{-1} for J=0, symmetry block 1, the difference between the n_θ=44 and 70 cases was two parts in a million. However, the sum of all the differences for states up to to 25 000 cm^{-1} was only 0.15 parts in a million.

In practice, the process of determining r_e, ω_e and D_e was more difficult than might appear to be the case from this description of our methodology, since our investigation was complicated by the existence of local minima, that are not global minima for the three variables. Moreover, the eigenvalue solutions are particularly sensitive to r_e and ω_e. A difference of as little as 0.05 in the first of these two parameters and 0.002 in the second could affect the energy levels by in the region of 0.01cm^{-1} for states with energies of approximately 10 000 cm^{-1}. Larger deviations in these basis functions from their determined optimum values produced correspondingly greater errors and, in the case of states with energies over 20 000 cm^{-1}, a bad choice of parameters could easily result errors in the individual levels in excess of 20 cm^{-1}. The values determined for the Morse oscillator-like basis set were: r_e = 2.05, ω_e = 0.008 and D_e = 0.20, atomic units (the equivalent dissociation energy is 43 895 cm^{-1}).

By examining outputs, values were easily obtained for NVIB and n_H. NVIB was set at 700 (provided that this number is high enough to include all the vibrational states, it has no effect on convergence) and n_H was set to 2 500. Testing a selection of J =20 states, indicated that the choice of this value for n_H, rather than one much

larger one, only introduced an error of 1 part in 200 million. Computing time is largely independent of the choice of NVIB, but it rises slightly faster than the square of n_H. It was observed that for J=20, n_H = 2 500 took 1.8 times as long to compute as when the value was set at 2 000 and 3.4 times as long as when n_H was 1 500.

Establishing a correct value for IBASS is extremely important as high energy solutions are particularly sensitive to this parameter. Moreover, computing times are estimated to increase as the 2.5 power of IBASS. It was observed that values for IBASS that were satisfactory at low energies could give rise to large errors at high energies. For example a change of 50 in the value of 'm' was capable of producing errors of $\sim$ 3 cm^{-1} for some high energy solutions. The J = 20, symetry block 1, was tested making use of the Variational Principle in a similar method to the one employed above. 2 060 levels for 8 different values of 'm', between 280 and 600 were examined. We evaluated the accuracy of the 7 lowest m values compared to the eigenvalues computed using m = 600 (see Table 2.4), and determined the optimum value of m to be 530.

After computing BT2, an examination of the number of states that had been computed with energies in each 10 000 cm^{-1} energy band for each symmetry block of every value of J. This led to the conclusion that all the BT2 computed asymmetrical rotation states with J in the range 14−−20, had eignstates missing in the 29 000-30 000 cm−1 energy band. The total number of these missing states is estimated to be $\sim$450. The reason why these eigenstates were not computed is that the value of 530 for the parameter m had been established by testing at J=20, whereas the greatest number of eigenstates below 30 000 cm^{-1} occurs at J=18 (even vibrational and even rotational symmetries). Fortunately the absence of 450 levels at energies above 29 000 cm^{-1} is insignificant as far as the accuracy and completeness of the BT2 is concerned. However,it underlines the importance of performing the most rigorous testing possible in order to establish the correct computational parameters.

Finally, again using J=20, all of the six most sensitive parameters were re-tested and it was confirmed that the values selected held good at high energy solutions.

To summarise, in order to generate accurate eigenvalues, it is essential that the values of seven of the eight parameters listed in Section 2.2.1 are accurately determined. The results are not dependent upon the eighth parameter, NVIB, provided that, as discussed above, this is above a certain minimum value. The identification of these values involves rigorous testing based on the Variational Principle, or other methodologies that ensure that for each of the relevant parameters, the eigenvalues generated are fully converged within the limitations imposed by computing power and time.

Table 2.4: Extract for the convergence testing log for the determination of the optimum value for m, where m × (J+1-p) = IBASS. n_r, n_θ, are 28 and 44 respectively. n_H is 2 200. It illustrates the way in which the value of m required to achieve convergence increases with E. The values in the body of the table are the amounts by which the energy of a state, computed using various values of m deviates from the value of the same state computed using m=600.

	m			
E (cm^{-1})	300	350	460	580
15 000	0.0010	0.0004	0.0001	0.0000
20 000	0.0300	0.0100	0.0020	0.0005
25 000	0.4000	0.2000	0.0400	0.0080
30 000	6.0000	3.0000	0.7000	0.2000

The inaccuracy of earlier line lists has been mentioned in Chapter 1, and it can be demonstrated that in some cases lack of convergence is a major factor (Polyansky et al., 1997a). Earlier attempts to calculate a synthetic H_2O line list, using similar DVR techniques have used lower IBASS values. Viti et al. (1997), for example, used $300 \times (J + 1 - p)$, in computing VT2 and Partridge and Schwenke (1997), used an even lower effective value of 'm'. It follows that neither of these lists is capable of producing solutions for high energy ro-vibrational states.

It is estimated that for eigenvalues below 25 000 cm^{-1}, the choice of r_n=28 accounts for approximately half of the total convergence error, which is estimated to be less than 0.01 cm^{-1} at 10 000 cm^{-1} and in the region of 0.02 cm^{-1} at 20 000 cm^{-1}. At higher energies, the decision to use a value of m of 530 is probably the major source of convergence error (see Table 2.4).

2.2.3 Outputs

In common with FBR approaches, the DVR3D suite of programs generates four ro-vibration symmetry blocks for the H_2O molecule, which are here labelled ee, eo, oe and oo. The first e/o term in these labels is the vibrational basis symmetry 'q' and the second, e/o term is the quantum number 'p', the rotational parity (see Table 2.5). These symmetry blocks are related to the C_{2v}(M) symmetry blocks Γ_{rv}: A_1, A_2, B_1, B_2 (see Bunker & Jensen, 2005).

The nuclear permutation operation in which the two identical protons comprising the hydrogen nuclei are interchanged gives rise to two molecular spin states of the molecule. The nuclear spins may couple symmetrically or anti-symmetrically. The antisymmetric coupling that gives rise to the ortho (O) form of the H_2O molecule is triply degenerate, whilst the symmetric coupling, that gives rise to the para (P) form of the molecule is non-degenerate.

Table 2.5: Symmetry Blocks. q is the vibrational symmetry and p is the rotational parity. These are labelled as either symmetric (e), or antisymmetric (o) states. O/P = Ortho/Para. The 'Code' is the notation for symmetry used in the Levels File, Table 3.1.

	J even				**J odd**			
q	e	e	o	o	e	e	o	o
p	e	o	e	o	e	o	e	o
O/P	P	O	O	P	O	P	P	O
Code	1	3	4	2	3	1	2	4

For any J, apart from J=0, there are two ortho and two para symmetry blocks (in the case of J=0 there is one O and one P block). The blocks are related to specific combinations of: p, q and the odd or evenness of J, as shown in Table 2.5.

The difference in degeneracies of the O and P states impacts on the partition function of the molecule as well as on line intensity. Also, the fact that O-P and P-O transitions are, for all practical purposes, forbidden (Miani and Tennyson, 2004) has spectroscopic consequences.

2.2.4 PES and energy levels

The energies of the quantised ro-vibration states are the eigenvalue solutions that satisfy the Schrödinger equation for the oxygen and two hydrogen nuclei moving within the electronic potential well. As stated in Section 2.1.1, the problem is rendered tractable by adopting the Born-Oppenheimer approximation. However, in reality, the electronic potential within which the charged nuclei are moving is itself a function of the actual internuclear geometry, and in the absence of any adjustments, the best *ab initio* PES is only capable of predicting the vibrational fundamentals of the H_2O molecule to within about 2 cm^{-1} for lower vibrational states. The error increases rapidly for higher band origins (Partridge and Schwenke, 1997; Kedziora and Shavitt, 1997). One method of improving the PES is to use an *ab initio* starting point and adjust it empirically to fit the observed spectroscopic data to give, a 'spectroscopically-determined' potential (Sutcliffe and Tennyson, 1986). A PES produced in this manner is capable of achieving high accuracies by interpolation (Polyansky et al., 1994; 1996). However it is observed that when extrapolating to higher ro-vibrational states, these surfaces perform worse than do those produced by a purely *ab initio* approach (Polyansky et al., 1997b; 1999). Also they are better at predicting the energies of stretching modes than the bending modes (Sutcliffe and Tennyson, 1987).

In order to achieve higher accuracy it is necessary to make further adjustments,

either to the PES, or to the program used to generate the wavefunctions, to include a number of physical effects. We used the potential energy surface, fit B of Shirin et al. (2003), which takes as its starting point the *ab initio* Born-Oppenhimer surface of Partridge and Schwenke (1997), adjusted for electronic relativistic and adiabatic effects, a correction to the barrier to linearity and allowance for the Lamb shift. Non-adiabatic effects were treated within the program. Additional information on some of these adjustments is given below.

After applying these adjustments, the surface was fitted to the experimentally-determined H_2O levels of Tennyson et al. (2001). Despite being the most accurate surface in existence at the time, it is nevertheless the single most important factor affecting the the accuracy of the computed eigenvalues (moreso than the convergence errors detailed in Section 2.2.2).

Császár et al. (1998a; 1998b) showed that the electronic relativistic corrections are surprisingly large for H_2O. The effect of including relativistic corrections is to significantly improve the predictions for the stretching modes, but at the expense of worsening agreement with the bending overtones.

For water, the effects of the adiabatic correction (otherwise known as the Born-Oppenheimer diagonal correction) can be quite large (Tennyson, 2006a). Fortunately it is relatively easy to calculate this correction, which can be expressed as second derivatives of the electronic wavefunctions with respect to the nuclear displacement (Handy et al., 1986; Handy and Lee, 1996; Kutzelnigg, 1997).

In the case of water, non-adiabatic corrections to the Born-Oppenheimer approximation are also important, particularly as far as they affect higher J rotational motion (Zobov et al., 1996; Schwenke, 2003). The computation of these adjustments is difficult as it involves a knowledge of all the electronic states and necessitates the use of complicated differential operators containing sums over all the electronic wavefunctions (Barletta, 2002). Bunker and Moss (1980) made a detailed formulation of the non-adiabatic contributions to the ro-vibrational problem for triatomic molecules.

Fortunately, a full theoretical non-adiabatic adjustment to the PES has been shown to produce no significant benefits compared to simplified approaches (Tennyson et al., 2002). These authors examined two such approaches.

The first involved identifying the separate vibrational and rotational motions (different ways of identifying these led to different results) and then using separate reduced masses for the vibrational and rotational motions. This was found to systematically over-correct bending motions and under-correct stretches. It also had the effect of producing an extra term in the Hamiltonian when $\mu^V \neq \mu^R$.

The second approach involved a simplified version of the full correction, including only terms that scale with the kinetic energy terms in θ and r. The main adjustment is the inclusion of non-adiabatic effects for the rotational motion, and this is essential for reliable results at high J (Shirin et al., 2003).

The second approach enables adjustments to be effected through the DVR3D program rather than changes to the PES, and is the one used in this work.

Pyykkö et al. (2001) suggested that quantum electrodynamic Lamb shifts may contribute in the region of 1 cm^{-1} to the vibrational band origins and a similar amount to the $J = 20$ rotational levels, and the Shirin PES included adjustments for these effects.

Finally, it has been shown that spin-orbit interactions may be safely ignored, even in the region of linear geometries (Tarczay et al., 2001)

2.2.5 DMS and Intensities

The intensities of the allowed ro-vibrational transitions are determined by the dipole transition moments $\langle\psi'|\overline{\mu}|\psi''\rangle$ for these pairs of states, where ψ' and ψ'' are the wavefunctions of the two states, and $\overline{\mu}$ is the electronic dipole moment vector. In order to calculate transition intensities, it is normal to use a DMS (Sutcliffe, 1999).

The line strength, S_{if} of transitions between the initial, i, and final, f, ro-vibrational states (within the same electronic state), having angular momenta J′ and J″ respectively, is (Jensen, 1988):

$$S_{if} = (2J' + 1)(2J'' + 1)|\langle\psi'|\overline{\mu}|\psi''\rangle|^2 \tag{2.4}$$

The line strength is independent of temperature. In the SI system it has units of (Coulomb metres)^2.

The parameters computed by the DVR3D program suite include the Einstein A coefficient, A_{if}, for each transition. This is the coefficient of spontaneous emission between the upper and lower states. It is related to the dipole transition moment for the pair of states and to J for the upper state. A_{if} relates to a single molecule. It is independent of temperature, has units of s^{-1} and in SI units (Bernath, 2005, p. 142) is given by:

$$A_{if} = \frac{16\pi^3}{3\epsilon_0 c^3 h}\nu^3 \frac{S_{if}}{(2J' + 1)} \tag{2.5}$$

For absorption spectra, the quantity usually derived from observation is the line intensity, I. This has units of cm/molecule. I is temperature-dependent and is related to A_{if} by the expression:

$$I = \frac{Cg_i(2J'+1)}{Q_{vrn}(T)\nu^2} \exp\left(\frac{-hcE''}{kT}\right)\left[1-\exp\left(\frac{-hc\nu}{kT}\right)\right] A_{if} \qquad (2.6)$$

where ν is the frequency in cm^{-1}, E'' is the energy of the lower ro-vibrational level in cm^{-1}, Q_{vrn}(T) is the internal ground state partition function and is dimensionless, and g_i is the nuclear spin degeneracy and carries only one subscript since transitions between different nuclear spin states are not allowed (Miani and Tennyson, 2004). Boltzmann's constant, k, has units of JK^{-1} and the constant C has the value $(8\pi c)^{-1}$ = 1.3271x10^{-12} s cm^{-1}.

Since the BT2 line list includes A_{if} for each transition, the above equation enables the line absorption intensities to be computed at any given temperature.

Unlike the PES, where the most accurate ones are *ab initio* surfaces that have been fitted to the available experimental data, in the case of DMS, limitations on the accuracy of experimental line strengths means that, at the current time, the most accurate surfaces are purely *ab initio* (Lynas-Gray et al., 1995). Two such DMS were tested in the intensity part of our calculations. Our initial BT1 line list was computed using the same PES as BT2 and a preliminary DMS, of Lynas-Gray et al. (in preparation). The line positions in BT1 are identical to those in BT2 (the same PES having being used for both). However, we observed that the Einstein A coefficients of the weaker lines generated using the Lynas-Gray et al. DMS were often too large when compared with experiment. This part of the computation was therefore repeated using the DMS of Schwenke and Partridge (2000). The results, which are contained in BT2, show much better agreement between the computed strengths of weak lines and experiment. The Einstein A coefficients of the stronger lines in BT1 and BT2 generally agree to within two percent and both agree reasonably well with experimental values. In addition to being superior to the Lynas-Gray et al. surface that we tested, Schwenke and Partridge's DMS represents a major improvement on the earlier DMS of Partridge and Schwenke (1997) and from our analysis, as well from the same authors, was the most accurate in existence at the time that our calculations were performed.

Chapter 3

The BT2 line list

3.1 Computational requirements

BT2 is the final, distributed, version of the line list. As indicated in Section 2.2.5, as part of the development and testing of BT2 an earlier version, BT1, was produced. This has the same line positions as BT2 and in the case of strong transitions, very similar Einstein A coefficients. We deal here with the calculations involved in producing BT2. The methodology for the earlier BT1 line list was identical apart from the choice of DMS.

The BT2 line lists was computed on three Sun 5 Microsystem V880 mainframe computers at UCL's Hiperspace computing centre: Enigma and Ra, which are clustered using high speed interconnects, each having 8 processors (those on Ra being faster than on Enigma) and 32 Gb of RAM, and PSE, which has 24 processors and 96 Gb of RAM. The total disk storage on Enigma and Ra is 432 Gb (two-thirds of this being on Ra), and PSE has 1 296 Gb of disk space.

The final, 'DIPOLE' stage of the calculation was amenable to parallelisation with little time penalty. Other parts of the program were run on single processors, which avoided coding problems and was more efficient in computer time. The total number of processor hours employed in generating the BT1 line list (including the preliminary convergence testing which is discussed below) was 55 000 hr.. A further 10 000 hr. were used in repeating the 'DIPOLE' runs to generate BT2 and in testing the results. Several hard disks, having a total capacity of 1.5 Tb, were purchased to allow the wavefunctions to be stored (and backed-up) and then re-used for the second calculation.

3.2 Establishing the framework

The aim was to provide a line list that would be complete and spectroscopically accurate at the temperatures of late K stars (up to 4 000 K) and at wavelengths down to at least 0.8 μm. Preliminary calculations showed that in order to achieve this it would be necessary to include all states lying at energies up to 30 000 cm^{-1} relative to the ground state of the system. Previous workers, Miller et al. (1994) and Partridge and Schwenke (1997) selected lower energy cut-offs.

The cut-off for the total angular momentum was J=50. We estimate that the highest value of J that has ro-vibrational energies of less than 30 000 cm^{-1} is 58. However, it is estimated that by terminating our calculation at J=50, less than 500 levels out of a total of more than 221,000 are omitted and none of these excluded levels has an energy less than 23 490 cm^{-1}, with the majority being at energies above 28 000 cm^{-1}. The low number of lines omitted is a consequence of the density of the high energy states which is very much less (typically by two orders of magnitude) than for the same energy regions for low J states. Even at a temperature of 4 000 K these missing levels contribute less than 0.02% of the total partition function. Moreover, by omitting Js above 50 we saved in the region of 8 000 processor hours.

3.3 Labelling the levels

As is the case for observed water lines, the production of a synthetic line list prompts the question of how to assign quantum numbers to the transitions. The BT2 line list includes over 505 million transitions. However, all these transitions are between two of the energy levels in a list containing a much smaller number of entries: 221 097. The problem of assigning over half a billion transitions therefore reduces to that of labelling the energy states, which is a simpler, but still very considerable task. The DVR suite itself provides little assistance in this respect as it only generates data on: J, the symmetry block, the level number and the energy of each level.

In classical mechanics a three dimensional bent molecule has six internal spatial degrees of freedom. It follows from the Correspondence Principle that in a quantum mechanical regime, we must also define six quantum variables for such a molecule. Consequently, in the 'normal mode' (see below), we assume that the motion of the molecule within the electronic potential can be described by three vibrational and three rotational quantum numbers. As is explained below, these are not rigorous quantum numbers, and for higher excited states the fact that the rotational and vibrational states are not completely separable means that the 'normal mode' approach is no longer valid.

We now describe the labelling of the eigenvalue solutions to the Schröinger equation.

The rotational states of H_2O are labelled using the standard asymmetric top notation: J K_a K_c where J is the rotational angular momentum and K_a and K_c are the projections of J along the a and c axes respectively. The vibrational states can be labelled by both 'normal' and 'local' mode notation. In the normal mode notation (Bernath, 2005), which is the one most frequently used and is the one adopted for labelling BT2, (v_1, v_2, v_3) represent vibrational quanta for the symmetric stretch, bend and asymmetric stretch, respectively. The normal mode is satisfactory for labelling low levels of stretching excitation, but floppy molecules such as H_2O, H_2S and H_2Se have a local mode structure of the stretching energy levels (Child and Halonen, 1984). This is supported by Carleer et al. (1999) who indicate the near degeneracy of the J=4, 5 and 6, $(n,0)^+0$ and $(n,0)^-0$ states for water, (the notation is that used for local modes - see below) and by Zobov et al. (2000b), who state that for water molecules it was more satisfactory to label stretching states above about 15 000 cm^{-1} using local modes and also that vibrational states in the 20 000 plus cm^{-1} region are local mode-like, with the exception of higher bending modes (see below).

In local mode notation, $(mn)^{\pm}v_2$, (Halonen, 1998; Jensen, 2000), m and n represent quanta of local stretch in symmetric '+' or asymmetric '−' combinations. The superscript is dropped in the case where $m = n$ as this combination is always symmetric.

In the case of water, the frequencies of the symmetric and asymmetric stretch modes are nearly degenerate and, as a result, have strong resonant coupling (Darling and Dennison). In addition to the Darling-Dennison stretch-stretch resonance, there is a strong Fermi resonance in H_2O between the symmetric stretch and bend due to the approximate 2:1 frequency ratio of these modes and the same symmetries of the bend and symmetric stretch. There is no coupling between the antisymmetric stretch and bend as these have different symmetries and hence no terms in the Hamiltonian can connect them (Bernath, 2005, p229). The existence of these interacting vibrational states means that the spectrum of water has a pronounced structure.

Groups of interactions are labelled by a polyad number n, where $n = v_1 + 0.5 \times v_2 + v_3$, for every v_2. Polyads with even values of v_2 are labelled nν, whilst those with odd values for v_2 are labelled n$\nu + \delta$. Polyads nν and n$\nu + \delta$ each contain $(n + 1)(n + 2)/2$ vibrational states (Tennyson et al., 2001).

In both the normal and local modes, most of the labels used to characterise

the ro-vibrational energy levels are only approximate, and in particular break down at higher excitations (more quickly in the case of the normal than the local mode, as discussed above). Rose and Kellman (1994) predict that as the bending mode character increases the vibrational modes become chaotic and neither local mode or normal mode models are appropriate.

As the bending energy approaches the barrier to linearity at $11\,105\pm5\mathrm{cm}^{-1}$ (Kaine et al., 2000), the vibrational levels become disturbed and show a discontinuity (Child et al.,1999). This effect, known as quantum monodromy, has been observed in laboratory torch spectra by Zobov et al. (2005), who have recorded 134 previously unidentified bending states with ν_2 values between 5 and 9.

As stated above, the distinction that we make between rotational and vibrational states is artificial. The only rigorous quantum numbers for water are J (the total angular momentum), p, the rotational parity, which is given by $p = (-1)^{J+K_a+K_c}$, and q, the symmetry of interchanging the two H atoms, sometimes referred to as 'q' (not to be confused with the vibrational symmetry q in Table 2.5). If q is even, the state is ortho and if odd, para (Tennyson et al., 2001; Tennyson, 2006a).

Despite the problems, both conceptual and practical, associated with assigning 3 rotational and 3 vibrational 'quantum numbers' to ro-vibrational energy levels, we nevertheless followed the conventional practice and assigned normal mode 'quantum numbers' to as many BT2 levels as was possible within the available time constraints.

The process of labelling BT2 began by identifying those energy levels that matched levels whose six quantum numbers were known experimentally. Despite the fact that many papers have been devoted to labelling energy levels derived from experimental line frequencies (see for example, Polyansky et al., 1997c), so far, fewer than 15 000 experimentally-determined levels have been labelled with their 3 rotational and 3 vibrational quantum numbers (Tennyson et al., 2001).

Having incorporated all the experimentally-known labels, we then proceeded to label many levels that are not known experimentally, using the three different methods described below. However, in the first instance it must be explained that before it is possible to carry out systematic labelling of ro-vibrational states with higher J values, it is essential to have as a starting point a knowledge of the three vibrational quantum numbers of as many of the J=0 (i.e. pure vibrational) states as possible and of the six quantum ro-vibrational quantum numbers for as large a number as is possible for states with low J values. The first two methods described below are those that were used to determine the quantum numbers of the pure vibrational states and ro-vibrational states with low J values. The third method deals with the way in which these data were used to derive the ro-vibrational quantum numbers of

states with higher J values.

The labelling of many of the J=0 states that were not known experimentally was performed by R. Tolchenov using a visual inspection of the nodal structure of the wavefunction as described in Mussa and Tennyson, (1998). He also used the same method to label many other levels that were not known experimentally for J$\leq$7. The method is not totally accurate and involves a certain amount of subjectivity. In particular, it suffers from the fact that observations of the three-dimensional wavefunctions can only be made using two-dimensional sections, which can consequently be misleading. Furthermore, Mussa and Tennyson observed that at energies in the region of our cut-off of 30 000 cm^{-1}, a high proportion of the wavefunctions are irregular with no identifiable nodal structure. Nevertheless, this initial work by Tolchenov was fundamental in enabling the accurate labelling of higher J states, using the methods described below.

The second method involved examining the A_{if} coefficients for pure rotational transitions between an unlabelled vibrational state and a vibrational state that had already been labelled, the strongest transitions being those where ΔK$_a$ and ΔK$_c$ are both $\pm$1. Examples are [111] $\leftarrow$ [000] and [202] $\leftarrow$ [111]. This method was found to be useful for states having J<10. Again, this work was performed by R. Tolchenov, and the method is described in Tolchenov et al. (2005).

A third method employed algorithms invented by the author of this Ph.D. thesis. Using these, it was possible to label states having J$\geq$10 to fill in some gaps for lower Js and also to check, and sometimes correct, the labelling carried out using the two previously mentioned methods. He originally developed this method of labelling for an earlier exercise to determine the temperature-dependent partition functions of the HCN and HNC isomers (Barber et al., 2002). They were developed from an iterative treatment of small differences. The constants in the algorithms are the same as those in the well-known Pascal Triangle, but their signs alternate. Because of this simple pattern it is a straight forward exercise to write down higher order algorithms that are capable of achieving greater accuracy. In addition to their application in labelling levels, the algorithms can be used to predict higher terms in a wide variety of series where the relationship between adjacent terms is complex and unknown.

In Barber et al. (2002), the algorithm (3.1) was used to identify sets of levels within the same parity block having the same K$_a$, ν_1, ν_2, ν_3 quantum numbers, but different values of J and K$_c$ for HCN/HNC. However, in the case of H_2O, the greater density of the energy levels demanded higher accuracy than was the case for HCN/HNC and consequently, an extra term was required and algorithm (3.2) was employed for most of the labelling.

The simpler of the two algorithms is:

$$E_{J_n} \cong 3E_{J_{n-1}} - 3E_{J_{n-2}} + E_{J_{n-3}} \tag{3.1}$$

where E_{J_n} is the energy of the state in the same symmetry block having J = n and the same set of K_a, ν_1, ν_2, ν_3 quantum numbers.

and the one capable of achieving higher accuracy is:

$$E_{J_n} \cong 4E_{J_{n-1}} - 6E_{J_{n-2}} + 4E_{J_{n-3}} - E_{J_{n-4}} \tag{3.2}$$

Sometimes it was observed that resonance between levels caused the behaviour pattern to be erratic. This 'energy stealing' is a well-known physical phenomenon (Polyansky et al., 1997d) and the fact that BT2 is able to identify these resonances, attests to its accuracy. In addition to the difficulties in using algorithm (3.2) where the behaviour pattern of the levels is erratic, there were instances where no $E_{J_{n-4}}$ value existed. In both of these cases the additional term in (3.2) was disadvantageous and the original, simpler algorithm (3.1) was used.

In all, 25 870 levels in the BT2 list have been labelled using methodologies detailed above. In the case of J=0, quantum numbers are given for 270 of the 416 levels with energies below 30 000 cm^{-1}; the proportion of states labelled at higher Js becomes progressively less as J increases.

One important consequence of labelling levels is that when synthetic spectra are generated using spectra-BT2.f90, many of the transitions are fully assigned. This greatly increases the value of BT2 in both astronomical and laboratory spectroscopic applications.

3.4 Presentation of BT2

Details of the BT2 water line list were first published in Barber et al. (2006a). The complete BT2 line list is available electronically in compressed form at:
http://www.tampa.phys.ucl.ac.uk/ftp/astrodata/water/BT2/
and also at:
ftp://cdsarc.u-strasbg.fr/cats/VI/119
The data are in two parts. The first, the 'Levels File' is a list of 221 097 energy levels, ordered by J and symmetry block. As discussed in Section 3.3, many of these energy levels have been labelled with the appropriate angular momentum (J,K_a, K_c) and vibrational (ν_1,ν_2,ν_3) quantum numbers. An extract from the Levels File with an explanation of the contents of each of the 11 columns in the file is given in Table 3.1.

Table 3.1: Extract from the BT2 Levels File. A: Row in file, B: J, C: Symmetry (1-4: see Table 2.5), D: Row in block, E: frequency of transition in cm^{-1} F, G, H: ν_1, ν_2, ν_3. I, J, K: J, K_a, K_c.

A	B	C	D	E	F	G	H	I	J	K
2284	2	2	5	3885.718672	0	0	1	2	2	1
2285	2	2	6	4777.145956	0	3	0	2	1	1
2286	2	2	7	5332.258064	1	1	0	2	1	1
2287	2	2	8	5472.371851	0	1	1	2	2	1
2288	2	2	9	6254.694085	0	4	0	2	1	1
2289	2	2	10	6876.917089	1	2	0	2	1	1
2290	2	2	11	7027.396535	0	2	1	2	2	1
2291	2	2	12	7293.201639	2	0	0	2	1	1
2292	2	2	13	7376.617020	1	0	1	2	2	1
2293	2	2	14	7536.864373	0	0	2	2	1	1

The second part of BT2 is the 'Transitions File'. This has 505 806 202 entries. Each transition references upper and lower energy levels in the Levels File and gives the Einstein A_{if} coefficient for the transition. An extract from the Transitions File is given in Table 3.2.

In uncompressed form the BT2 Transitions File is 12.6 Gb of data. Therefore, in order to facilitate use of the list, the transitions have been ordered by frequency and separated into 16 smaller files, each representing a specific frequency range.

In addition to the files containing the actual line list, the ftp sites contain a Fortran program, spectra-BT2.f90, that will enable users to generate emission or absorption spectra from BT2 by specifying various parameters including: temperature, frequency range, cut-off intensity and line width. There is also a facility to generate spectra with full ro-vibrational assignments, if required. The method of using spectra-BT2.f90 is detailed in a 'readme-spectra' file and there are also examples of a job file and an output file. It will be seen that the job file requires the partition function Q_{vrn} for H_2O at the relevant temperature. The program has the ability to calculate $Q_{vrn}(T)$; alternatively the value may be inserted manually. It should be noted that the O/P degeneracies included in spectra-BT2.f90 are 3 and 1, which are four times the numbers commonly adopted by astronomers. Consequently if $Q_{vrn}(T)$ is to be inserted manually, the value to be employed is the 'spectroscopic' value which is four times the 'astronomical value', given in Vidler and Tennyson (2000).

Table 3.2: Extract from BT2 Transitions File. A, B: Row numbers in the Levels File. The identification of A as an upper level is not necessary because upper and lower can be identified from Level(A) - Level(B). C: A_{if} (s^{-1}).

A	B	C
1000	239	9.671E+01
1001	239	1.874E+00
1002	239	4.894E-03
1003	239	1.140E-04
1004	239	1.707E-02
1005	239	8.473E-08
1006	239	6.535E-04
1007	239	7.157E+00
1008	239	6.403E-06
1009	239	9.861E-05

3.5 Comparison with earlier line lists

3.5.1 The earlier line lists

Without any claim at completeness, some of the more important H_2O line lists are detailed below.

Before computational techniques were developed to produce *ab initio* line lists, experimentalists produced lists giving the absorption coefficients for water vapour, averaged over specific frequency intervals as a function of temperature. The first quantitative measurements of the transmission through water vapour, with temperatures up to 2 780 K, were performed by Hottel and Smith (1935). In the 1960s there was perceived to be a military requirement for more accurate data in order to analyse and predict rocket plume radiation (Ferrriso et al., 1966). Empirical lists were created that took as their starting point laboratory spectra produced, for example, by: Tourin and Henry (1959), Burch et al. (1963) and Ferriso et al. (1964). Ferriso et al. (1966) produced a complete set of absorption coefficients averaged in 25 cm^{-1} intervals between 50 and 7 500 cm^{-1}, at temperatures between 300 K and 3 000 K, plus some data at temperatures at the higher end of this range for frequencies up to 11 000 cm^{-1}. However, the most accurate and complete of these early absorption lists was that of Ludwig (1971), which although extending only to 9 300 cm^{-1} (at least in published form - it being noted that the work was of military importance), filled in the gaps in the Ferriso et al. (1966) data, and showed that the earlier figures for absorption at the higher end of the temperature range had been too high. Ludwig's data do not identify individual water lines, and by the early 1990s their coarse

resolution in terms of frequency bin-size, meant that they were no longer considered satisfactory for stellar atmospheric modelling (Schryber et al., 1995).

The initial MT H_2O line list (Miller et al., 1994) was extended by Allard et al. (1994), and subsequently reported on in Schryber et al. (1995). This version of the list includes 6.2 million transitions based on ro-vibrational states up to $J = 30$, with an energy cut-off of 11 000 cm^{-1}. Schryber et al. indicate that there is good convergence for states with $J \leq 20$ but there were convergence errors of $\sim$10 cm^{-1} at $J = 30$. The energy cut-off is too low (Jones et al., 1995), and the overall accuracy of the energy levels is not high enough (Allard et al., 1994) to give a good representation of stellar energy outputs shortward of 2 μm..

Jones et al. (2003) state that the PS H_2O line list (Partridge and Schwenke, 1997) represents a substantial improvement on the MT line list. However, for use in model atmospheres in the range 2 000–4 000 K these authors and also Viti (1997) indicate that it suffers from having an average cut-off of 28 000 $cm^{-1}$and that even below this cut-off there are many energy levels missing, which they indicate are due to poor convergence, stating in particular that the problems are due to Partridge and Schwenke's decision not to increase the size of the Hamiltonian matrix beyond that used for J=4. They estimate that PS omits $\sim$30% of transitions up to J=10, $\sim$50% up to J=20, and $\sim$60% up to J=28. Jones et al. state that for low-J energy levels, the Partridge and Schwenke calculations give 'superb results', however for higher rotational states, particularly those with J >20, a very high proportion of rotational states that should be degenerate in fact show significant splitting. Levels with high K_c and with K_a odd, lie below the ones with K_a even, when they should be quasi-degenerate. They indicate that since two transitions which, to within their line width are coincident, will have less effect on the opacity than two separate transitions, the artificial splitting in PS of quasi-degenerate states will cause the strength of water vapour bands to be overstated at low resolution.

Polyansky et al. (1997a) tested the hypothesis that the splitting found in the PS rotational levels is an artifact of the lack of convergence. They calculated energy levels using the same PES that Partridge and Schwenke had used to generate PS, but substituted the basis set of parameters employed by Viti (see below) to produce VT2. They observed that whilst there was good agreement with PS for low-J states, for J=24 the Polyansky et al., energy levels were systematically lower than those for PS by up to 1 cm^{-1}. Furthermore, none of the 'artificial' splittings were present in these new levels.

The Jørgensen et al., H_2O line list (known as SCAN) (Jørgensen and Jensen, 1993; Jørgensen, 2001) is structured so as to enable temperature-dependent opacity

calculations based on 100 million *ab initio* lines with energies up to 30 000 cm^{-1}. There is, however insufficient data to enable this list to be used for spectroscopic work, which is limited to two additional lists (designed to be used at different temperatures), each with 1,000 000 transitions.

Jørgensen's 2001 list is a development of the earlier work of Jørgesen and Jensen (1993) which included 80 000 transitions. Jones et al. (2003) report that synthetic spectra produced using the later SCAN list did not give a good match with ISO observations of M dwarf spectra in the 2.5–3.0 μm region, and that SCAN produced results that were substantially different to the other 3 lists tested.

The final H_2O line list that we comment on here is the VT2 list of Viti (1997). This list superseded the VTP1 list of Viti et al. (1997) that contained 230 000 lines. As VT2 was computed using an earlier version of DVR3D (Tennyson et al., 1995) it is more directly comparable with the BT2 line list than are the other line lists mentioned above. As described in Viti (1997), the list only includes transitions for states with J$\leq$9, although wavefunctions were produced up to J=28. The VT2 list is therefore of limited practical application, but it is important as it may be considered to be a forerunner of BT2.

Because of its similar origins to BT2, we give here the values of the five basis parameters and also n_H, and 'm' (determines IBASS) referred to in Section 2.2.1, that were used in producing VT2. These are: n_r=40, n_θ=40, r_e=2.55, ω_e=0.007, D_e=0.25, n_H=2 000 and m=300. As detailed in Section 2.2.1 the corresponding values used to generate BT2 were: 28, 44, 2.05, 0.008, 0.20, 2 500 and 530. Convergence testing on BT2 Section 2.2.2 suggests that the much lower value of 'm' is likely to have produced results for higher energy states that were not fully converged. We also note that the Morse oscillator functions (in particular, the choice of r_e), differed from the ones selected for BT2. However, this could be due to the fact that Viti used the PES of Polyansky et al. (1994), whilst BT2 was computed using the PES of Shirin et al. (2003).

Jones et al. (2003) and Allard et al. (2000) conclude that none of the above models is good enough to generate accurate spectroscopic models of cool stars. Of the then-available lists, Jones et al. comment that PS was the most accurate. Their observations serve as a preface to the computation of BT2, the accuracy and completeness of which are examined below.

3.5.2 Completeness

By comparing the partition function, Q(T), for water computed at a particular temperature using the energy levels from the BT2 and PS line lists with the most

accurately known value at this temperature, it is possible to estimate the completeness of the line lists and the opacity that is missing in spectra generated by the two line lists at the selected temperature (this method was developed by Neale et al., 1996, in their work on H_3^+).

A calculation of the partition function of water at 3 000K using the 221 097 energy levels in BT2 yields a value that is 99.9915% of the Vidler and Tennyson (2000) value, which indicates that levels missing from BT2 only contribute about 85 parts in a million to the partition function of water at this temperature, the reason being that there is a diminishingly small probability of states above 30 000 cm^{-1} being occupied at this temperature. For comparison, the PS line list, which has a 28 000 cm^{-1} cut-off gives a partition function at 3 000 K that is only 99.493% of the Vidler and Tennyson value.

Although the exclusion of levels above 30 000 cm^{-1} does not materially affect the completeness of the BT2 list, it does affect absorption at shorter wavelengths. If we consider a photon of of wavelength 1 μm (energy 10 000 cm^{-1}), this is able to be absorbed by a water molecule in a particular rotation-vibration level provided that there is another level 10 000 cm^{-1} above this lower state (to an accuracy that is determined by the intrinsic line width) into which the molecule may be excited. It follows that since the BT2 line list has an upper cut-off of 30 000 cm^{-1}, none of the energy levels in the list above 20 000 cm^{-1} are capable of being excited by a 1 μm photon, as there is no corresponding upper level.

If we examine the extent to which Q(3 000K) computed from BT2, but excluding all levels above 20 000 cm^{-1}, falls short of the Vidler and Tennyson value, this provides an indication (this is an upper limit as it takes no account of blending effects) of the opacity that has been excluded by adopting a 30 000 cm^{-1} cut-off. Performing the calculation gives a shortfall of 0.83%.

In the case of PS, only energy levels below 18 000 cm^{-1} are able to absorb a 1 μm photon, and computing Q(3 000K) using only PS states up to 18 000 cm^{-1} shows that these comprise only 98.37% of the Vidler and Tennyson value. Hence it will be seen that the opacity deficit at 1μm is in the region of twice as great in the PS list as in BT and the ratio increases at shorter wavelengths.

3.5.3 Accuracy

Before the publication of BT2, the most accurate list was PS. Table 3.3 compares BT2 and PS energy levels with known experimental values (Tennyson et al., 2001). It will be seen from this table that although the PS list is more accurate than BT2 in the cases where agreement with experiment is better than 0.1 cm^{-1}, this is not

Table 3.3: Comparison of BT2 and PS (Partridge & Schwenke, 1997) with 14 889 experimentally-determined energy levels (Tennyson et al., 2001).

Within cm^{-1}	BT2 %	PS %
0.1	48.7	59.2
0.3	91.4	85.6
1.0	99.2	92.6
3.0	99.9	96.5
5.0	100	97.0
10.0	100	98.1

Table 3.4: Comparison of BT2 and PS *ab initio* energy levels with experimentally-known levels for J=1 (all four symmetry blocks) taking every twentieth level known experimentally. Energies are in cm^{-1}

Exp.	K_a	K_c	v_1	v_2	v_3	Exp-BT	Exp-PS
5 354.871	0	1	0	1	1	-0.01	-0.02
7 468.342	0	1	0	0	2	-0.05	-0.07
8 844.536	1	1	1	1	1	-0.11	-0.03
10 334.369	1	1	0	7	0	-0.36	-0.37
11 055.476	0	1	0	0	3	-0.05	-0.05
12 444.094	1	1	1	1	2	-0.01	+0.01
13 858.487	0	1	0	7	1	-0.53	-0.49
14 719.133	1	1	1	5	1	-0.15	-0.09
15 784.299	1	0	2	1	2	+0.01	+0.04
16 936.990	1	0	5	0	0	-0.11	+0.38
17 785.302	1	0	1	0	4	-0.23	+0.08
19 802.586	0	1	5	0	1	-0.20	-0.99
21 258.129	1	1	5	1	1	-0.57	-3.39
25 150.162	1	1	7	0	1	+0.50	-104.36

the case generally. Specifically, based on a sample of 14 889 levels, whilst 99.2% of the BT lines are within 1.0 cm^{-1} of experiment 7.4% of the PS lines are outside this range. Other line lists (MT, VT2, SCAN) perform significantly worse than this.

Examining deviations from experiment by energy is even more revealing. Table 3.5 shows that PS is increasingly unreliable above 10 000 cm^{-1}, which is the region with the greatest number of transitions. In order to demonstrate that BT2 progressively achieves higher accuracy than PS as the energy of the state increases, Table 3.4 compares the BT2 and PS computed energies against the known experimental values for every twentieth energy level for J=1 (all four symmetry blocks) that is known experimentally.

Table 3.5: Numbers of levels in BT2 and PS (Partridge & Schwenke, 1997) disagreeing with experiment (Tennyson et al., 2001) by more than 2 cm^{-1}, ordered by energy.

Level Energy cm^{-1}	Number in range	BT2 No.	PS No.
20 000 - 26 300	575	9	334
15 000 - 20 000	2 813	10	105
10 000 - 15 000	6 323	8	58
7 000 - 10 000	3,263	3	9
< 7,000	1 914	0	0
Total	14 889	30	506

Finally, it should be noted that even though the Variational Principle was applied in determining the computational parameters to be applied in calculating BT2, the energy levels that have been calculated are able to deviate from the experimental values on the downside as well as on the upside. This is due to errors in the PES.

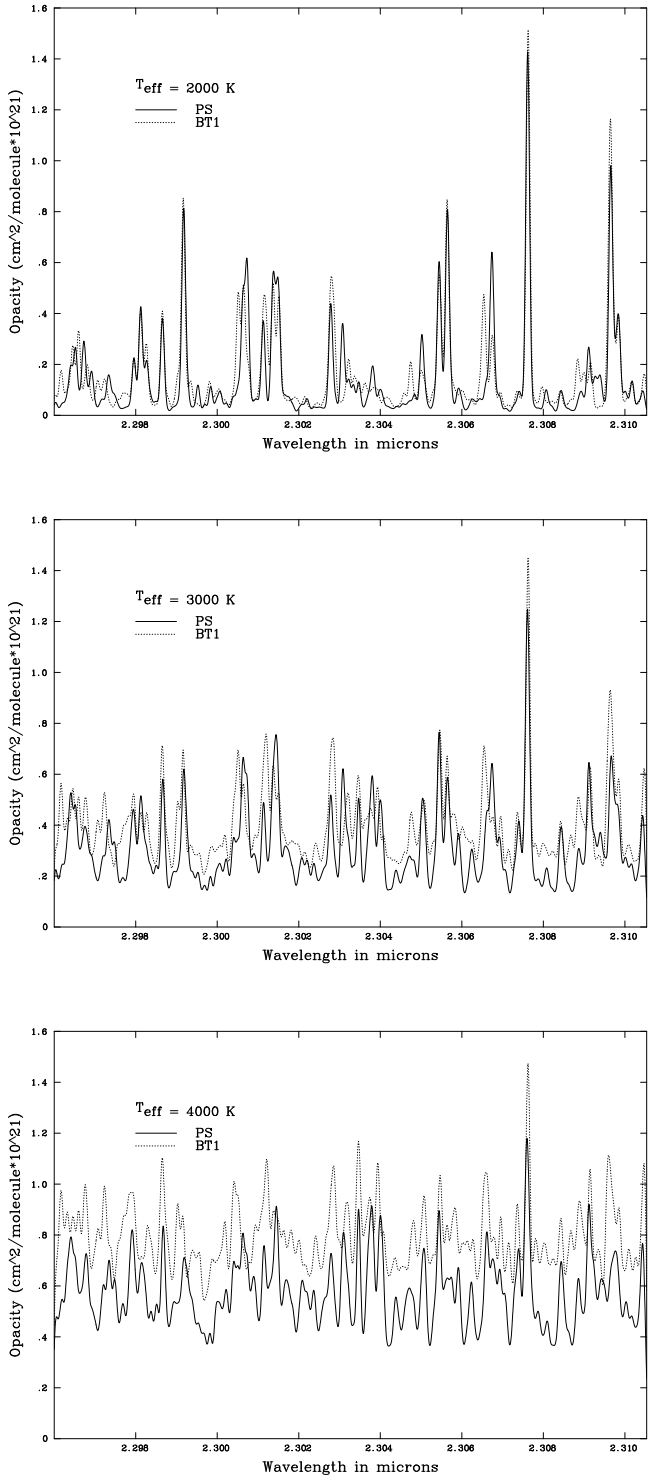

Figure 3.1: A comparison of BT1 and PS synthetic spectra at 2 000, 3 000 and 4 000 K. The missing opacity in PS becomes increasingly apparent at higher temperatures. Reproduced from Jones et al. (2005a).

Chapter 4

Introduction to the practical applications of BT2

A major part of this Ph.D. thesis is devoted to applications of BT2. Water exists in a very wide range of astronomical environments; its spectrum is also the subject of numerous laboratory investigations. Until the publication of the BT2 line list earlier this year, the author of this thesis was the only person able to use the list and consequently this unique position has meant that he has been involved in a large number of astronomical and laboratory-based collaborations employing BT2. Moreover, even though the line list and Fortran program 'spectra-BT2.f90' are now freely available on our Group's ftp site and also from the CDS archive in Strasbourg, as detailed in Section 3.4, many research groups still find it more convenient to approach the author directly to generate synthetic spectra, to identify lines and to compute physical parameters based on best fits, than to conduct these exercises themselves.

The following chapters deal with the uses to which BT2 has been put. We differentiate between five types of application:

- Those, of an astronomical nature, in which the author has been involved in all aspects of the work, including: observation, data reduction, the generation and fitting of synthetic spectra, line identification and the formation of conclusions. Work on comets Tempel 1 and Schwassmann-Waschmann 3 fall into this category (Meech et al., 2005; Barber et al., 2006c, Barber et al., 2006e).

- Astronomical applications in which the author has not been involved in obtaining the observational data, but has been directly involved in all other aspects of the project including using BT2 to derive physical parameters. The work on

the temperature and water column density of V838 Mon falls into this category (Banerjee et al., 2005; Barber et al., 2006b).

- Applications where the author of this Ph.D. thesis has provided numerical data that he has either computed directly, using BT2, (Dello Russo et al, 2004, 2005; Kawakita et al., 2006) or else has derived by comparing BT2 synthetic spectra output with observation (Rawlings et al., in prep.).

- Those applications in which the author has responded to a specific request to use BT2 to identify observed spectral features or individual lines. In some instances, such as Lyubchik et al. (2006), the author of this Ph.D. thesis has collaborated in producing a paper, whilst in others, e.g. Smith et al. (2004), the authors of the paper have merely acknowledged the contribution.

- Applications of an astronomical or experimental basis, where the author has provided researchers either, with access to the complete or relevant parts of the BT2 line list, or else, has provided synthetic spectra produced using BT2. Barber et al., 2006d, which deals with modelling cool stellar atmospheres using BT2 in the PHOENIX model, and Pavlenko et al. (2006), which includes the BT2 water line list in its molecular database for computing the spectral energy distribution (SED) of V838 Mon, are examples of the former, whilst Jones et al., 2005a, 2005b; Moont, 2005, Coheur et al., 2005, Zobov et al., 2006 are in the latter category.

The most important of these applications are described in the following chapters.

Chapter 5

Applications in V838 Mon

V838 Mon is an astronomical object that has caused much debate and also attracted a great deal of publicity.

The author's direct involvement has been of two types. He used synthetic spectra generated with BT2 to identify water lines (the first, and we believe, the only occasion that individual water lines have been identified in this object). By fitting the synthetic spectra to the observed data on five separate dates, the author was able to determine the rotational temperature and H_2O column density in the ejected circumstellar shell on these five dates.

Subsequently, the author has collaborated in modelling the time evolving chemistry of the circumstellar shell (Rawlings et al., in prep.). The resulting model agrees well with the author's determination of the H_2O column densities on five dates (see above), as well as with those for other species, determined on a single date (Lynch et al., 2004), with the exception of H_2S, which is wrongly reported in that paper.

In addition to the above applications, the BT2 line list was used by Pavlenko et al. (2006) to compute the theoretical spectral energy distribution of an L supergiant, for the purpose of comparison with V838 Mon spectra. These authors obtained a qualitatively good fit of the spectrum of V838 Mon over a wide spectral range (0.4-1.0 μm), with a model atmosphere having $T_{eff} = 2\,000$ K.

5.1 Introduction

V838 Mon was detected in eruption on 2002 January 6 (Brown, 2002) with a peak amplitude of $V_{max} = 10$ and was originally thought to be a nova. Indeed its spectrum had an F-type continuum with neutral hydrogen lines and ionized metals - all characteristic of a nova. However, V838 Mon soon exhibited un-nova-like proper-

Figure 5.1: Hubble Space Telescope image of V838 Mon, 27 March 2003

ties. Over the following two months, there were two more outbursts with amplitudes V_{max} 6.7 and 7 respectively. Moreover, following its sharp rises in intensity in which it reached a luminosity of $\sim$1 $L_{\odot}$ in February 2002 and had the temperature of an F supergiant, V838 Mon cooled rapidly. By October 2002 it was exhibiting spectral features characteristic of a late M supergiant, and by January 2003 its photosphere had cooled to $\sim$2 100 K (Lynch, et al., 2004). At this time, the spectrum of V838 Mon had similarities to that of a cool L type dwarf (Evans et al., 2003). Evans et al. computed a detailed model of V838 Mon and its circumstellar environment. In this model the central star has a photospheric temperature of $\sim$2 100 K and is surrounded by a spherical envelope of molecular matter at $\sim$800 K. Neither the star,

nor the envelope, are able to be resolved, even in high-resolution Hubble images. In contrast, the expanding light echo associated with V838 Mon can be resolved by ground-based instruments (Henden et al., 2002; Bond et al., 2003).

The distance to V838 Mon is not accurately known. Estimates, based on photometric measurements of the light echo, suggest a figure in the range 8-10 kpc (Tylenda, 2004; Crause et al., 2005, van Loon et al., 2004). However, Sparks (2005) using polarimetry computes a lower value: ∼6.0 kps, and further observations of the object will be required in order to secure a value for its distance.

In addition to uncertainty over the distance of V838 Mon, there is a lack of consensus regarding the nature of the object and of its light echo. There are two main schools of thought regarding the nature of V838 Mon. One suggestion is that we are observing an AGB object (these are known to be unstable with deep convective shells) throwing off material and moving rapidly to the right on the H-R diagram. The precise temperature of the progenitor is not known, but Tylenda et al. (2005) suggest an early B star with a temperature lower than 30 000 K. Also, the mechanism responsible for the very rapid transition is not understood. It has been suggested, for instance, that it could be related to a B3V star observed in the same field. Other ideas involve some form of merger: Retter et al. (2006), suggest the ingestion of three planets (each event corresponding to one of the observed light peaks) by an expanding red giant, whilst Soker and Tylenda (2006), propose the merger of two stars.

There are also different hypotheses regarding the nature of the so-called 'light echo'. When the first Hubble images of V838 Mon were released by NASA, there was general agreement that what was being observed was light reflecting off circumstellar dust that had been thrown off from the progenitor of V838 Mon in earlier epochs (similar to those responsible for the rapid brightening of the object in 2002). However, Tylenda (2004), Tylenda et al. (2005) and Banerjee et al. (2006), all suggest that the dust from which the light (and in the case of Banerjee et al., infrared radiation), is being emitted is interstellar in nature. In this respect, the most significant results are those of Banerjee et al., who, using the IR light echo, estimate that the mass of the dust plus gas in the region responsible for the light echo is ∼150 $M_{\odot}$. This figure is itself too high to have been caused by earlier ejections from a star of even the most massive type, and when the figure is adjusted to include an estimate for the full extent of the echoing region, the corrected value for the total gas and dust is ∼900 $M_{\odot}$ (Soker and Tylenda, 2006).

In some respects V838 Mon is similar to V4332 Sgr and M31-RV (two other objects which have erupted in the last 10-15 years) and it is suggested that these

objects may form a new class of eruptive variable (Banerjee and Ashok, 2004).

5.1.1 Water bands

Figures 1 & 2 of Evans et al. (2003), and Figures 6 & 7 of Lynch et al. (2004) reveal wide, deep absorption troughs between the spectral bands e.g at 1.4 μm between the J & H bands and at 1.9 μm between the H & K bands. Such inter-band features are usually due to water and are commonly observed in cool M stars (Lançon and Rocca-Volmerange, 1992). Neither Evans et al. nor Lynch et al. record individual water lines in the spectra of V838 Mon.

5.1.2 Mt. Abu spectra of V838 Mon

Since early 2002, with the exception of the rainy season (mid-June to early October), Banerjee and Ahshok of PRL Ahmedabad, have taken near-IR spectra of V838 Mon at fairly regular intervals, using the 1.2 m telescope on Mt. Abu. Five H band spectra, obtained at a resolving power of $\sim$1 000 between November 2002 and December 2004 are shown in Figure 5.2.

Apart from the absorption features longward of 1.73 μm, which we identify as being due to water, and the AlO bands (Banerjee et al. 2003) that are indicated in Figure 5.2, most of the other strong features in these spectra are due to the second overtone of ^{12}CO (Banerjee and Ashok, 2002).

5.1.3 Water lines, temperature and H_2O column density

By comparing the observed spectra with synthetic BT2 spectra it was possible to identify a number of features in Figure 5.2 as being due to water. The relative intensities of the various features are very temperature-dependent. Hence, by generating spectra at different temperatures and testing for best fit with observation (Fig. 5.3), it was possible to determine the temperature of the region within which water absorption was taking place on each of the five dates (Table 5.2).

In Figure 5.3 the observed spectra are shown as histograms, whilst the synthetic spectra are presented as smooth curves. It is seen from Table 5.2 that between 19 November 2002 and 25 December 2004 the temperature of the water-absorbing region decreased from 900$\pm$30 K to 750$\pm$50 K over a period of 767 days.

Many of the transitions within the BT2 line list have been labelled, and consequently it was possible to identify the 17 strong lines that comprise the five main absorption features in Figure 5.3. The details are given in Table 5.1. The lower and upper levels for each of these transitions are labelled in the manner: (ν_1 ν_2 ν_3)[J K_a

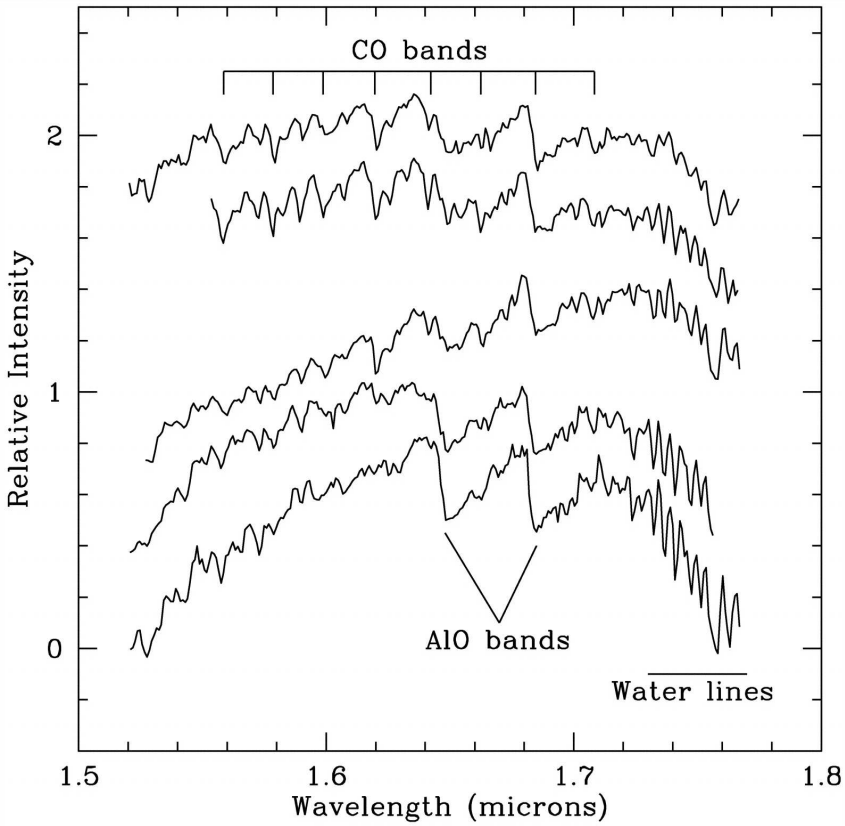

Figure 5.2: H band spectra of V838 Mon. The spectra are vertically offset by arbitrary amounts for clarity of presentation. Bottom to top, the dates are: 20 Nov. 2002, 25 Jan. 2003, 14 Dec. 2003, 15 Apr. 2004 and 25 Dec. 2004. Reproduced from Banerjee et al. (2005).

K_C]. It is seen that with the exception of one line at 1.74454 μm all of these strong transitions are in the (0 1 1)←(0 0 0) band, and it is for this reason that we state that the temperature that we have determined is the 'rotational' temperature.

Table 5.1 also contains information about intensity. The fourth column gives the relative intensities of the 17 strongest synthetic H_2O lines in the wavelength range 1.726 to 1.751 μm at a temperature of 800 K, whilst the last column gives the relative intensity of the five strong absorption features that are the result of the blending of these lines. The intensity is expressed as the total integrated line intensity within the bin whose position corresponds to that of maximum absorption within the feature. The apparent discrepancies between the two sets of data are explained by the fact that the features comprise not only the strong lines listed in Table 5.1, but a large number of weak lines that collectively make an important contribution to total absorption.

Lastly, it is possible to estimate H_2O column densities using the expression:

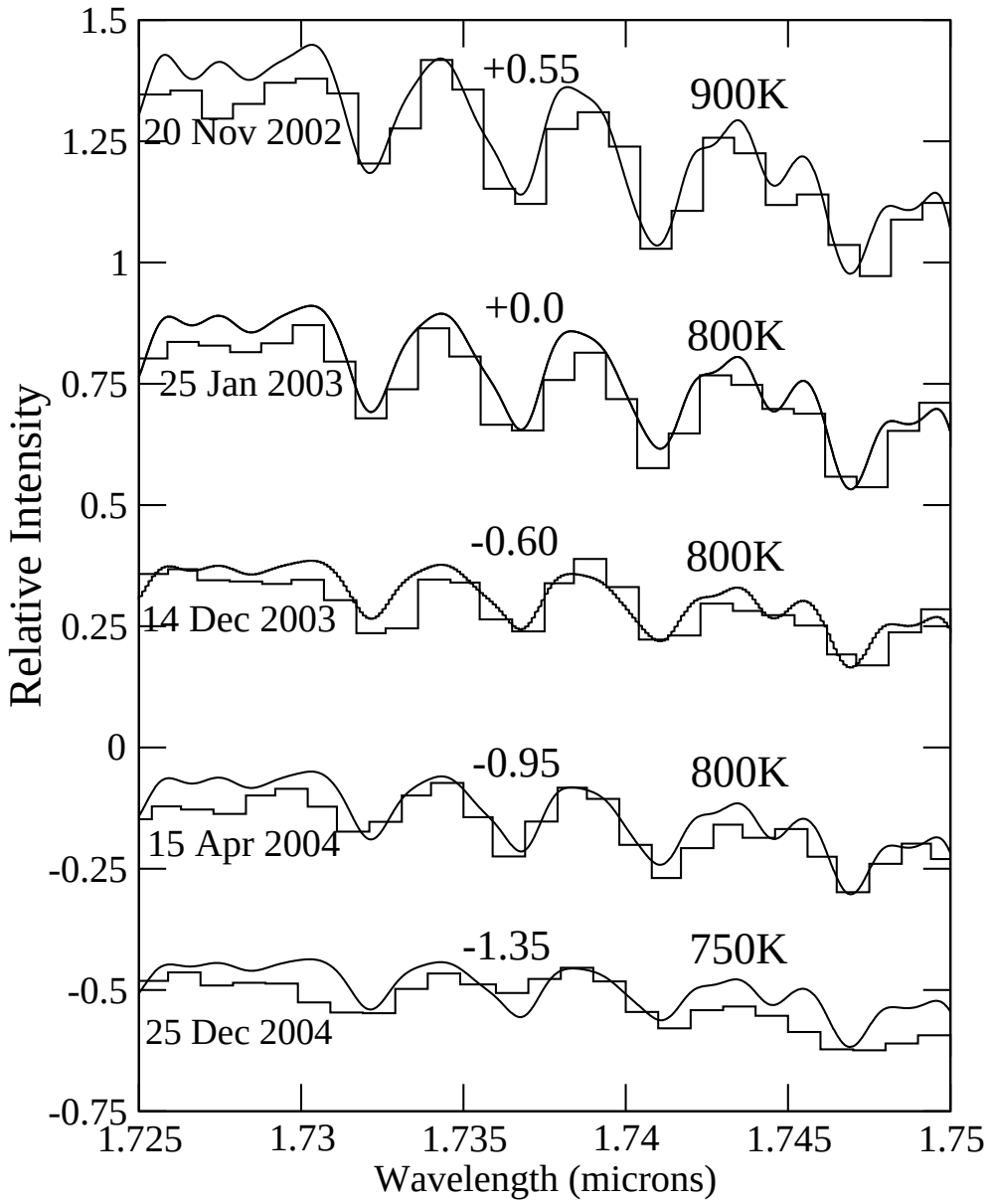

Figure 5.3: Synthetic spectra (solid curves) superimposed on the observed data (histograms), for the different epochs of observation. For ease of presentation, the five pairs of data are plotted with constants added to their relative intensities. The values of these offsets are listed next to the plots. Reproduced from Banerjee et al. (2005)

$I = I_0 \exp(-\kappa_\lambda \mathrm{NS})$, where N is the number of water molecules per cm^3, S is the distance in cm and the product NS is the column density (molecules cm^{-2}). κ_λ is the opacity at wavelength λ and is one of the outputs of the program spectra-BT2.f90.

Once the best temperature fit has been established, the optimum values of I_0 and NS that give the best fit to the observed data at that temperature were obtained. The effect of increasing I_0 is to raise the overall level of the synthetic plot, whilst increasing NS has the effect of increasing the depth of the strong absorption features relative to the weak ones. The process employed is iterative, a more accurate fit to temperature being achieved once approximate values for I_0 and NS have been established. Table 5.2 details the estimates of the $\mathrm{H_2O}$ column density on each of the five dates.

The methodology is liable to suffer from systematic errors and consequently the derived column densities are estimated to be accurate to within a factor of two. However, the comparison between the column densities at the different dates will be more accurate, and the error in the relative numbers is estimated to be +25%, −20%.

5.1.4 Discussion

The column density and temperature estimates have been compared with those derived by Lynch et al. (2004). The envelope temperature of 800±30 K on 25 January 2003 is consistent with that of 750-790 K derived by Lynch et al. at a similar date and based on observations of: $\mathrm{H_2O}$ and CO molecular bands and the SiO (2ν) overtone. Our estimate of the $\mathrm{H_2O}$ column density on 25 January 2003 is approximately half the Lynch et al. (2004) value, but the figures are in agreement within the estimated error.

Even though the rate of cooling must slow, it is likely that at some future time the temperature of the water-bearing envelope will reach the ice sublimation temperature (∼150 K) to form water-ice. Such a development would further enhance the similarity between V838 Mon and its possible analog V4332 Sgr in which water ice was detected strongly 10 years after the object's outburst (Banerjee et al., 2004).

5.2 Modelling the chemistry

Rawlings et al. (in prep.), have constructed a time-evolving chemical model of a single region located at the outer edge of the molecular shell, which they assume to be representative of the whole shell. The chemical network includes 1 540 reactions

Table 5.1: Line Centres and Relative Intensities of lines, I_{line}, and features, $I_{fea.}$, computed at 800 K, for 25 Jan 2003: Reproduced from Banerjee et al. (2005).

Lower level $(\nu_1\nu_2\nu_2)[JK_aK_c]$	Upper level $(\nu_1\nu_2\nu_2)[JK_aK_c]$	λ μm	I_{line} Rel.	Center μm	$I_{fea.}$ Rel.
(0 0 0)[7 3 4]	(0 1 1)[8 5 3]	1.73202	1.93	1.7329	1.77
(0 0 0)[6 3 4]	(0 1 1)[7 5 3]	1.73239	1.61		
(0 0 0)[9 2 7]	(0 1 1)[10 4 6]	1.73686	2.83	1.73686	1.93
(0 0 0)[15 7 8]	(0 1 1)[16 7 9]	1.73987	1.23		
(0 0 0)[15 5 10]	(0 1 1)[16 5 11]	1.74036	2.07		
(0 0 0)[16 6 11]	(0 1 1)[17 6 12]	1.74082	1.03	1.74071	2.21
(0 0 0)[15 6 9]	(0 1 1)[16 6 10]	1.74121	1.91		
(0 0 0)[5 3 2]	(0 1 1)[6 5 1]	1.74128	1.26		
(0 0 0)[14 8 7]	(0 1 1)[15 8 8]	1.74269	1.27	Shoulder	1.36
(0 0 0)[7 0 7]	(0 1 1)[8 2 6]	1.74445	1.24		
(0 0 0)[13 5 8]	(1 1 0)[14 6 9]	1.74454	1.23	1.74456	1.77
(0 0 0)[13 9 4]	(0 1 1)[14 9 5]	1.74471	1.12		
(0 0 0)[14 7 8]	(0 1 1)[15 7 9]	1.74650	2.12		
(0 0 0)[6 2 5]	(0 1 1)[7 4 4]	1.74674	2.29		
(0 0 0)[16 5 12]	(0 1 1)[17 5 13]	1.74680	1.50	1.74688	2.59
(0 0 0)[8 2 6]	(0 1 1)[9 4 5]	1.74728	1.36		
(0 0 0)[14 6 8]	(0 1 1)[15 6 9]	1.74750	1.13		

Table 5.2: Temperature and Column Densities: Reproduced from Banerjee et al. (2005).

Obs. Date	Temperature (^{o}K)	Error (^{o}K)	Column Density mols cm^{-2}
20 Nov 2002	900	30	$9.3\text{x}10^{21}$
25 Jan 2003	800	30	$9.0\text{x}10^{21}$
14 Dec 2003	800	30	$3.8\text{x}10^{21}$
15 Apr 2004	800	40	$5.1\text{x}10^{21}$
25 Dec 2004	700	50	$4.6\text{x}10^{21}$

between 102 chemical species (Le Teuff et al., 2000) and this gives a comprehensive description of the circumstellar gas with molecules composed of the elements: H, He, C, N, O, Na, Si and S.

Their model includes three structural components:

- The central source (photosphere) which is an expanding, optically thick, cool, stellar envelope with properties similar to an L or M supergiant.
- An ejected shell at a distance of ∼40 AU.
- The large-scale cool molecular cloud that is responsible for the 'light echo'. As we have indicated, there is disagreement over the nature and position of this cloud, which contains the dust responsible for the 'light echo'. This region is unconnected with the molecular detection in the shell, and is therefore disregarded in the modelling.

Using spectra obtained ∼315 days after the first eruption of V838 Mon, Lynch et al. (2004) recorded column densities for five molecular species observed to be present in shell. Lynch et al. give the estimated column density for a sixth species, H_2S, but this was found to be unreproducible in the model and was later confirmed to be very substantially in error (private communication). These derived molecular column densities and the temporal evolution of the H_2O column density, see Table 5.2, were used as a check on Rawlings' chemical model.

Rawlings et al. used the time-dependent temperatures of the envelope detailed in Banerjee et al. (2005). The photospheric temperatures and radii were taken from Tylenda, (2005).

The radial dependence of the density of the shell is unknown and Rawlings et al. adopt two separate models. The first assumes an inverse square relationship, and the second an inverse cube relationship. The inverse square relation between density and radius gives column densities that are far too low, but an inverse cube relationship was found to give much more realistic results and was therefore adopted.

A major source of uncertainty in the model is the initial conditions, in particular the initial ionisation level and the initial H_2:H ratio. Being a non-photon dominated environment, free electrons are required to drive a negative ion chemistry via: H^-, C^-, O^-, OH^- etc.. In the atmospheres of M giants/supergiants the main donors of free electrons are alkali metals. However, in the envelope of V838 Mon shocks may be a contributing factor.

Also, the local radiation field within the molecular shell is poorly constrained. Rawlings et al. consider four components:

- The photospheric contribution, which is a function of the geometry of the shell and also the time evolving radius and temperature of the photosphere.
- A local source term for the shell, assuming the temperatures in Table 5.2

- A possible contribution from a companion B3V star.
- The contribution from the ambient interstellar UV radiation field.

The model definitely rules out the possibility of a remaining, central B-type star since the high UV flux associated with such a star would destroy the molecules in the shell.

5.2.1 Derived chemistry

Within the estimated errors of Lynch et al. (2004), Rawlings et al. model a chemistry that is consistent with the column densities of the five species derived by Lynch et al.. Perhaps surprisingly, the H_2:H ratio never exceeds 10%. CO saturates at ∼0.1 days. Since the environment is oxygen rich, the abundances of hydrocarbons and other carbon-bearing species decline sharply after this time. At a later time, the oxygen budget appears to be approximately evenly split between CO, O_2, OH, H_2O, CO_2, SO_2 and SiO_2, and to a lesser extent, NO and SO. This oxygen rich chemistry is unusual in astronomical environments, where H-dominated chemistry is the norm. In addition, Rawlings et al.'s model reproduces well the time-dependence of our derived water column density (Table 5.2).

5.3 BT2 used to generate synthetic SED

Pavlenko et al. (2006), have computed a theoretical photospheric spectral energy distribution of an L supergiant in the optical and near infrared regions for the purpose of comparison with the observed spectrum of V838 Mon, in the range 0.45–1.0 μm, obtained with the Shane 3 metre telescope at Lick Observatory in November 2002.

Adopting a classical approach, these authors use NextGen model photospheres (Hauschildt et al., 1999) with T_{eff} = 2 000–2 200 K. Their model includes atomic and molecular line data for ∼100 species assembled from a variety of sources. In the case of H_2O, line data are taken from BT2.

With the exception of absorption in the 0.75 μm region, they obtain a qualitatively good fit of the spectrum of V838 Mon over the whole observed spectral range, with a model atmosphere having T_{eff} = 2 000 K.

Chapter 6

Cometary applications

Although the low temperatures associated with comets do not make these objects an obvious area of application of the BT2 line list, there is a particular feature of the emission spectra of the cometary comas that makes the study of their spectra ideal territory for BT2, and this is discussed below. The author has been involved in the production of five papers on cometary work (Dello Russo et al., 2004, 2004; Meech et al., 2005; Barber et al., 2006c and Barber et al.,2006e). In addition, BT2 data is now being used by other researchers in the field (Kawakita et al., 2006).

6.1 Introduction

Comets are of particular scientific interest because their nuclei (with the exception of their dusty surfaces) have not been altered to any significant extent since the comets were formed in the primordial Solar System. By investigating the composition of comets we are thus able to gain important knowledge about the chemical composition of the regions in which they formed, more than 4 billion years ago.

There are believed to be two main reservoirs of comets in the Solar System: the Oort cloud, which is a spherical region extending from ∼10 000 AU to possibly 50 000 AU from the Sun, and is thought to contain $\sim 10^{10}$ cometary nuclei (Stern, 2003; Duncan et al., 2005) and the Kuiper-Edgworth belt, which includes several billion comets orbiting at heliocentric distances ranging from ∼40 to several hundred AU (Morbidelli and Brown, 2005). Unlike the Oort Cloud, the Kuiper-Edgworth belt is concentrated close to the ecliptic.

Comets remain largely undetected unless they are perturbed gravitationally so that they enter the inner solar system. In particular, comets originating in the Kuiper-Edgworth belt have short periods and prograde low-inclination orbits, and

because of this are the ones most frequently observed. In contrast, Oort cloud comets have random orbital inclinations and their motion can be either prograde or retrograde. Once within the inner Solar System, comets are activated by sunlight. If they approach sufficiently close to the Sun, their surface ices sublime and escaping gases are able to eject small icy-dust particles from the cometary surface. Together these can give rise to 'tails'. One is composed of dust, and points backwards along the comet's path, and the other is made up of ionized gas. This points directly away from the sun (Yeomans, 2005). These tails are frequently able to be seen from Earth with the naked eye.

Comets are cold objects. Their surface temperatures depend, *inter alia*, on their distances from the sun, but even as close as 1 AU their surface temperatures typically average only ∼300 K, with differences of possibly 100 K or more in the temperatures of the sunward and dark sides (depending on their rotational rates). The temperature of the sunward side of the comet is the main determinant of the rate of sublimation of water molecules from the icy region just below the dusty surface of the comet. The temperature of the gaseous molecules is collisionally thermalised in the region very close to, possibly within 500 metres of, the surface, and comets have been observed that have inner coma temperatures in the range 20–150 K (Dello Russo et al., 2004). In contrast, the ambient temperatures of Oort cloud comets are only ∼5 K and 30–60 K for Kuiper-Edgworth belt comets (Mumma et al., 1993).

Gaseous H_2O molecules in the coma of comets produce ro-vibrational spectra that, in principle, can be observed from Earth. However, the low temperatures, and the presence of water in the Earth's atmosphere, are serious impediments to observing water lines in comets. The gaseous water molecules are predominantly in low ro-vibrationally excited states and the principal route for radiative decay is by fundamental transitions (that is to say transitions to the ground vibrational state). The emitted photons are then absorbed by water molecules in the Earth's atmosphere, and hence are not observable by ground-based observers. Radio observations have been useful for detecting some molecules, such as ammonia (Bird et al., 1999), but only a few transitions have been recorded for water. Bird et al. (1999) report a 'marginal' detection of the 6_{16}–5_{23} H_2O rotational transition at 1.35 cm., and in the sub-millimetre, Bensch et al. (2006) have observed the 556.937 GHz 1_{10}–1_{01} ground state transition in Submillimeter Wave Astronomy Satellite (SWAS) spectra. However, in general, these wavelength regions have produced a very limited amount of information about water in comets.

Despite these observational difficulties, it is important to be able to quantify the rate of water emissions from comets, since water is the dominant ice in comets and

within 3-4 AU of the Sun its sublimation controls the release of other volatiles (Dello Russo et al., 2004).

Consequently, attention has focussed on other methods of measuring cometary water. In recent years, it has been realised that certain weaker transitions are not absorbed by the Earth's atmosphere. These are solar-pumped fluorescent 'SPF', water lines, originating in non-LTE regions of a comet's coma. They are transitions from higher-lying ro-vibrational states that have been 'pumped' by solar photons, to lower energy vibrationally-excited states. Despite being weaker than the fundamental transitions, it is possible to observe infrared SPF lines from ground-based telescopes. They are not extinguished by atmospheric water, as they are 'hot band' transitions, that is to say, transitions to energy levels that are above the ground vibrational state, and which are consequently lowly populated in the Earth's atmosphere.

In LTE environments, where collisional de-excitation dominates, these upper levels would only be significantly populated at temperatures of several thousand Kelvin. However, in non-LTE environments, such as exist in the coma of comets, they are able to remain populated for periods long enough to allow spontaneous radiative de-excitation. SPF transitions have been used to determine the rotational temperatures of Comet 153P/Ikeya-Zhang (Section 6.2).

As mentioned in Section 2.2.3, the H_2O molecule has two distinct forms, ortho and para. At temperatures above ~50 K, the ortho-para ratio (OPR) for H_2O is 3:1. However, the lowest ortho level lies 23.8 cm^{-1} (equivalent to ~34 K) above the lowest para level, so at very low temperatures, para states are increasingly favoured.

There is evidence that once an H_2O molecule has formed, both radiative and collisional processes (in a molecular cloud or cometary environment) are extremely inefficient at converting between the ortho and para states. Theoretical studies demonstrate a radiative conversion time for H_2 that exceeds the age of the universe, whilst collisional induced O-P and P-O hydrogen molecule decay rates are also of the order of the age of the universe in low temperature and low density astrophysical environments, such as cold molecular clouds or cometary coma (Dodelson, 1986; Mumma et al., 1993). Also, laser-induced fluorescence experiments show no evidence of nuclear spin state conversion during molecular collisions (Nela et al., 2000). Therefore, it seems certain (Miani and Tennyson, 2004) that H_2O molecules do not undergo significant nuclear spin conversion either in the cometary nucleus or during sublimation into the coma. Thus, nuclear spin temperatures (derived from measured OPRs in the coma) may be a measure of the chemical formation temperature of water in comets and could provide clues about the formation region and processing

histories of cometary ices (Mumma et al., 1989, 1993).

Using BT2 to assign SPF transitions into ortho and para groups, and using BT2 Einstein A coefficients, it has been possible to determine nuclear spin temperatures for three comets: C/1999 H1 (Lee), C/1999 S4 and C/2001 A2 (Section 6.3). Subsequently BT2 data were used by Kawakita et al. (2006) to calculate the nuclear spin temperature of comet C/2001 Q4 (Neat).

In addition, using BT2, it has been possible to identify what may prove to be a new class of line in the post-impact spectrum of comet 9P/Tempel 1, (Section 6.4.1). These are transitions from upper levels whose ro-vibrational energies are too high to be pumped by the normal SPF mechanism (this is established by an examination of the Einstein B coefficients and ground vibrational populations of the allowed pumping routes). These are tentatively labelled 'SH' (Solar Heated) transitions, in order to differentiate them from the SPF lines, but this nomenclature does not imply knowledge of the process by which these lines are formed in cold cometary coma.

Because the non-fluorescent transitions do not derive from regions that are in local thermodynamic equilibrium (LTE), the computation of the relative intensities of these transitions as a function of the temperature of the inner coma of the comet is complicated, requiring knowledge of: the Einstein B coefficients of the allowed transitions from the ground vibrational state by which the upper level may be populated, the Einstein A coefficients of the various routes by which the upper state may decay, and similar information for higher energy levels which, by a cascading process, are able to populate the upper level of the selected transition. The methodology, which is detailed in Dello Russo et al. (2000), is outlined in Section 6.2. Most of the data required to perform the calculations are not available experimentally, but can be determined using the BT2 water line list.

6.2 Rotational temperature of Comet 153P/Ikeya-Zhang

The author used the BT2 line list to compute the frequencies and Einstein A coefficients of the 64 transitions (up to J=7) that make up each of the 7 hot bands of water that are known to have been detected in comets. These data were applied in the determination of the temperature-dependent fluorescence efficiencies (also known as g-factors) of each observed fluorescent water line in the spectrum of Comet 153P/Ikeya-Zhang (C/2002 C1) (Dello Russo et al., 2004).

The g-factors are the product of: the Einstein A coefficient, the fractional population of the upper level of the transition and the branching ratio (which is equivalent

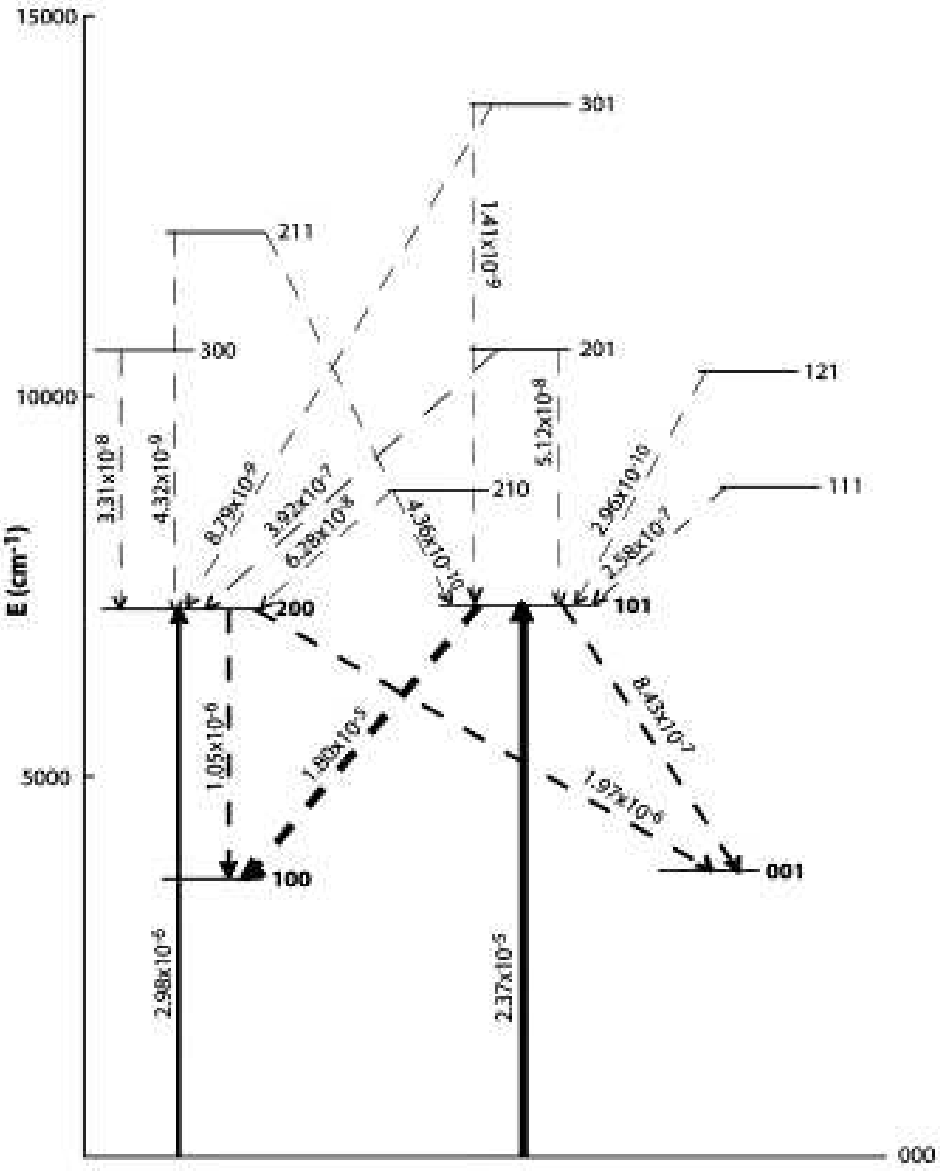

Figure 6.1: Schematic showing the vibrational bands involved in the formation of SPF lines: Reproduced from Dello Russo et al. (2004).

to the ratio of the Einstein A coefficient for the transition being considered to the sum of the Einstein A coefficients for all the routes by which the upper state may radiatively decay).

The upper state is able to be populated by two processes. It may be populated directly by pumping from ground vibrational states, where the rate of upward pumping is proportional to the product of: the incident solar flux at the pumping

frequency, the temperature-dependent population of the ground vibrational states, and the Einstein B coefficient of the upward transition. The upper state may also be populated indirectly by cascade from higher energy states, which have themselves been populated, either directly or indirectly, by pumping from ground vibrational states. The contribution to the population of the upper state arising from cascade from higher levels is dependent on: the population of these higher states, the Einstein A coefficients of the various allowed downward transitions, and their branching ratios. It will, of course be realised that this part of the calculation is itself complicated by non-LTE considerations. Finally it should be noted that, to a good approximation (except, as discussed in Section 6.1, where the water molecules were formed in the primordial Solar System at temperatures below 50 K), the OPR for H_2O is 3:1. The triple degeneracy of the ortho state needs to be taken into account when computing transition probabilities..

It will be seen that the computation of the temperature-dependent intensity of a single non-fluorescent line is a complicated matter. The process may be simplified by excluding low contribution cascade routes without impacting on the accuracy of the retrieval of the rotational temperature. Ultimately, the only factors impinging on the temperature-dependent fluorescence efficiency g(T) are: a knowledge of the allowed upwards and downwards transitions, and the various Einstein A and B coefficients, together with the solar pumping fluxes at a range of frequencies. The methodology makes several assumptions, which have varying degrees of validity. These are listed in the next section.

6.2.1 Working assumptions

- Under the influence of solar radiation, water molecules sublime, either from the comet surface (a 'direct source') or from small icy-dust particles which are driven from the surface by gaseous outbursts (a 'distributed' source). The ro-vibrational temperature of the molecules when they enter the gaseous phase is determined by the temperature of the surface from which they have sublimed. However, the molecules are vibrationally de-excited by collisions within the first ~500 metres of the inner coma, adopting a rotational Boltzmann energy distribution that is characteristic of the temperature of the inner coma, and is lower than the sublimation temperature.

- Solar photons and electron collisions pump H_2O molecules from these low energy pure rotational states into ro-vibrationally excited states. The transitions are optically thin.

- Away from the nucleus, the collisional rate is too low to maintain the water molecules in excited ro-vibrational states and they have time to decay radiatively to ground vibrational states, mainly by single direct transitions, but also via cascades to intermediate vibrational states. These are the fluorescent transitions that we refer to as 'SPF'. They are optically thin.

- Pumping due to infrared emissions from dust can be ignored in the near infrared.

6.2.2 Procedure

Dello Russo et al. (2004) made observations of comet 153/Ikeya-Zhang during seven observing periods, using the echelle spectrometer CSHELL at the NASA Infrared Telescope Facility on Mauna Kea, Hawaii, in three frequency ranges, centred on: 2 003, 2 144 and 3 452 cm^{-1}.

The favourable apparition of the comet, allowed detections of multiple water lines from at least six different hot-bands (see Table 6.1). A total of 17 lines (some of which could not be resolved individually) were identified in the 7 vibrational bands that were being targeted. Each band has $\sum_{J=0}^{J=7}(2J+1)$, i.e., 64 transitions.Transitions were observed from upper energy levels having all J values $\leq$6, but the percentage observed for any given upper J value was proportionately greater in the case of J $\leq$3 than for higher J values.

H_2O band	H_2O line	ν rest (cm^{-1})	$E_u - E_u(0_{00})$ (cm^{-1})	$g_{100\ K}$[a] $10^{-8}\ s^{-1}$	$g_{120\ K}$[a] $10^{-8}\ s^{-1}$	$g_{150\ K}$[a] $10^{-8}\ s^{-1}$
100–010	2_{12}–3_{03}	2003.00	79.50	22.1	20.6	18.4
100–010	1_{01}–2_{12}	2003.39	23.79	41.7	36.0	29.5
001–010	3_{22}–3_{21}	2137.33	206.30	6.84	8.06	9.12
001–010	0_{00}–1_{01}	2137.37	0.00	48.7	39.5	30.2
001–010	2_{12}–2_{11}	2139.92	79.50	5.00	4.59	4.02
100–010	2_{21}–1_{10}	2148.19	134.90	14.2	14.5	14.4
001–010	1_{11}–1_{10}	2151.19	37.14	45.4	39.8	33.0
111–110	5_{15}–6_{16}	3448.72	326.63	0.94	1.28	1.68
101–100	6_{06}–7_{07}	3448.74	446.70	4.79	8.26	13.7
101–100	6_{16}–7_{17}	3448.83	447.25	1.58	2.73	4.55
101–100	5_{24}–6_{25}	3449.38	416.21	4.74	7.78	12.3
200–001	1_{10}–1_{11}	3450.29	42.37	10.2	8.87	7.35
101–100	2_{02}–3_{21}	3453.15	70.09	6.93	6.07	5.08
200–100	1_{10}–2_{21}	3453.30	42.37	7.27	6.31	5.23
101–001	2_{11}–2_{20}	3454.69	95.18	4.60	4.16	3.59
200–100	3_{03}–4_{14}	3455.98	136.76	4.03	4.14	4.07
101–100	4_{22}–5_{23}	3456.45	315.78	7.31	9.67	12.4

Table 6.1: Log of water lines detected in Comet Ikeya-Zhang and their computed g(T) factors at 100, 120 and 150 K. Reproduced from Dello Russo et al. (2004).

6.2.3 Modelling SPF intensities

In order to be able to calculate rotational temperatures from observed line intensities it is necessary to develop models to describe how individual line intensities vary as a function of temperature. Figure 6.1 shows the routes by which the upper state of an SPF line are populated. It also indicates that there may be other routes by which this upper level can radiatively decay. The temperature-dependent probabilities of all the upward and downward transitions that affect the intensity of the SPF line in question need to be built into the model. At a given temperature, the probability of the upward transition is proportional to the Einstein B coefficient of that transition and in the case of downwards transitions, to the Einstein A coefficient. The Einstein A coefficient is an output of spectra-BT2.f90 and the Einstein B coefficient is related to the Einstein A coefficient by the expression:

$$\frac{A}{B} = \frac{8h\pi\nu^3}{c^3} \tag{6.1}$$

where A and B are the Einstein A and B coefficients and h is Planck's constant.

Figure 6.1 details the main upwards and downwards vibrational bands that need to be considered in order to calculate the temperature-dependent intensity of the SPF transitions in the (101)→(100) band. The true situation is more complex than is indicated in this figure, since, for ease of illustration, the figure only deals with changes in the vibrational quantum number. In reality fully rotationally resolved transitions need to be considered.

Various routes are shown by which the upper (101) vibrational state may be populated. One is by pumping from the ground vibrational state (assumed to be characterised by a Boltzmann distribution) (101)←(000). It may also be populated by cascade from higher vibrational states, including, but not restricted to, the ones shown in Figure 6.1: (211), (301), (201), (121), (111). However, it is generally the case that each of these higher states may decay to levels other than the (101) state that we are interested in. For example, the (201) state decays, *inter alia* to the (200) or (101) vibrational states. These higher levels are themselves able to be populated by a combination of upwards and downward routes.

Finally, account needs to be taken of the fact that the upper level, (101) is able to decay by transitions other than the one, (101)→(001), that we are concerned with here. Figure 6.1 shows an alternative route, (101)→(100), but the number of possibilities increases when changes in rotational angular momentum are considered.

A considerable number of transitions may need to be taken into account to determine the temperature-dependent intensity of a single SPF transition, particularly having regard to the contribution due to cascade from higher states. In order to simplify the calculation, Dello Russo et al. (2000) assume that the transition probabilities within a hot-band such as: (101)→(001) are the same as those for the corresponding fundamental transition: (001)→(000), and use as a starting point absorption line strengths for fundamental bands tabulated in Rothman et al. (1992), only using BT2-derived Einstein A coefficients to compute the direct pumping rates and branching ratios. Despite this simplification, the computation of the intensity of a single SPF line at a given temperature requires many inputs, and in particular Einstein A and B coefficients from BT2. The computed intensity of a SPF transition at a given temperature is expressed in terms of g(T). In Table 6.1 computed values of g(T) are given for 10 SPF transition in the 2.9 μm (3 450 cm^{-1}) region at three temperatures: 100, 120 and 150 K.

6.2.4 Selection of lines

In some spectral regions, many of the strong fluorescent lines have g-factors whose variations with temperature are very similar to each other (the transitions are pumped from states with similar lower state rotational energies), while other lines that might otherwise be better suited for a rotational temperature analysis are often too weak, or are accidentally coincident with telluric absorption features. To minimise these problems Dello Russo et al. (2004) targeted water hot-band lines near 2.9μm. This region contains several strong fluorescent lines as is seen from Figure 6.2.

Details of these lines are given in Table 6.1 (which also contains details of some strong SPF transitions at other wavelengths).

Using hot-band lines at 2.9μm Dello Russo et al. were able to derive H_2O rotational temperatures on three dates. All lines at 2.9 μm were used in this analysis except the (101)[422]→(100)[523] line with rest frequency 3456.45 cm^{-1}. This line was excluded because it is believed to be blended with an unknown emission feature.

6.2.5 Results

The rotational temperature of the comet was determined on three dates. By comparing the values of g at various temperatures with the transmittance-adjusted, measured line fluxes, it was possible to deduce the rotational temperature of the comet. These are: 138^{+6}_{-5}, 141^{+10}_{-9} and 94±3 K on UT 2002 March 22.0, March 23.0

and April 13.8, respectively.

The results imply that the rotational temperature decreased by about 40-50 K between UT March 22.0 (R_h = 0.51 AU) and UT April 13.8 (R_h = 0.78 AU) (See Table 6.1). This is not unexpected, since the comet was receding from the Sun during this period of time. A decrease in T_{rot} with heliocentric distance is to be expected, although the R_h-dependence can vary (Biver et al., 1999, 2002; Dello Russo et al., 2000; DiSanti et al., 2001). The formal relationship derived from Dello Russo et al.'s results for Ikeya Zhang is $T_{rot} = (74\pm\ 4)[R_h^{(-0.93\pm0.11)}]$ K.

6.3 Nuclear spin temperatures of three comets

The hot-band transitions identified by BT1 in Section 6.2 were classified into ortho and para using the symmetry information contained within the BT2 energy file (see column C, Table 3.1).

Using this information it was possible to deduce the primordial O/P water composition of three comets: C/1999 H1, C/1999 S4 and C/2001 A2 (Dello Russo et al., 2005), and hence the nuclear spin temperatures. These temperatures are thought to relate to the primordial temperatures of the different regions of the early solar nebula in which the comets were formed (Dello Russo et al., 2004). The method takes as its starting point the fact that O-P and P-O transitions are not allowed.

Spectra of these three comets were obtained in the 2.9 μm region using the high resolution spectrometer, NIRSPEC at the Keck Observatory, Hawaii, and a number of fluorescent transitions were recorded in these spectra. By separating the observed transitions into two groups, ortho (O) and para (P), and using the relative intensities of the O transitions to derive a rotational temperature and comparing the relative intensities of the O and P transitions with the ratios that would have been expected from a normal (3:1 OPR), it was possible to deduce the actual O/P degeneracy ratio and hence a nuclear spin temperature for the water molecules contained in the comet.

The detectability of emission lines near 2.9 μm is particularly sensitive to the atmospheric water burden. H_2O emission features were separated from the continuum by subtracting the normalised atmospheric model from the comet spectrum row by row, yielding the net cometary molecular emission intensities along the slit (convolved with the atmospheric transmittance function). The true line flux (F_{line}) incident at the top of the terrestrial atmosphere was determined by dividing the observed flux by the monochromatic transmittance at the Doppler-shifted line position.

In order to obtain the rotational temperature, production rate, and OPR from measured line fluxes, the g-factors for individual ro-vibrational lines are needed for a range of temperatures. Fluorescence models were produced for seven hot bands in the 2.9 μm region, based on the methodology discussed in Section 6.2.3 and detailed in Dello Russo et al. (2000, 2004). Due to the limited amount of laboratory data determination of g-factors for the H_2O SPF transitions, BT1 was used to generate the Einstein A coefficients. These values were revisited at a later date, when BT2 had been computed, and there were found to be no significant differences in the values obtained from the two lists for the transitions in question (the main differences between the Einstein A coefficients in BT1 and BT2 occur in weaker transitions).

In Section 6.2, lines from six hot bands were detected near 2.9 μm. The vibrational assignments for these six bands are 101→001, 101→100, 200→100, 200→001, 110→010, and 111→110.

For each comet, the individual fluxes from all measured lines were initially used in determining rotational temperatures and OPRs. Production rates were determined for each line individually, based on the initially measured rotational temperature and OPR. Lines that gave systematically deviant production rates i.e., systematically higher or lower than the mean (90% confidence level) were excluded from the analysis. Four lines were excluded for S4 and Lee on all dates, and three lines were excluded on the July dates for A2. No lines were excluded in the August A2 analysis. Production rates, rotational temperatures, and OPRs were then recalculated (excluding deviant lines) for all comets and on all dates. The presence of systematically deviant lines suggests possible errors in the rotational branching ratios in the fluorescence models or may, in the case of systematically high figures, be due to blending with unknown emissions. N. Dello Russo of Johns Hopkins University Applied Physics Laboratory has applied to the US National Science Foundation for funding to investigate these systematically deviant lines, naming the author of this Ph.D.as a collaborator in the project.

A knowledge of T_{rot} is required in order to calculate the H_2O production rates from individual line intensities. T_{rot} in the ground vibrational level is estimated by comparing the transmittance-corrected H_2O line fluxes (F_{line}) with their calculated temperature-dependent g-factors (g_{line}), using all measured lines in the 2.9 μm region. The rotational temperature was measured on two dates for comets Lee and A2 and on one date for comet S4. The derived nuclear spin temperatures of water released from comets A2, Lee, and S4 were computed to be 23^{+4}_{-3}K, 30^{+15}_{-6}K, and $\leq$30 K respectively (from a weighted average of the two dates on which OPRs were measured in Lee and A2).

TABLE 2
H_2O Lines Analyzed near 2.9 μm

Rest Frequency (cm^{-1})	Vibrational Assignment	Rotational Assignment	Nuclear Spin Species	Dates Detected (UT)		
				Lee	S4	A2
3347.907	101–001	2_{20}–3_{31}	Ortho	1999 Aug 19.6, 21.6	None	None
3348.355	200–001	3_{22}–4_{23}	Para	1999 Aug 19.6, 21.6	None	None
3358.922	200–001	3_{03}–4_{04}	Ortho	1999 Aug 19.6, 21.6	None	2001 Jul 9.5, 10.5
3360.990	200–001	3_{13}–4_{14}	Para	None	None	2001 Jul 9.5, 10.5
3362.310	101–001	2_{12}–3_{21}	Para	1999 Aug 19.6, 21.6	None	None
3366.554	200–100	3_{22}–4_{31}	Para	1999 Aug 19.6, 21.6	None	None
3371.692	200–100	3_{13}–4_{22}	Para	1999 Aug 19.6, 21.6	2000 Jul 13.6	None
3372.754[a]	200–001	2_{21}–3_{22}	Ortho	1999 Aug 19.6, 21.6	2000 Jul 13.6	2001 Jul 9.5, 10.5
3378.484[a]	200–001	2_{02}–3_{03}	Para	1999 Aug 19.6, 21.6	None	2001 Jul 9.5, 10.5
3382.100	200–001	2_{12}–3_{13}	Ortho	1999 Aug 19.6, 21.6	2000 Jul 13.6	2001 Jul 9.5, 10.5
3387.541[a]	101–001	4_{04}–5_{15}	Ortho	1999 Aug 19.6, 21.6	2000 Jul 13.6	2001 Jul 9.5, 10.5
3390.017[a*]	101–100	2_{12}–3_{31}	Para	1999 Aug 19.6, 21.6	2000 Jul 13.6	None
3390.039[a*]	200–001	4_{14}–4_{13}	Ortho	...	...	...
3390.092[a*]	101–001	4_{14}–5_{05}	Para	...	...	...
3394.076	200–100	2_{21}–3_{30}	Ortho	1999 Aug 19.6	None	None
3397.628	101–001	1_{11}–2_{20}	Ortho	1999 Aug 19.6	None	None
3399.368	200–001	1_{01}–2_{02}	Ortho	1999 Aug 19.6	None	None
3404.243	101–001	1_{10}–2_{21}	Para	1999 Aug 19.6	None	None
3404.997	101–001	3_{03}–4_{14}	Para	1999 Aug 19.6	None	2001 Jul 9.5, 10.5, Aug 4.4, 10.5
3409.203	110–010	3_{30}–4_{41}	Ortho	1999 Aug 19.6	None	None
3410.577	101–100	6_{24}–7_{25}	Ortho	None	None	2001 Jul 9.5, 10.5
3411.613	101–001	3_{13}–4_{04}	Ortho	1999 Aug 19.6	None	2001 Jul 9.5, 10.5, Aug 4.4, 10.5
3412.924	200–100	2_{12}–3_{21}	Ortho	1999 Aug 19.6	None	2001 Jul 9.5, 10.5, Aug 4.4, 10.5
3415.699	101–100	3_{03}–4_{22}	Para	1999 Aug 19.6, 21.6	2000 Jul 13.6	2001 Aug 4.4, 10.5
3417.659*	200–100	3_{12}–4_{23}	Ortho	1999 Aug 19.6, 21.6	None	2001 Jul 9.5, 10.5
3417.775*	101–001	3_{22}–4_{13}	Ortho	...	...	...
3422.329	101–001	2_{02}–3_{13}	Ortho	1999 Aug 19.6, 21.6	None	None
3426.582	101–100	6_{15}–7_{16}	Ortho	None	None	2001 Jul 9.5, 10.5
3428.303	200–001	2_{12}–2_{11}	Ortho	1999 Aug 19.6, 21.6	2000 Jul 13.6	None
3434.330*	200–100	2_{11}–3_{22}	Para	1999 Aug 19.6, 21.6	2000 Jul 13.6	2001 Jul 9.5, 10.5, Aug 4.4, 10.5
3434.382*	101–100	4_{14}–4_{31}	Para	...	...	...
3434.399*	101–001	2_{12}–3_{03}	Para	...	...	...
3435.490	200–001	3_{22}–3_{21}	Para	1999 Aug 19.6, 21.6	None	2001 Jul 9.5, 10.5
3436.633*	101–001	4_{04}–4_{13}	Ortho	1999 Aug 19.6, 21.6	None	None
3436.643*	101–100	5_{33}–6_{34}	Ortho	...	...	...
3439.423	101–001	1_{01}–2_{12}	Para	1999 Aug 21.6	None	2001 Jul 9.5, 10.5, Aug 4.4, 10.5
3439.826	200–001	1_{11}–1_{10}	Para	None	None	2001 Jul 9.5, 10.5, Aug 4.4, 10.5
3445.885	200–001	2_{20}–2_{21}	Para	1999 Aug 21.6	None	2001 Aug 4.4, 10.5
3448.722*	111–110	5_{15}–6_{16}	Ortho	1999 Aug 19.6, 21.6	None	None
3448.742*	101–100	6_{06}–7_{07}	Ortho	...	...	...
3448.829*	101–100	6_{16}–7_{17}	Para	...	...	...
3449.376	101–100	5_{24}–6_{25}	Ortho	1999 Aug 19.6, 21.6	None	2001 Jul 9.5, 10.5
3450.294	200–001	1_{10}–1_{11}	Ortho	1999 Aug 19.6, 21.6	2000 Jul 13.6	2001 Jul 9.5, 10.5, Aug 4.4, 10.5
3451.089	101–001	4_{13}–4_{22}	Ortho	1999 Aug 21.6	None	2001 Jul 9.5, 10.5
3453.154*	101–100	2_{02}–3_{21}	Ortho	1999 Aug 19.6, 21.6	2000 Jul 13.6	2001 Jul 9.5, 10.5, Aug 10.5
3453.300*	200–100	1_{10}–2_{21}	Ortho	...	...	...
3454.689	101–001	2_{11}–2_{20}	Ortho	1999 Aug 19.6, 21.6	2000 Jul 13.6	None
3456.445[a,b]	101–100	4_{22}–5_{23}	Ortho	None	2000 Jul 13.6	None
3458.117	101–001	0_{00}–1_{11}	Ortho	1999 Aug 19.6, 21.6	None	None
3459.493*	101–100	4_{31}–5_{32}	Ortho	1999 Aug 19.6, 21.6	None	None
3459.529*	101–001	1_{11}–2_{02}	Ortho	...	...	...
3463.196†	200–100	3_{22}–3_{31}	Para	1999 Aug 19.6, 21.6	None	None
3463.234†	200–100	3_{13}–4_{04}	Para	...	...	...
3467.676	101–100	4_{13}–5_{14}	Ortho	1999 Aug 19.6	None	None
3468.532*	101–001	2_{02}–2_{11}	Ortho	1999 Aug 19.6	None	None
3468.631*	101–100	5_{05}–6_{06}	Para	...	...	...
3468.652*	200–001	1_{01}–0_{00}	Ortho	...	...	...
3468.754*	111–110	3_{12}–4_{13}	Para	...	...	...
3468.870*	101–100	5_{15}–6_{16}	Ortho	...	...	...
3472.285†	200–100	4_{32}–5_{23}	Ortho	1999 Aug 19.6	None	None
3472.357†	111–110	3_{22}–4_{23}	Ortho	...	...	...

Note.—Asterisks (*) or daggers (†) indicate emissions that are combinations of two or more lines.
[a] Lines excluded from the analysis for all comets on all dates (see § 3).
[b] This line was detected and analyzed on three dates in comet 153P/Ikeya-Zhang (C/2002 C1) and was suspected of being a blended emission (Dello Russo et al. 2004), so it was excluded from this analysis since there are four total measurements of this line in our comet data archive (see text).

Table 6.2: Designation of H_2O lines in the region of 2.9 μm. Ro-vibrational and O/P assignments from BT2. Reproduced from Dello Russo et al. (2005).

The low nuclear spin temperatures measured in these comets suggest that their H_2O molecules probably formed on cold grains (with T_{spin} reflecting grain temperatures), rather than from exothermic gas-phase reactions (Tielens & Allamandola, 1987). Nuclear spin temperatures in comets A2 and Lee are much lower than derived rotational temperatures, suggesting that H_2O OPRs are not reset to the coma gas temperature upon sublimation from the nucleus.

It should be noted that, in principle, optical depth effects could simulate low OPRs. However, in practice, apart from within a distance of only a few kilometres (and possibly less) of the nucleus, the transitions that were measured were optically thin.

6.4 Water lines in comet Tempel 1

On 4th July 2005, NASA's Deep Impact mission successfully collided a 370 kg spacecraft (largely made of copper to minimise reactions with cometary water but including 6.4 kg of unspent hydrazine fuel) into the surface of comet 9P/Tempel 1 with an impact velocity of 10.3 km s^{-1}, releasing 19 GJoules of kinetic energy and ejecting dust and gas from the impact region that was studied by a nearby spececraft (A'Hearn et al., 2005; Feldman et al., 2005; Schultz et al., 2005) and from telescopes all over the world. The ground-based observations are reported in Meech et al. (2005).

We were successful in being awarded time on the United Kingdom Infrared Telescope (UKIRT), Muna Kea, Hawaii, to obtain spectra of Tempel 1 before and after impact. The principal objective was to determine the temporal development of those SPF water lines shown in Section 6.2 following the Deep Impact event.

Observations were made using CGS4, a cooled grating spectrometer with a 256 $\times$ 256 pixel array. The details given below relate to our observations on 4 July, post the Deep Impact event. Due to low intensity, CGS4 was unable to detect the comet prior to impact. However, immediately post-impact, considerable flux appeared, enabling us to record the evolution of the comet's spectrum with time.

Spectra were obtained in the wavelength range centred on 2.894 μm, with a spectral range of $\pm$0.040 μm. This wavelength region is the same as was selected for the investigation of the rotational temperature of Comet Ikeya-Zhang, see Section 6.2. Apart from containing many SPF transitions, see Figure 6.2, it was also known to be a spectral area which is largely void of other molecular lines (such as CO). This means that it is possible to model this region using the BT2 line list without having to include other species. However, in the subsequent examination of the data, in or-

der to maximise the S/N ratio, the analysis was restricted to the wavelength range: 2.8945 - 2.8985 μm.

It had been our intention to obtain spectra of Tempel 1 on the night prior to impact, on impact night, and on the night after impact. However, prior to impact the comet was not sufficiently bright to be able to obtain useful data, and on the night after impact, reduced intensity and a deterioration in the observing conditions prevented high quality data being obtained. Our results therefore relate only to the period of 144 minutes immediately following impact.

Cometary spectra were produced using normal techniques for observing in the infrared L band. Flat field and standard star frames were obtained at the beginning an end of the observing session. The ABBA mode removed the requirement for a dark frame (as discussed below).

An individual spectrum was obtained with four co-added 10 s exposures, repeated four times in 2x2 sampling so that the effects of bad pixels were minimised. Each spectral frame thus corresponded to 160 s exposure.

The telescope was first positioned such that light from the comet fell onto Row 95 of the detector. After an initial observation, the A frame, the telescope was nodded $10''$, so that light from the comet continued to fall on the spectrometer slit, but on a different row of the detector, Row 117. This produced a B frame. It was important when setting up the 'nod' parameters to ensure that both the A and B signals were centred on pixel rows, as the signal was from the spatially compact inner coma. A subsequent examination of the data revealed that approximately 70% of the signal was contained within a single pixel row.

The observing was of continuous ABBA quads, each quad being obtained over a period of 12 minutes. The quads were summed or sampled as required. To produce the spectra and to investigate their temporal evolution, sequential pairs of spectral frames were subtracted. This process has the effect of both 'dark framing' and sky subtracting, which are consequently not conducted separately. The subtraction leaves an A-B frame, which has a positive spectrum of the comet in Row 95 and a negative spectrum in Row 117. Finally the spectrum in Row 117 is extracted and subtracted from that extracted from Row 95. This final process has the effect of correcting for any change in the sky signal that may have occurred between the frames.

The net result is a spectrum that has an effective 320 s exposure, obtained (because of overheads such as nodding the telescope and reading out the detector array) over a period of 330 s. It should be noted that our analysis was confined to the signal in rows 95 and 117. No attempt was made to recover the small amount of

signal from adjacent rows as an analysis of the data revealed that this would have resulted in a reduction in the overall S/N ratio.

Because the signal was confined to two single rows, it was essential to achieve accurate tracking of the target. UKIRT's high accuracy guidance system made this possible and a subsequent analysis of the data revealed that there had been no detectable drift in the position of the signal on the array during the course of the evening. In order to identify water features, and to accurately measure their intensities, it was necessary to compensate for wavelength-dependent telluric absorption effects. This was particularly important in identifying the weak 'SH' lines that we discuss later.

The process of obtaining a true line flux is complicated by the fact that atmospheric transmittance varies not only with wavelength, but also with time. In theory we could have used our own sky data obtained at varying times during the evening. However, an examination of these sky data led to the conclusion that it would have the effect of introducing a new element of noise into the data. We therefore divided by a standard Keck sky spectrum, (Dello Russo, private communication), normalised to fit the water burden at UKIRT during the observations. It was subsequently learned (private communication) that this was the same process that had been employed by Mumma et al. (2005).

The detector was wavelength-calibrated by matching observed sky lines with those in the Kitt Peak sky atlas downloadable from:

ftp://ftp.noao.edu/catalogs/atmospheric_transmission/

and also by comparing with the Keck sky data, which has the advantage of having a similar water burden. The two sets of reference data (Keck and Kitt Peak) were found to differ by up to 0.000013 μm, which was equivalent to 0.36 of the pixel resolution of 0.0000362 μm. A second factor limiting the accuracy with which the observations could be wavelegth calibrated was the non-linearity of the detector. It was estimated that this could deviate from linearity by one pixel over the 2.8945 - 2.8985 μm region.

A detailed examination of the 24 A-B pairs revealed that sets 3, 4, 6, 11, 15 and 24 had excessively low S/N ratios and were therefore excluded. The post-impact total spectrum obtained by summing the other 18 A-B pairs, adjusted for a red shift of 9 km s^{-1} is shown in Figure 6.5 and covers the period July 4 05:54 to 08:11 U.T., but with 5 gaps each of $\sim$6 minutes duration starting at 6:06, 6:12, 6:24, 6:54 and 7:17 U.T.. The data have been adjusted to remove the continuum. The amount of intensity removed varies slightly across the wavelength range, but averages $3x10^{-16}$

$Wm^{-2}\mu m^{-1}$. The fact that some of the intensities in Figure 6.5 are negative may in part be due to having over-corrected for the continuum, or more likely is due to noise, which is estimated to be in the region of $0.4x10^{-16}$ Wm^{-2} μm^{-1}.

In Figure 6.5 two bright fluorescent transitions at 2.89580 and 2.89831 μm, stand out against a background of weaker features. Many of these weaker features are close to, or below, the noise threshold and these are disregarded. However, there are several where the S/N ratio is estimated to be greater than 4 and which, unlike noise, appear in the same place (albeit with differing intensities) in many of the individual frames. These are interpreted as also being genuine signals, and they are marked either SPF (where their wavelengths correspond to known fluorescent transitions), or SH, (in those cases where transitions are thought to be by some other route). The first column of Table 6.3 gives the observed wavelength of each of the features (adjusted for red shift).

The position of many of the spectral features in Figure 6.5 can be replicated using the BT2 synthetic water line list. Some of these are identified as being due to one or two individual lines whilst others are blends of many transitions, and are therefore not easily assigned with either vibrational or rotational quantum numbers. Two different techniques were used to assign features in the observed spectra. The first was simply to use the documented positions of the SPF transitions (see Table 6.2), the wavelengths used being the experimentally-known values, which differ slightly from those computed using BT2. The Einstein A coefficients used to compute intensities as a function of temperature were the BT2 values. The second technique was used to identify features that did not correspond to known SPF transitions and which, as far as we are aware, have not previously been recorded in cometary spectra.

In attempting to identify the non-SPF features in the observed spectrum, a series of synthetic spectra were generated using BT2, some of which are shown in Figures 6.7 and 6.8. In order to improve the signal to noise ratio and also to lessen the significance of errors in the wavelength calibration of our detector, estimated to be in the region of 0.00004 μm (slightly greater than a single pixel width), the resolution of the observed data was artificially reduced from an instrument-limited $\sim$37 000 to a pixel-averaged limited value of $\sim$17 500 by taking a moving average of five pixels in the wavelength dimension. This assisted the process of matching the observed and synthetic data. It was subsequently learned that Mumma et al. (2005) had adopted a similar procedure (using a 3 pixel moving average) in the analysis of their Keck data of Tempel 1 (private communication). Figure 6.6 shows our observed spectrum with this artificially degraded spectral resolution. In this figure the vertical scale is terminated at a level well below the peak intensities of the two strongest SPF

Table 6.3: Assignments of SPF and previously unobserved SH lines in the post-impact spectrum of Tempel 1. The first column gives the observed wavelength of each of the features (adjusted for red shift), the next column identifies the transition: the vibrational quantum numbers are given in round brackets and the rotational quantum numbers in square brackets. The last three columns give: the experimentally-determined wavelength of the listed transition, the Einstein A coefficient computed using BT2, and our designation of type SPF or SH.

$\lambda_{observed}$ μm $\pm$0.00005	Identification (see text for notation)	$\lambda_{laboratory}$ μm	A_{if} s^{-1}	Type
2.89458	(101)[211] - (001)[220]	2.89462	1.9	SPF
2.89527	(103)[110] - (102)[110]	2.89526	53.5	SH
2.89527	(211)[322] - (210)[211]	2.89528	8.5	SH
2.89573	(210)[101] - (011)[000]	2.89570	5.1	SH
2.89580	(200)[110] - (100)[221]	2.89578	4.7	SPF
2.89591	(101)[202] - (100)[321]	2.89590	1.7	SPF
2.89723	(220)[212] - (021)[111]	2.89728	4.4	SH
2.89831	(200)[110] - (001)[111]	2.89830	6.6	SPF

transitions. This was done to aid identification of the weak transitions.

Figure 6.7 shows three synthetic spectra generated at 3 000, 4 000 and 5 000 K (assuming LTE), using the BT2 line list (with some corrections to the calculated wavelengths based on the available experimental data). In producing these spectra, we applied the restriction that only states with J$\leq$3 are included. The resolution in Figure 6.7 was set to be the same as Figure 6.6. Figure 6.8 shows another set of synthetic BT2 spectra generated at the same three temperatures, but this time including all J levels (up to 50). Some of the same features are observed as in Figure 6.6, but we note that Figure 6.7 matches the observed spectrum better than Figure 6.8 does. However, it should be noted that these synthetic spectra have been computed on the assumption of LTE, which is clearly not the case. Moreover, the mechanism behind the formation of the SH transitions is not known. Hence, a precise match between the intensity of the features in the observed and the BT2 synthetic spectra is not to be expected. It is, however, true for H_2O that those transitions where $\Delta\nu_3 = 1$ will be the strongest.

Figure 6.7 is therefore a high-v, low-J spectrum and it reproduces well the position (less-so, the intensities) of many of the non-SPF features in the low-resolution observed spectrum, Figure 6.6. It should be noted that similar features are observed in synthetic spectra generated for temperatures greater than 3 000 K and the appearances of the spectra vary little once $T_{vib} > 4\,500$ K, except for differences in the general levels of intensity. It is also noted that there are other features in the observed spectrum (Figure 6.6) that are replicated in the synthetic spectrum (Figure

6.7). These are also due to water emission. However, since they are produced by the blending of many overlapping transitions from different vibrational manifolds, it is not possible to assign them to one or two individual transitions. Hence they have not been labelled with ro-vibrational quantum numbers in Table 6.3.

The non-SPF transitions identified in Table 6.3 share certain common characteristics and they are labelled them 'SH' in order to convey the fact that we believe that they are likely to be of a similar physical origin, related either directly or indirectly (the transfer of energy may possibly be via electrons) to solar photons. It is possible that the production route involves H_2O molecules that have sublimed from the freshly exposed icy grains ejected by the impact. However, an understanding of the precise nature of these SH lines will require further research. We have recently learned that Villanueva et al. (2006) observed some previously unrecorded lines in the 2.8313 μm region in the post-impact spectrum of Tempel 1, which may be due to transitions from higher energy ro-vibrational states of H_2O. We plan to try and replicate these features using synthetic BT2 spectra. In addition, we will collaborate with M. Mumma in trying to identify several unidentified lines in Mumma et al., (2005) including the one marked with a question mark in Figure 6.9.

6.4.1 Assigning the features

Among the assigned features are fluorescent emission lines from levels that have two quanta of H_2O stretching, such as (2 0 0)$\rightarrow$(1 0 0) and (1 0 1)$\rightarrow$(1 0 0). In the former transition, the emission involves one quantum of ν_1, in the latter it involves one quantum of ν_3. A quantum of ν_1 and of ν_3, have similar energies $\sim$3 450 cm^{-1}. In both cases, the final state is the $1\nu_1$ state. Because a quantum of ν_2 carries less than half the energy of a ν_1 or ν_3 quantum, ($\sim$1 400 cm^{-1}), transitions involving a change of one quantum of ν_2 are not observed in our selected wavelength range.

The post-impact spectrum of Tempel 1 also includes several transitions from states that include one or two quanta of ν_2, and have a total of 3 or 4 vibrational quanta. These are not SPF spectral features. It will be seen from Table 6.3 that these include the blend of (1 0 3)$\rightarrow$(1 0 2) and (2 1 1)$\rightarrow$(2 1 0) at 2.8953 μm, and (2 2 0)$\rightarrow$(0 2 1) at 2.8972 μm. It seems likely that upper levels with more than two vibrational quanta have not been populated by solar pumping from ground vibrational states, but by another mechanism. Whereas SPF transitions originate from upper states having energies in the region of 7 300 cm^{-1}, the transitions labelled 'SH' all originate from higher energy states (those upper states having four vibrational quanta are in the energy range 10 300-14 400 cm^{-1}).

6.4.2 Comparison with other spectra

We have compared our results with the spectra obtained by Mumma et al. (2005).

As far as the positions of the observed SPF transitions are concerned, our results agree well with those of Mumma et al.. However, none of the SH features appear in Mumma et al.'s spectrum D. It is also noted that there is one strong feature in Mumma et al.'s spectrum at 3454.1 cm^{-1} that does not appear in our data. One possible reason for the difference between our results and those of Mumma et al. is the difference in times when the spectra were obtained. Our results were obtained between 05:54 and 08:11 U.T. on impact night, whilst Mumma et al.'s spectrum in Figure 6.9 were obtained between 6:43 and 7:25 U.T.. By summing the intensities of all the SH features, a degree of temporal resolution was achieved that was not possible for the individual lines. We observed that the total intensity of the SH features was particularly strong during the period 20–40 minutes after impact, but by 50 minutes after impact it had declined to a level that was only slightly above that of the background noise. This could be the reason why the features are not observed in Mumma et al.'s spectra..

Recently we obtained UKIRT spectra of Comet 73P/Schwassmann-Wachmann 3, fragment-C, in order to investigate whether this recently fragmented comet exhibits similar SH features to those that we observed in Temple 1. Preliminary investigation of the 73P spectra does not reveal any of the SH features.

6.4.3 Conclusions

The Deep Impact collision with Comet 9P/Tempel 1 released considerable amounts of fresh material, much of it from beneath the cometary surface.

The principal objective in observing the Deep Impact event was to investigate the temporal evolution of SPF lines in the spectrum of Comet Tempel 1, post-impact. However, with the exception of our comment about the temporal development of the integrated intensity of the SH features (see above), because of low S/N, we were not able to address this issue. Rather, our analysis wasconfined to spectral data integrated over the whole of the observing session.

We identified H_2O lines in the post-impact spectrum of Tempel 1 that had not previously been recorded in cometary spectra. We labelled these lines 'SH', but our designation should not be interpreted as implying that we understand the method by which they were produced. They would not appear to have been formed by the well-documented SPF mechanism, since the products of: the LTE populations of the low lying pure rotational states that are able to be pumped to the appropriate

upper level (by routes that are permitted by the selection rules), and the Einstein B coefficients of the upward transitions, are typically two or three orders of magnitude lower than for the SPF transitions.

We observe that these same emission features are present in synthetic BT2 spectra generated at temperatures of several thousand Kelvin, but not at lower temperatures. This may indicate that solar photons are involved in the process. If so, the mechanism could be an indirect one, possibly involving photo-ionization and electron-ion dissociative recombination (H_3O^+ has been suggested as a possible ion and a group at UCL, including S. Vitti and J. Tennyson is now examining this possibility). In any event, care should be exercised in drawing conclusions based on our synthetic spectra as these assume LTE conditions, which are unlikely to exist in the retion of the coma where the photons originate. It is also noted that these SH lines, which were strong during the period 20–40 minutes after impact were not observed in Mumma et al. (2005). This might possibly be explained by the fact that Mumma et al.'s Tempel 1 spectrum that includes this spectral region was obtained at a later time.

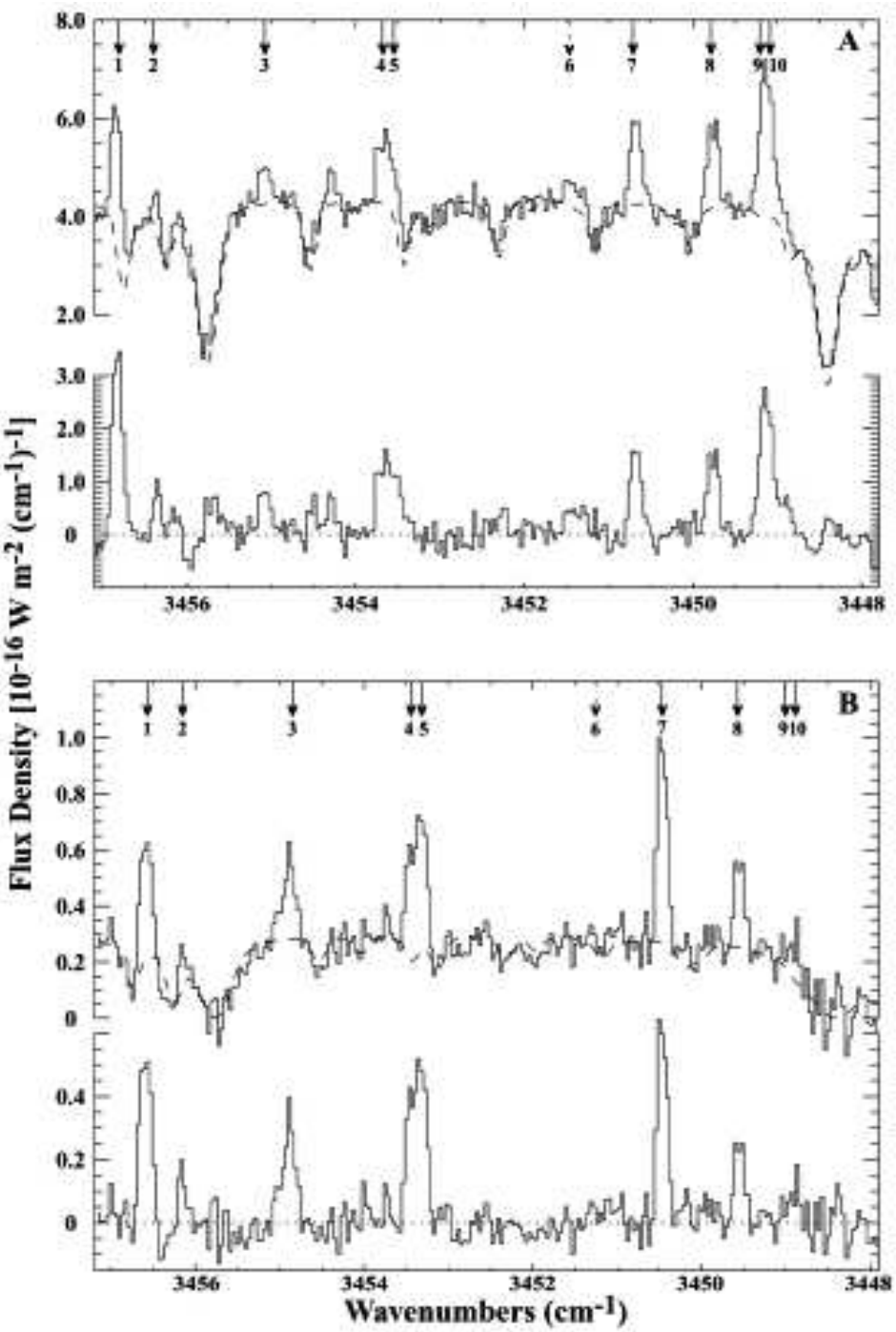

Figure 6.2: Detection of SPF lines in Comet Ikeya-Zhang. (A) UT 2002 March 22, 00:31, (B) UT 2002 April 13, 18:45. Top: flux-calibrated spectra. Bottom: flux-calibrated residual spectra. Labels relate to transitions in Table 6.1, numbering from the bottom upwards. Line 6, (101)[413]→(001)[422] is omitted from Table 6.1, and 10 is a blend of numbers 9 and 10 from the list in Table 6.1. Reproduced from Dello Russo et al. (2004).

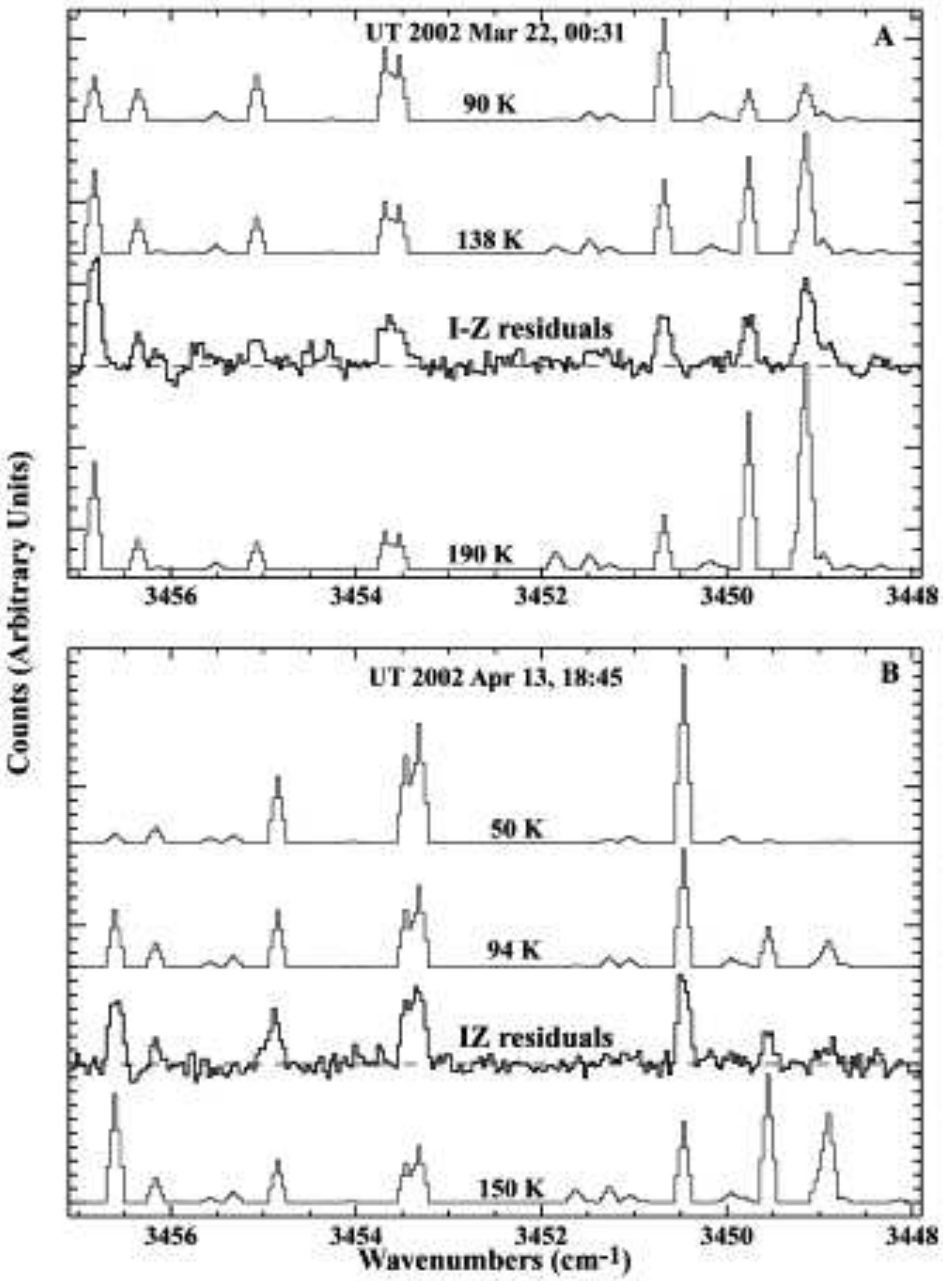

Figure 6.3: Comparison of Ikeya-Zhang residual spectral extracts (convolved with atmospheric transmittance functions) with modelled SPF features computed with Einstein A coefficients generated using BT1. The upper chart relates 22 March 2002 and the lower 13 April 2002. In each chart the top two and bottom plots are the modelled features computed at various temperatures. The second plot from the bottom in each chart is the residual of the observed spectrum and should be compared to the plot immediately above it, which is the model giving the best temperature fit. The best fit rotational temperatures are: (A) 138 K and (B) 94 K. Reproduced from Dello Russo et al. (2004).

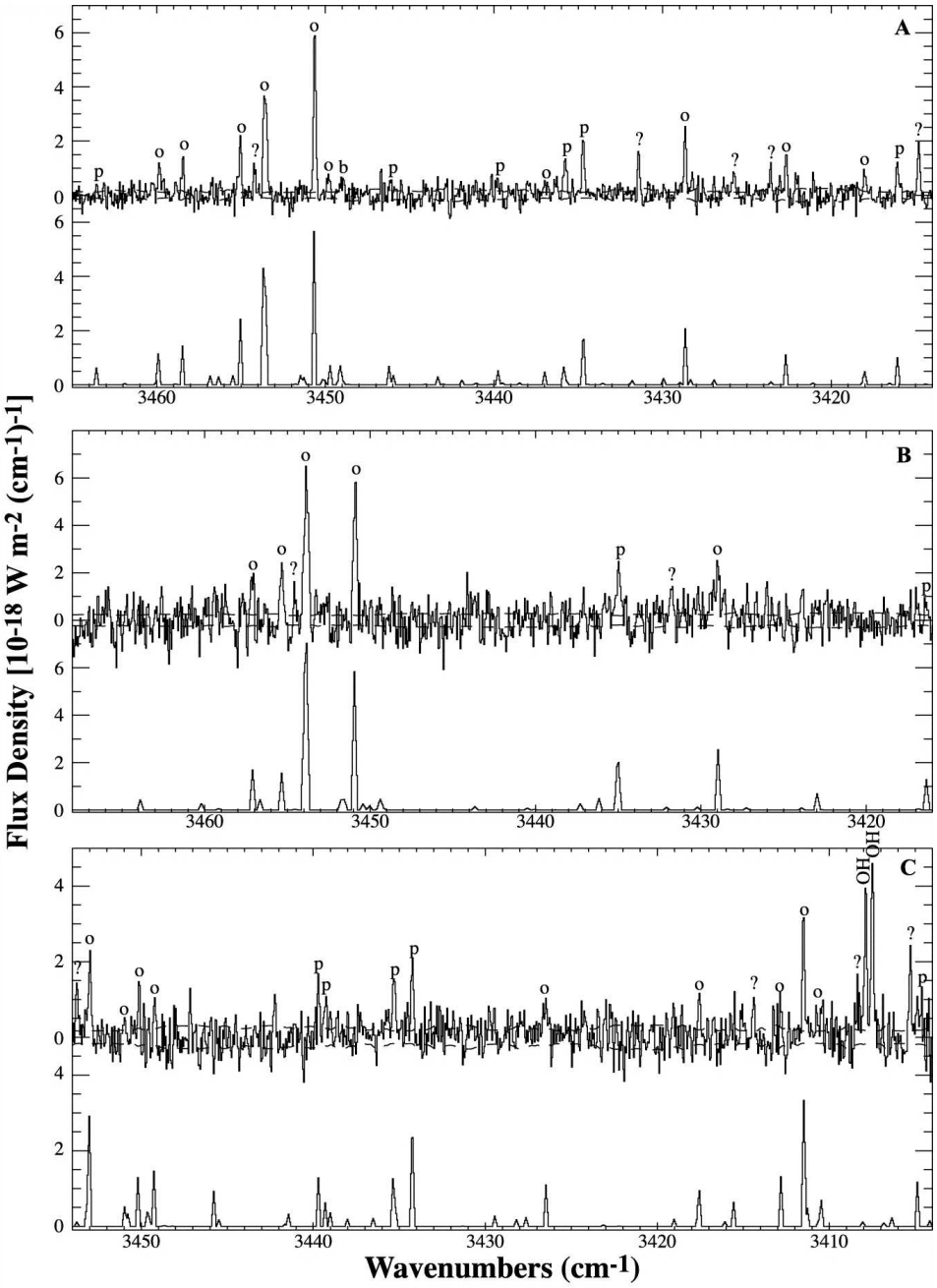

Figure 6.4: Comparison of the spectral residuals and BT2 O/P assignments [b=blend] (upper plot) with Dello Russo's fluorescence model (using Einstein A coefficients generated using BT2) at best fit temperatures. (A) Lee: 21 Aug 1999, T=76 K; (B) S4: 13 July 2000, T=73 K; (C) A2: 10 July 2001, T=105 K. Reproduced from Dello Russo et al. (2005).

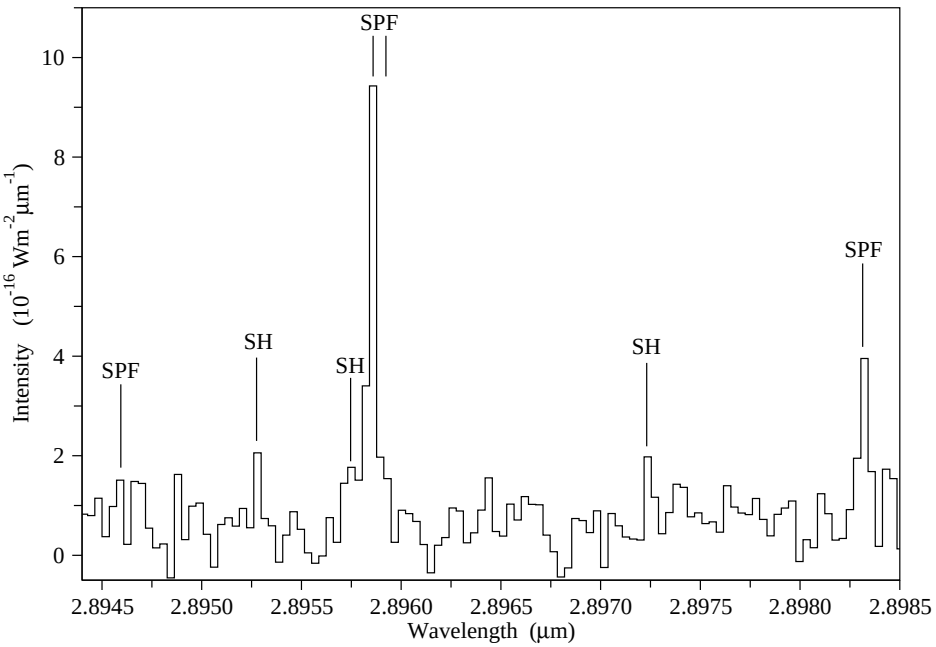

Figure 6.5: Observed post-impact spectrum of Tempel 1. Wavelength is in the rest frame.

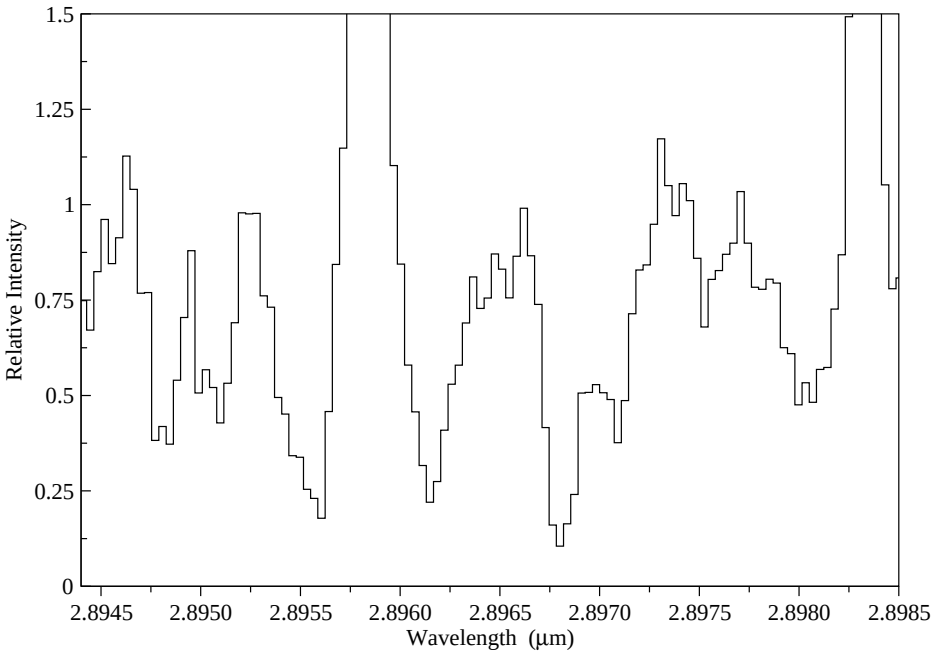

Figure 6.6: Observed post-impact spectrum of Tempel 1, resolution-degraded by using a moving average of 5 pixels. Wavelength is in the rest frame. The vertical scale has been limited to assist identification of the weaker features.

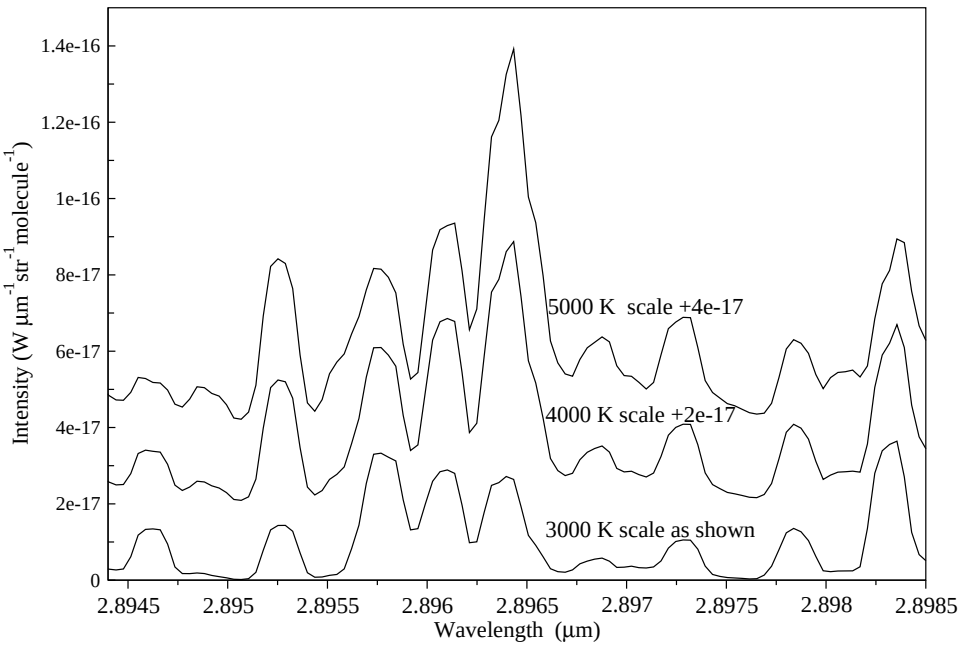

Figure 6.7: BT2 synthetic spectra at 3 000 K, 4 000 K and 5 000 K, J_{max}=3

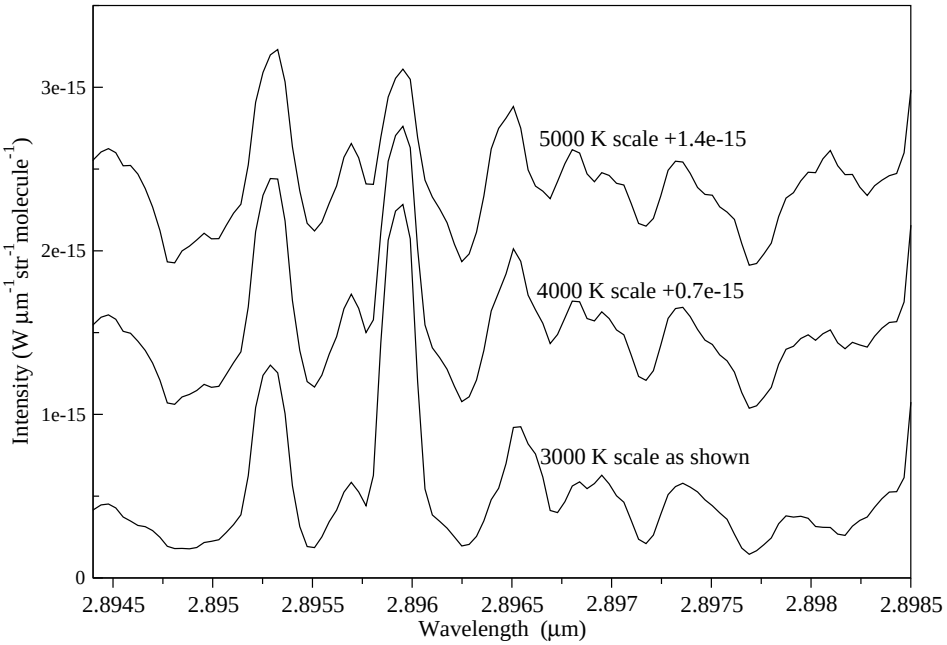

Figure 6.8: BT2 synthetic spectra at 3 000 K, 4 000 K and 5 000 K, J_{max}=50

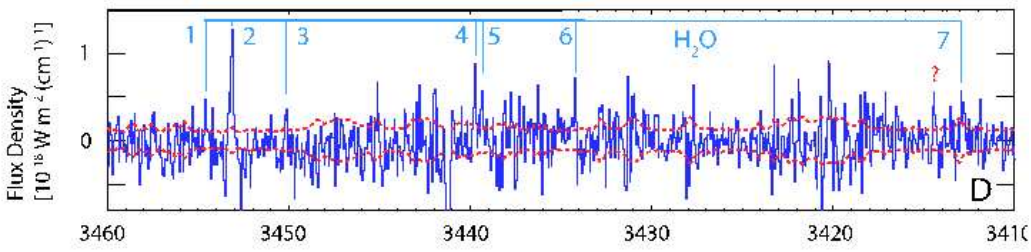

Figure 6.9: Spectrum of Tempel 1 post-impact (abscissa is frequency in units of cm^{-1}). Reproduced from Mumma et al. (2005).

Chapter 7

Cool stars and brown dwarfs

Our main motivation in producing a high accuracy synthetic water line list was that it is required for studying cool stars and brown dwarfs. Investigations of these objects may be divided into two areas: spectroscopy and atmospheric modelling. In the former case, the requirement is that the synthetic list should give the line positions and intensities to a high accuracy and that it should also assign all the strong transitions. In the latter case, the requirement is also for completeness, as line blanketing is important in radiative transfer models (Jørgensen 1994b, 1997; Allard et al., 1994). There is, however no requirement that the transitions should be labelled.

BT2 has been used on a number of occasions to analyse the spectra of cool stars and brown dwarfs and in modelling their atmospheres.

7.1 Cool giants and supergiants

Water features are known to exist in the spectra of cool giants and supergiants. Jennings and Sada (1998) were the first to identify individual rotational lines of water in the spectra of the M 1 supergiant, α Orionis (Betelgeuse), and in α Scorpii (Antares) an M 1.5 supergiant. Ryde et al. (2002), report the detection of water lines in α Bootes (Arcturus), a K 1.5 red giant. Water is not expected to be present in the atmospheres of stars hotter than M-type (Tsuji, 2001) and Ryde et al. suggest that the water in Arcturus may be formed in cooler convective regions in the upper photosphere.

The evolved envelopes of cool giants and supergiants are not in LTE (see Chapter 10). It is therefore not possible to use water lines as temperature indicators in the same manner as for cool dwarfs (see below), which because of their smaller diameters

and correspondingly higher surface gravities *are* in LTE. This was confirmed by some preliminary work on the spectra of giants/supergiants by Moont (2005). Working with a list of 39 pure rotational transitions generated by BT2 in the 11.18-11.21 μm region, Moont identified five water features that were all present in the spectra of five cool giants/supergiants observed using the Michelle spectrometer, R$\approx$ 15 000, on UKIRT, Hawaii, between 11-13 August 2002 (Viti et al., unpublished). The relative intensities of the lines were shown, *inter alia*, to depend on temperature, but Moont was not able to use the selected lines in a satisfactory manner to measure temperature.

It is anticipated that one of the bi-products of the author's planned collaboration with Harper and Ryde into the non-LTE modelling of the cool envelopes of M giants (see Chapter 10) will be the development of a method whereby BT2 may be used to derive the temperatures of the outer atmospheres of this class of stars.

7.2 M dwarfs

M dwarfs are the most common stars in the universe, and yet there are still many gaps in our knowledge of their fundamental properties. The boundary between late M dwarf stars and early brown dwarfs is blurred. In general, but certainly not in every case, M8 and M9 spectral types do not undergo sustained hydrogen burning, whilst earlier spectral classes are stars. The main problem in determining this boundary is related to the inability of stellar atmospheric models to produce synthetic spectra that match the observed spectra of these objects. Until recently it was believed that problems with the water opacity were responsible. However, recent work using BT2 discussed in Section 7.4.1 has demonstrated that the shortcoming is in fact elsewhere, most probably in these models.

One important aspect of the modelling of objects close to the stellar/brown dwarf boundary carried out by Jones et al. (2005a) has been the identification of spectral regions that are already reasonably well described by existing atmospheric models. In general terms, these models give better fits to the observed spectra at longer wavelengths, where the opacity is dominated by H_2O and CO absorption bands, than at shorter wavelengths where atoms and diatomic molecules (such as TiO and VO) dominate. A high quality water line list is essential for the accurate modelling of these longer wavelength regions.

7.3 Brown Dwarfs

Brown dwarfs are differentiated from stars in that they are not massive enough to permit sustained thermonuclear fusion of hydrogen. Their masses and temperatures are in a range that positions them between late M dwarf stars and gas giants. In the same way that the boundary between early brown dwarfs and late M dwarf stars is blurred, so are the boundaries between the various spectral classes of brown dwarfs: L, T and Y.

The low temperatures and small radii of brown dwarfs mean that they have very low luminosities, peaking in the near infrared. Consequently, they are very difficult objects to observe, and it is only 11 years since the existence of the first brown dwarf, Gliese 229B was confirmed (Oppenheimer et al., 1995). This object is a T dwarf having total luminosity, $L_{bol}=6.4\times10^{-6}L_{\odot}$, of which 50% is in the spectral region between 1.0 and 2.5 μm (Matthews et al., 1996), and $T_{eff}\approx900$ K (Matthews et al., 1996, using the Tsuji et al., 1996a dust-free model). Its spectrum, has an appearance similar to those of Jupiter and Titan (see Figure 7.1).

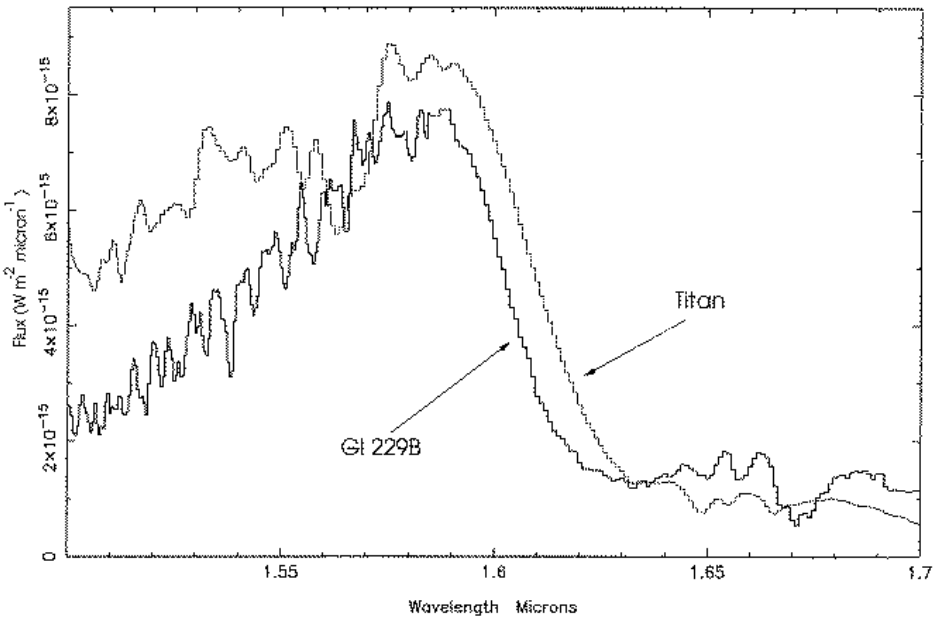

Figure 7.1: Spectrum of Gl 229B compared to that of Titan (scaled by ~0.003), near the 1.6 μm methane absorption edge. Reproduced from Geballe et al. (1996).

There is considerable interest in deriving the space density for stars close to the bottom of the main sequence and of sub-stellar objects (Jones et al., 1994). However, there are many uncertainties, particularly regarding the space density of

brown dwarfs.

Statistical modelling by Allen et al. (2005) tested against observational data contained in Reid et al. (2002) do not accurately constrain the sub-stellar Initial Mass Function (IMF). The models do, however, demonstrate that the Saltpeter relationship, that is generally assumed to hold for stellar objects, stating that the number of objects with a given mass is inversely proportional to the $\sim$2.4 power of the mass (Saltpeter, 1955), overestimates the population of objects having sub-stellar masses. Moreover, it is likely that the sub-stellar IMF is not able to be described by a simple Saltpeter-type model.

Problems associated with determining the IMF for brown dwarfs are detailed in Jones et al. (1994), and Pinfield et al. (2006). *Inter alia*, the scales used to convert the observed optical and infrared fluxes into bolometric luminosities and effective temperatures (and hence into estimates of masses) are not well defined.

The uncertainty over the IMF for brown dwarfs is a cause for concern amongst astronomers now searching for a new class of object earlier than T dwarfs, the so-called Y dwarfs (Pinfield and CDSWG, 2006). Collinge et al. (2002) suggest a space density for T dwarfs of one per 160 pc^3, and Pinfield and CDSWG have based their observing proposal on the assumption that Y dwarfs have a similar space density. However, until these objects are observed there is no evidence to support this assumption, and it is possible that the failure at the time of writing to detect any Y dwarfs (see below) may be due to a downturn in the IMF at these very low masses.

In recent years there has been a substantial increase in infrared observational activity both ground-based and from space. The 2 Micron All-Sky Survey, 2MASS, (Skrutskie et al., 2006) and the Deep Near-Infrared Survey, DENIS, (Epchtein, 1997) are being taken to larger telescopes; UKIRT in Hawaii is conducting the Infrared Deep Sky Survey (UKIDSS), WIRCam is operating on the Canada-France-Hawaii Telescope and the Visible and the Infrared Survey Telescope for Astronomy (VISTA) is due to come on stream next year. In space, NASA's Spitzer Space Telescope is also surveying in the IR.

As a result of this activity, the rate at which brown dwarfs are being discovered has accelerated and today in excess of 400 have been identified. The recent availability of large amounts of observational data for brown dwarfs means that the study of these objects is a rapidly developing field. In particular, attention has focussed on their spectra, which, because their atmospheres are rich in molecules, are both varied and complex (see Figure 7.2). Moreover, one important feature, that suggests that BT2 will become a useful tool in determining the temperatures and masses of

these objects (see Section 10.6) is the fact that the depth of the water absorption features increases with reducing temperature (see Figure 7.2).

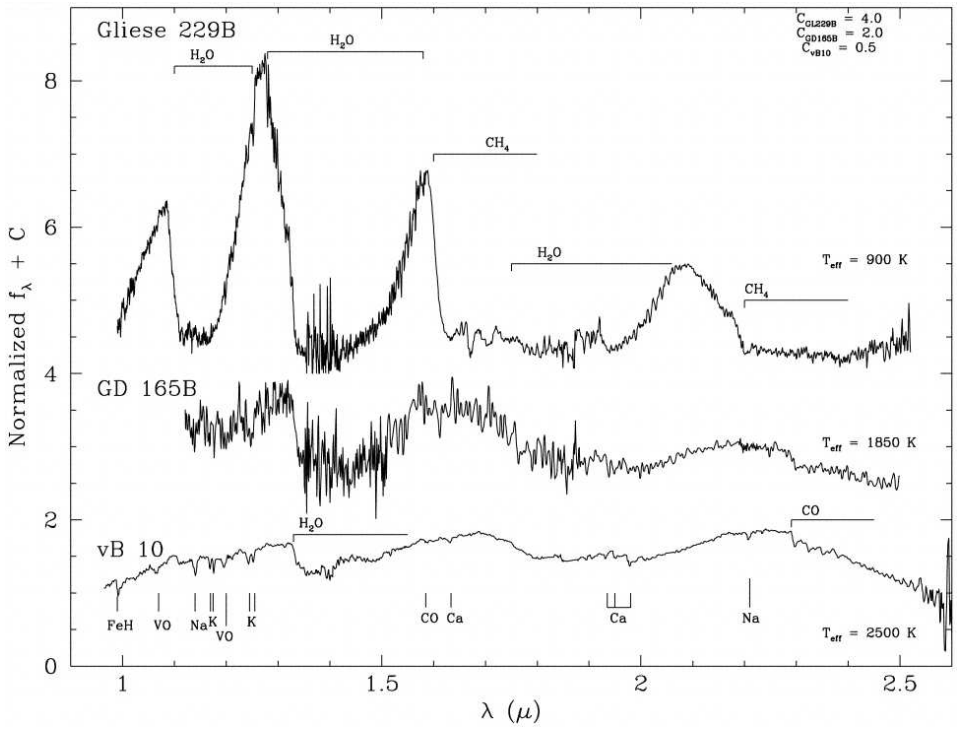

Figure 7.2: Spectra of three low mass objects: T dwarf Gliese 229B, L dwarf GD165B and a late M dwarf vB 10, illustrating how the depth of the water absorption features increases at lower temperatures. The vertical scales for the three plots are not comparable, the lines having been moved by arbitrary amounts in the vertical direction for ease of presentation. The figure is reproduced from Oppenheimer et al. (1998). Gliese 229B data were published in Oppenheimer et al. (1995) and Geballe et al. (1996), and those of the other two objects in Jones et al. (1994).

However, it is only when the atmospheres of brown dwarfs are able to be modelled satisfactorily that the physical parameters of the objects in terms of temperatures, pressures, metallicities and evolution will be properly understood. Consequently attention is also being focussed on developing more accurate atmospheric modelling.

Recent Spitzer images sugget that brown dwarfs have similar origins to stars and apart from having a lower mass than stars, their development over the first billion years closely resembles that of a star (previously the most likely production mechanism was thought to involve ejection from dense cores). It is only after this period, that their behaviours diverge. In the case of a star, the power derived from thermonuclear burning of hydrogen in its core balances the rate of photon loss from its surface. However, even though some of the more massive brown dwarfs ($\geq$0.065$M_{\odot}$) do burn hydrogen in their early stages, they never do so at a rate

fast enough to achieve this balance, since the parameter that ultimately determines the hydrogen-burning rate is mass (metallicity and opacity have a small impact on the hydrogen-burning limit). Broadly, those objects that have a mass less than $\sim 0.075 M_{\odot}$ (the precise figure depends on metallicity) are unable to achieve stable hydrogen burning (Baraffe et al., 1998).

The so-called 'lithium test' (Magazzù et al., 1991), which uses the lithium line at 6708 Å to distinguish between objects whose spectra exhibit lithium in absorption and those which do not, is a useful indicator of the hydrogen burning limit, and so provides a way of differentiating between stars and brown dwarfs near to the bottom of the H-R diagram. The actual mass limit for lithium burning depends on metallicity, but objects more massive than $\sim 0.065 M_{\odot}$ and with an age range between 30 and 300 Myr. will burn lithium isotopes via the $p + {}^{6}Li \rightarrow \alpha + {}^{3}He$ and $p + {}^{7}Li \rightarrow 2\alpha$ reactions (Burrows et al., 2001).

Objects more massive than $\sim 0.013 M_{\odot}$ will burn deuterium via the $p + d \rightarrow \gamma + {}^{3}He$ reaction (Burrows et al., 2001). In astronomical terms, this deuterium burning phase lasts only a short period, typically no more than 30 million years. In the same way that the lithium test is a useful indicator of the boundary between stars and brown dwarfs, the deuterium test is a useful, albeit approximate, way of differentiating between two classes of brown dwarfs: L and T (Chabrier and Baraffe, 1997; Chabrier et al., 2000). Depending on metallicity and gravity there is a considerable range in the temperatures corresponding to the limits of deuterium burning (Burrows et al., 2001), but in broad terms brown dwarfs with temperatures in the range $\sim$2 600 K to $\sim$1 500 K burn deuterium, whilst the cooler T dwarfs, whose temperatures range down to $\sim$750 K do not. It should be noted that a T dwarf with a temperature close to this theoretical limit has actually been observed - Gliese 570D (Burgasser et al., 2000).

Systematic observations are now being conducted to search for Y dwarfs which are below the deuterium burning threshold. These objects are predicted to have temperatures in the range $\sim$750–400K, spanning the gap between T dwarfs and planetary gas giants.

7.3.1 M and L dwarfs

The features that most accurately distinguish between M and L dwarfs are spectroscopic in nature, rather than being strictly temperature-based. Leggett et al. (2002a) indicate a temperature range of 2 200–1 300 K for L dwarfs. Their analysis of the various types of brown dwarfs are based on the ratios of the fluxes in the $JHKL'M'$ spectral bands. However, even this methodology is imprecise as there are variations

between the spectra of similar spectral class objects. In the case of L dwarfs, Leggett et al., suggest that the variations are due to dust.

In addition to the more general photometric intensity measurements, there are specific spectral features that aid the differentiation between M and L dwarfs. Whilst atoms and open shell diatomics are important in the spectra of late M dwarfs, the cooler L dwarf class is characterised by weakening VO and TiO absorption features in the red, and by stronger alkali metal and H_2O absorption features in the red and near-infrared (Delfosse et al., 1997; Kirkpatrick et al., 1999: Martín et al., 1999), see Figure 7.3. In addition, atomic lines can be used as key diagnostics of the atmospheres of M and L dwarfs.

We collaborated with Lyubchick and co-workers in analysing a series of high resolution spectra in the J band of five cool dwarfs from M6 to L0 (Lyubchik et al., 2006). Synthetic spectra were computed for comparison purposes using the VETA6 program (Pavlenko, 2000). This assumes local thermodynamic equilibrium, hydrostatic equilibrium, and solar metallicity. A mix of around 100 atomic and molecular species was used in computing chemical equilibrium. The molecular data and continuum opacities are described in Pavlenko et al. (2000). The atomic line list used was taken from the VALD database (Kupka et al., 1999) and the modelling was performed using two water line lists: the PS (AMES) list and the BT2 list.

Lyubchick et al. observed that BT2 produced more accurate models than PS. In particular, BT2 halved the amount of water opacity missing in the J band (1.6% of water opacity was missing when modelled using PS, whilst BT2 included 99.2% of the water opacity in the J band).

Overall, Lyubchick et al. (2006) concludes that a good fit is achieved by BT2 in the 1.281 to 1.301 μm and 1.327-1.333 μm regions, but the results are less satisfactory at wavelengths shorter than 1.3 μm, since the contribution of water to the total opacity at shorter wavelengths was typically less than 50% of that at the longer wavelength. These authors conclude that the limiting factor at shorter wavelengths is likely to be the quality of the diatomic line lists and cite FeH and CrH as being particularly important.

7.3.2 T dwarfs

Water is by far the most important source of non-continuum opacity of T dwarfs, with methane and CO also making significant contributions and ammonia becoming increasingly important for types later than T5. This is illustrated in Figure 7.5, which shows a near infrared spectrum of Gliese 229B (Oppenheimer et al., 1998). Continuum opacity comes from H^-, H_2^- and H_2 collision-induced absorption (Bur-

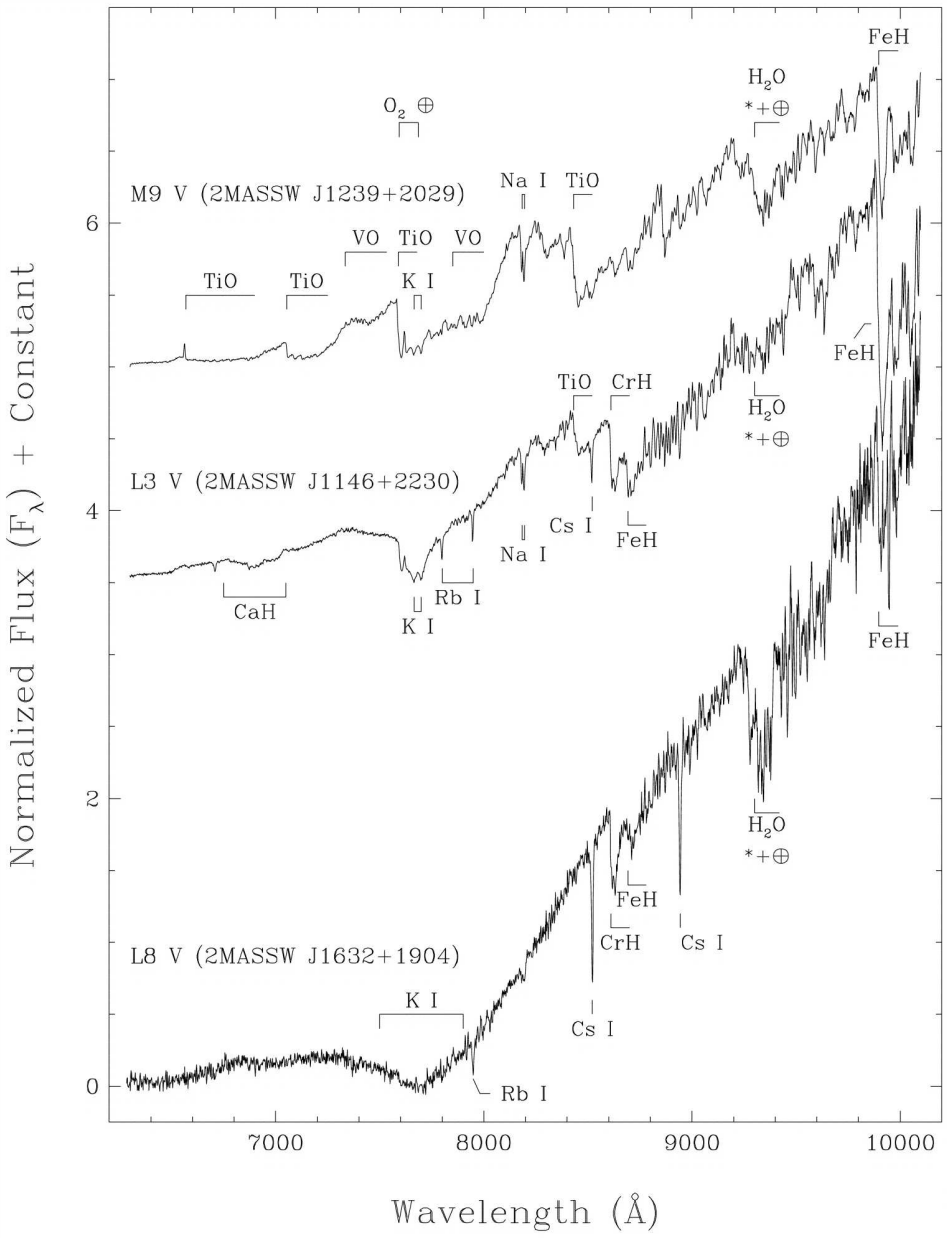

Figure 7.3: Spectra of a late M, early L and late M dwarfs in the red and near-infrared showing the disappearance of VO and TiO features in later type dwarfs and the deepening metallic hydride and H_2O absorption features. The vertical positions have been adjusted by arbitrary amounts for ease of presentation. Reproduced from Kirkpatrick et al. (1999).

rows et al., 1997). It is the presence of H_2O bands in brown dwarfs that makes such objects an obvious area of application for BT2.

ϵ Indi Ba and its companion, ϵ Indi Bb are, at a distance of 3.63 pc, the clos-

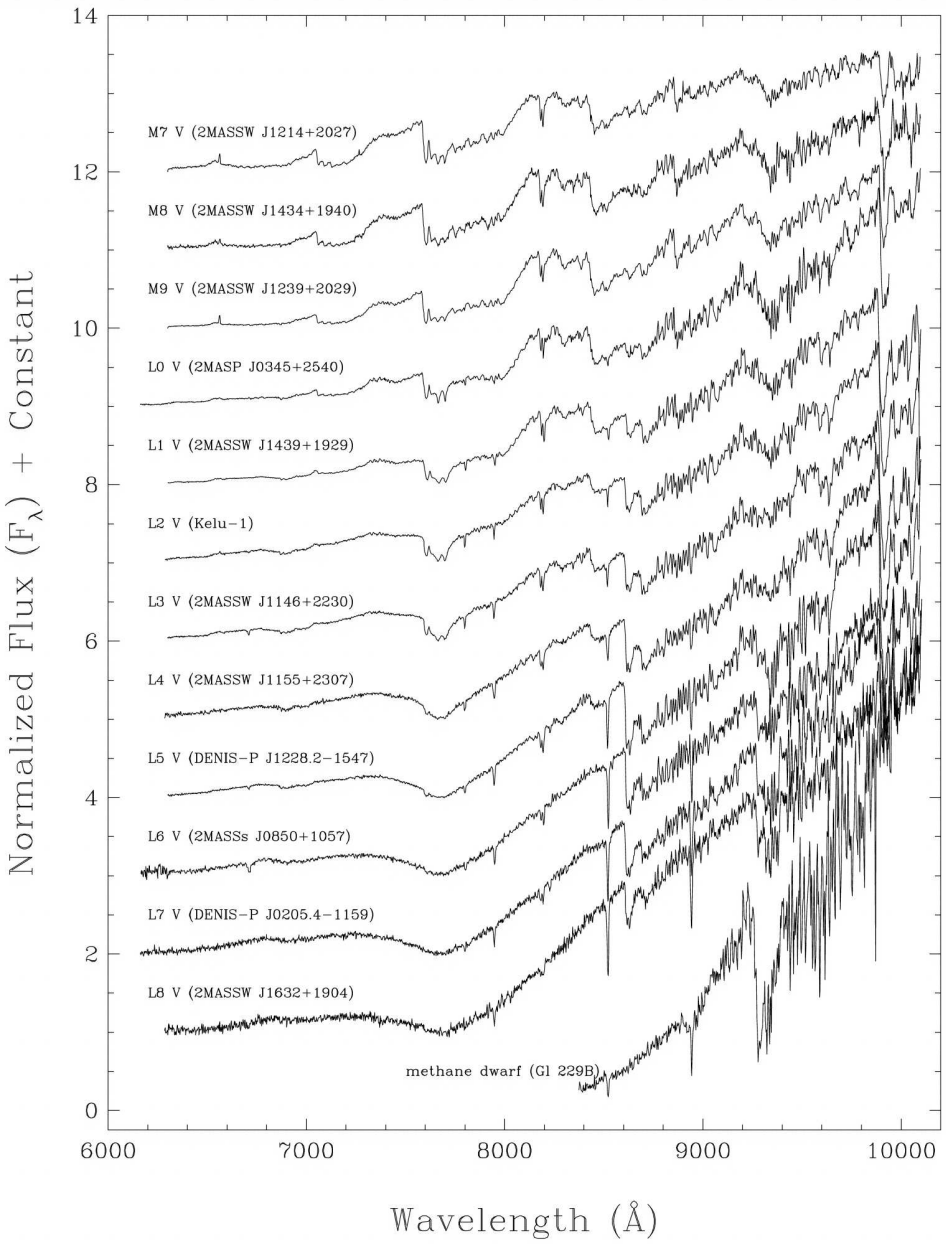

Figure 7.4: A series of spectra showing the development of complex molecular absorption features in later spectral types. The lowest plot is for T dwarf Gl 229B. The vertical positions have been adjusted by arbitrary amounts for ease of presentation. Reproduced from Kirkpatrick et al. (1999).

est known brown dwarfs to our Solar System. Scholz et al. (2003) observed that ϵ Ind had a T dwarf companion, but it was Volk et al. (2003) and McCaughrean et al. (2004) that subsequently discovered that this object was in fact a close optical

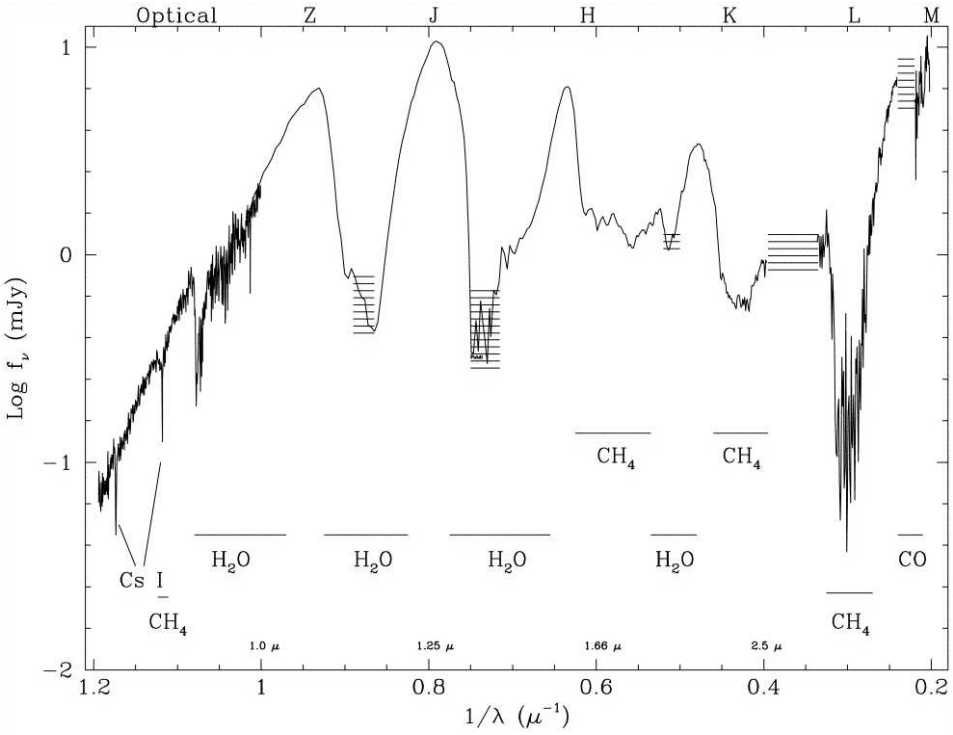

Figure 7.5: Spectrum of Gl 229B from 0.84 to 5 μm. H_2O and other major opacity sources are indicated. The horizontal bars indicate regions where telluric absorption prevents useful data collection. The various wavelength bands are indicated at the top of the figure. Reproduced from Oppenheimer et al. (1998).

doublet consisting of an early T dwarf (ϵ Indi Ba) and a late T dwarf (ϵ Indi Bb), separated by 0.6 arcsecs (Figure 7.6).

BT1 was used to determine the origin of certain features in the spectrum of ϵ Indi Ba. The spectra in Figure 7.7 were obtained using the 8.1 m Gemini South telescope and the NOAO Phoenix spectrometer (Smith et al., 2003). A synthetic spectrum was generated at 1 500 K, and convolved to match the resolution of the observed spectrum (R = 50 000). Figure 7.8, here shown in emission, summarizes these results.

Smith et al. had been able to assign two features in Figure 7.7, but not the feature just longward of 1.554 μm. The un-labelled feature was identified as a blend of six water lines, with no individual line contributing more than 25% of the intensity. The strongest four of these were the J9←J8, J10←J9, J13←J12 and J15←J14 transitions. We were also able to demonstrate that the feature at ∼1.555 μm, which Smith et al. identified as: (2 0 0)[13 10 3]←(0 0 0)[14 11 4] (our notation) is also blended with five other medium intensity lines, and that the strongest line (the one identified

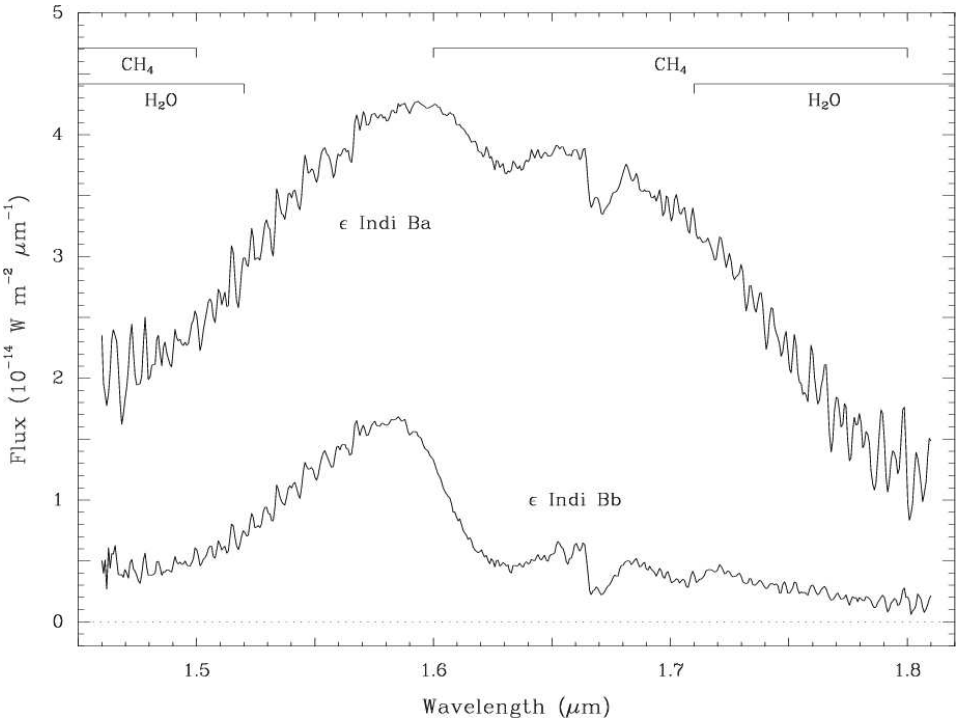

Figure 7.6: Spectrum of the close optical doublet: ϵ Indi Ba, ϵ Indi Bb in the wavelength range 1.45–1.80 μm at a resolution of ∼1 000. Reproduced from McCaughrean et al. (2004).

by Smith et al.) only accounts for approximately half of the total intensity of the absorption feature. The analysis of the water features in the spectrum of ϵ Indi Ba was the first practical application of our line list. It was conducted using an incomplete version of BT1 at a time when only a limited number of levels in the list were fully labelled. Consequently, at the time that the investigation was carried out, it was not possible to assign some of the individual weaker transitions in these blends.

It will also be seen by comparing Figure 7.7 and Figure 7.8 that certain unmarked features in the observed spectrum correspond to features in the BT1 synthetic spectrum. The positions of the features do not correspond exactly, and from the relative positions of the three water features in the observed and synthetic, rest-frame, spectra, indicates a blue shift of 60±20 km s^{-1}. Finally, by generating synthetic BT1 spectra at various temperatures, the temperature of ϵ Indi Ba is determined to be 1 500 K ±100 K. The sensitivity of the shape of the synthetic spectrum to temperature can be seen from Figure 7.8, which also contains a plot produced at 1 000 K. The intensities of the observed absorption features which are reproduced well in the 1 500 K BT1 synthetic spectrum are very much reduced, (particularly at shorter

wavelengths) in the 1 000 K synthetic spectrum.

Recntly we have used the BT2 line list to generate a synthetic spectrum of this wavelength region. This demonstrates that the seven strongest features in Figure 7.7 are due to water (Tennyson et al., 2006b). In total we have identified what we believe to be the 19 strongest water lines contributing to these features, and we have fully assigned 18 of these (see Table 7.1). Our derived value for the blue shift based on

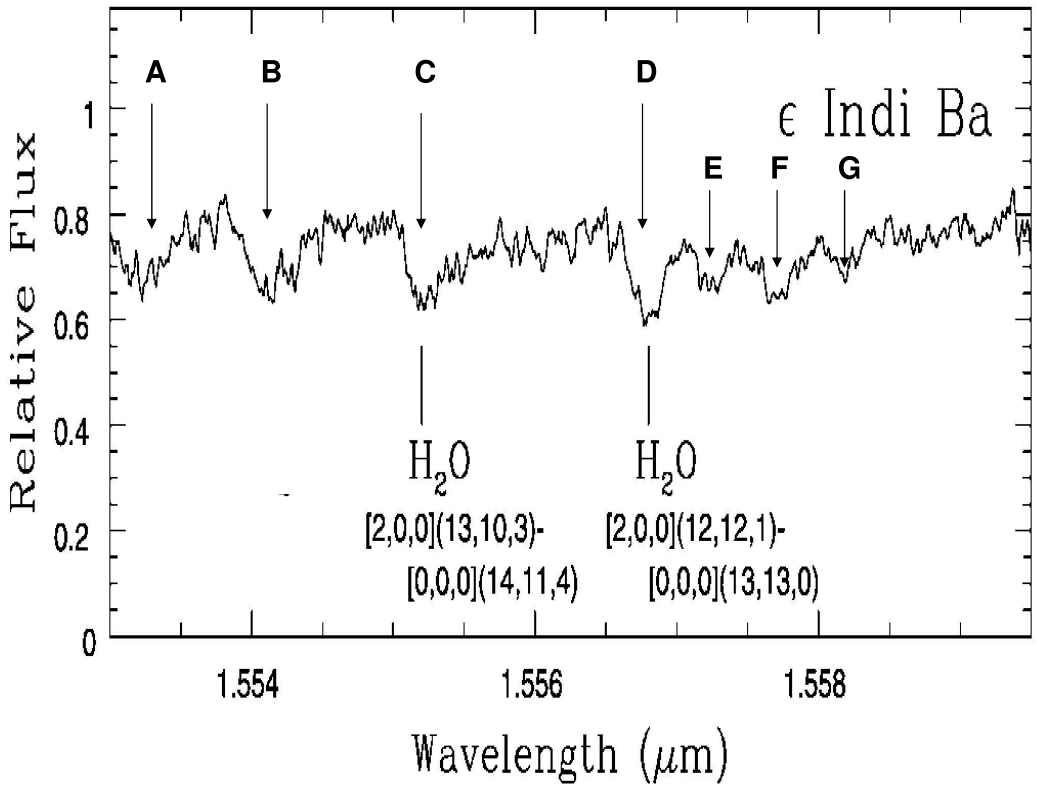

Figure 7.7: Spectra of ϵ Indi Ba in the region 1.553 to 1.559 μm (reproduced from Smith et al., (2003)). A BT1 synthetic spectrum (see Figure 7.8) identified feature B at 1.5541 μm as being a blend of six water lines, with no line accounting for more than 25% of the total intensity. BT1 also confirmed the assignment of the transitions indicated against features C and D. Recent work using BT2 (see Table 7.1) has identified all of the features A-G as being due to water .

7.4 Atmospheres of cool stars and dwarfs

Because of their cool temperatures and relatively high photospheric pressures (ranging from 0.1 to 10 bar), the atmospheres of M dwarfs and brown dwarfs are rich in

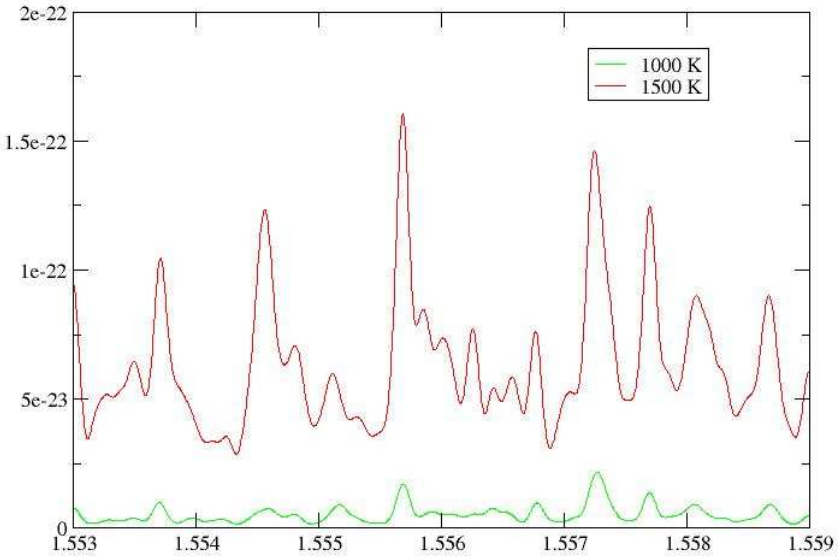

Figure 7.8: BT1 synthetic spectrum in the region 1.553 to 1.559 μm. used to identify water features in Figure 7.7.

molecules. These absorb and emit radiation in the near-IR, a region of the spectrum that corresponds to the peak energy fluxes of brown dwarfs, rendering them extremely important sources of opacity for these objects: the Planck function peaks at 1.2 μm at 2 500 K, at 1.9 μm at 1 500K and at 3.6 μm at 800K.

Any treatment of their atmospheres must include chemical equilibrium abundances for a large number of atomic and molecular species and also deal with grain and condensate formation and atmospheric turbulence.

Accurate modelling of cool atmospheres must take into account the position, intensity and width of possibly as many as a billion spectral lines due to the many species present. Relative abundances are temperature-dependent, but the major molecular species contributing to the opacity will always include a selection of the following: H_2O, CO, CH_4, NH_3, H_2S and metallic hydrides (Tsuji, 1995; Burgasser, 2002).

One of the problems facing the modellers of the atmospheres of cool stars and brown dwarfs is the disagreement between observation and model. Nevertheless, considerable progress has been made in recent years in such areas as: convection,

Table 7.1: BT2 identification of the main lines in the seven principal absorpion features in the spectrum of ϵ Indi Ba (Smith V.V. et al., 2003, ApJ, 582, L105). x indicates that the quantum number is not known. The wavelengths given here are in the rest frame. The observed data are blue shifted by approx. 80 km s^{-1}).

Upper level $(\nu_1\nu_2\nu_2)[JK_aK_c]$	Lower level $(\nu_1\nu_2\nu_2)[JK_aK_c]$	λ μm	$I_{line}\times10^{-24}$ cm mol^{-1}	Previously Identified	Feature (observed)
(2 0 1)[20 0 20]	(1 0 0)[21 0 21]	1.55370	11.51	No	A
(0 0 2)[12 6 7]	(0 0 0)[13 9 4]	1.55370	6.23	No	A
(3 0 1)[6 2 4]	(2 0 0)[7 2 5]	1.55373	4.45	No	A
(1 2 0)[13 4 9]	(0 0 0)[14 5 10]	1.55375	11.44	No	A
(2 0 1)[18 3 16]	(1 0 0)[19 2 17]	1.55375	9.00	No	A
[1](0 2 2)[19 1 18]	(1 0 0)[20 2 19]	1.55455	9.34	No	B
(0 2 1)[20 1 19]	(0 0 0)[21 1 20]	1.55455	10.66	No	B
(0 4 1)[13 1 12]	(0 2 0)[14 1 13]	1.55456	5.42	No	B
(3 0 0)[14 3 12]	(0 0 1)[15 3 13]	1.55457	13.51	No	B
[2](2 1 0)[12 8 5]	(0 1 0)[13 9 4]	1.55461	9.14	No	B
(2 0 0)[13 10 4]	(0 0 0)[14 11 3]	1.55570	12.69	No	C
(2 0 0)[13 10 3]	(0 0 0)[14 11 4]	1.55570	38.07	Yes	C
(2 0 0)[12 12 0]	(0 0 0)[13 13 1]	1.55723	11.85	No	D
(2 0 0)[12 12 1]	(0 0 0)[13 13 0]	1.55723	35.55	Yes	D
(0 4 1)[12 0 12]	(0 2 0)[13 0 13]	1.55771	26.83	No	E
(1 2 0)[15 8 7]	(0 0 0)[16 9 8]	1.55809	17.33	No	F
(x x x)[23 x x]	(0 0 0)[24 8 17]	1.55813	5.68	No	F
(1 2 0)[13 9 4]	(0 0 0)[14 10 5]	1.55864	12.33	No	G
(1 2 0)[13 9 5]	(0 0 0)[14 10 4]	1.55864	4.11	No	G

[1] or (2 0 1)[19 2 18] [2] or (1 3 0)[12 8 5]

molecular abundances, non-LTE effects and dust (Hauschildt et al., 1999; Tsuji, 2002; Alexander et al., 2003). At the same time, there have been advances in computing the opacity effects of the various species that are included in the models.

At the temperature of late M dwarfs (2 500 K), water is by far the most important source of atmospheric opacity, typically accounting for over 60% of all opacity in the infra-red. It is also an extremely important contributor to the opacity of L and T dwarfs (otherwise called 'methane dwarfs').

In M dwarfs and L dwarfs, the H_2O bands centred on 1.15, 1.4 and 1.9 μm separate the energy distribution of brown dwarfs into distinct peaks in the J, H and K bands and this structure is very apparent for type L6.5 V and later. CH_4 bands characterise T dwarf spectra and these have the effect of further confining the emitted flux into narrow peaks centred at 1.08, 1.27 1.59 and 2.07 μm (Burgasser, 2002). This structure is evident in the spectrum of Gl 228B, Figure 7.5.

M dwarfs and L dwarfs have strong CO absorption in the K band at 2.3 μm, which is not present in T dwarfs (see Figure 7.9). This figure also shows clearly that the methane absorption feature at around 2.2 μm seen in the spectrum of Gl 229B in Figure 7.9 is not present in the L dwarf spectra. Indeed, the ratio between the intensities of the various peaks in emitted flux between the H_2O, CH_4 and CO absorption bands is a way of classifying the spectral sub-types of brown dwarfs (Burgasser, 2002).

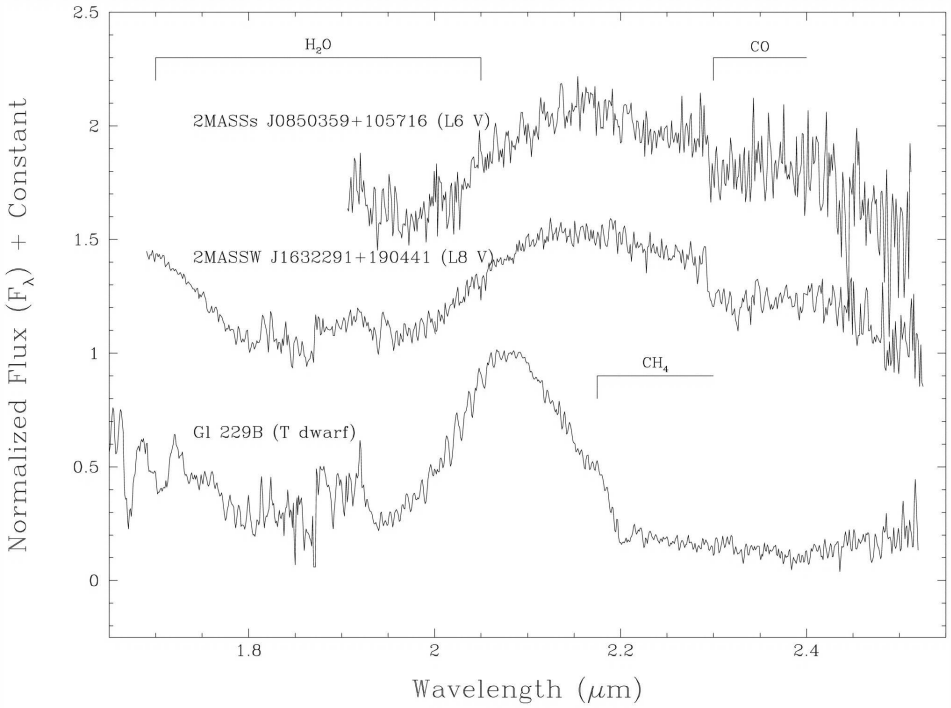

Figure 7.9: Spectra of two late L dwarfs and T dwarf Gl 229B, showing the L dwarfs have strong CO featured, but no CH_4 absorption, whilst this situation is reversed in the T dwarf spectrum. All three spectra have strong water absorption features. The vertical positions have been adjusted by random amounts to simplify presentation. Reproduced from Kirkpatrick et al. (1999).

Despite the attention that this area of research is now attracting, modelling the atmospheres of brown dwarfs is being constrained by: an inaccurate and incomplete treatment of opacity, lack of an accurate equation of state (that is to say, a lack

of knowledge of the relations between the density and temperature of the material and the pressure and internal energy of the brown dwarf) and also the absence of accurate Einstein A coefficients for important molecular species.

Without detailed molecular line lists, models of the spectra of brown dwarf atmospheres have frequently had to make broad-brush approximations regarding molecular opacities that have the effect of smearing out the rotational fine structure. However, even though they are crude approximations, these methods do have the advantage of being computationally less-demanding than ones based on full line lists for the species.

A more accurate method of computing molecular and atomic opacities in model atmospheres is achieved by an Opacity Sampling treatment of transition lists on a prescribed fine grid of wavelengths. Nevertheless, even with great improvements in the treatment of opacities for some species (e.g., CO), the available opacities for important absorbers such as CH_4 and NH_3 (see Section 10.3) place very serious limitations on the accuracy of this method. The ability to now include the BT2 H_2O line list should allow much more accurate modelling for water at least.

Another issue that needs to be addressed is line broadening. This is important in a number of astronomical situations, including modelling the atmospheres of cool stars and brown dwarfs. In addition to thermal (Doppler) broadening, line broadening is caused by pressure effects due to van der Waals forces arising from the interaction between two different neutral particles.

Lines in the spectra of cool stars and brown dwarfs are broadened by collisions of atoms and molecules with molecular hydrogen in their atmospheres. The strongest lines are the ones most affected. This pressure broadening is not able to be adequately described theoretically, and attention has focussed on semi-empirical methods involving fitting to experimental data (see for example: Bykov et al., 2004; Zeninari et al., 2004, Lavrentieva, 2005). It is possible that research on line broadening currently being carried out by N.N. Lavrentieva (Institute of Atmospheric Optics, Russian Academy of Science, Tomsk) using the BT2 line list may result in pressure broadening parameters being included in the line list at a future time (see Section 10.4).

7.4.1 The models

The construction of a stellar atmospheric model is an iterative process. The starting point is a basic model that involves physics in the form of convective and radiative transfer models, it makes assumptions about parameters such as surface gravity, convection, the role of dust and non-LTE effects. Next an assumption must be

made about atomic and molecular abundances. These are frequently assumed to be solar, but even this leaves room for debate as it has recently been suggested that the acknowledged solar abundances may be significantly in error (Asplund et al., 2005). Finally, the spectral line list of each species is required, and the lack of experimental data means that for most molecules the lists are mainly of a synthetic nature. Using all of these input parameters, a model atmosphere is produced, and this in turn is used to generate a synthetic spectrum of the star which is compared with observation. The input parameters are then modified in order to obtain a better fit with observation. Some parameters, such as the line lists and the ionization and dissociation energies, are an integral part of the models, whilst others such as temperature, surface gravity and metallicity are specific to the star.

If, by altering its object-specific parameters within accepted limits, whilst leaving the basic code unchanged, a model is able to generate synthetic spectra that are good fits with observed spectra for a range of stellar objects, the model is demonstrated to be satisfactory. It can then be used to determine the effective temperature, surface gravity and metallicity of stellar objects, and from these data the mass and age of the object can frequently be inferred.

Different models achieve various degrees of success in replicating observed spectra. Moreover, because the physical parameters of stellar and sub-stellar objects cover such a wide range, and the roles of convection and radiation vary with mass (for example stars with a mass of less than 0.4 $M_{\odot}$ are fully convective and radiative transfer only applies in the optically thin outer regions of the atmosphere), and the contribution to the opacity of stellar atmospheres of various species is extremely temperature dependent, it is possible for a model to work well for one type of object but not with another. Overall, considerable advances have been made in recent years due to the advent of better algorithms and faster computers. Today's models are able to include: different treatments of geometries (plane-parallel or spherical), line blanketing, micro-turbulence and non-LTE effects, that were computationally impossible only a few years ago. At the same time, advances in observational astronomy have expanded the database of high resolution spectra, and nowhere has this been more so than in the field of very low mass stars, and brown dwarfs.

It is with these classes of cool objects that we are primarily concerned, as their temperatures are low enough to allow the existence of gaseous water, and consequently when discussing stellar atmospheric models, other applications are ignored.

However, there are still major shortcomings between the observed and modelled spectra of cool stars and brown dwarfs. Baraffe et al. (1998), indicate that the difficulties are likely to lie with a still incomplete description of their atmospheres

rather than with structural and energy transport problems with the models. This indicates that problems still exist with the line lists for some important species.

Cooler temperatures give rise to additional problems in modelling the atmospheres of brown dwarfs, in the form of condensates (clouds). At temperatures below ∼2 000 K, dust forms in the atmospheres of brown dwarfs. As temperatures reduce, corundum, titanates, silicates and iron compounds are able to condense whilst at the extremely low temperatures of late T dwarfs, Y dwarfs and extrasolar giant planets H_2O and NH_3 are capable of condensing. The formation of dust and clouds greatly complicates the modelling. For example, clouds have the effect of lowering the emitted flux in the near-infrared, whilst tending to equalise the J, H and K band fluxes (Marley, 2001). Models attempting to deal with condensation need to take into account three separate processes: condensation, sedimentation and coagulation (Allard et al., 2003).

PHOENIX is the most important and frequently used code for modelling the atmospheres of cool stars and brown dwarfs, and this is discussed below. However, there are also other models, some of which are particularly successful in replicating the spectra of other types of astrophysical object. Marley et al. (1996) modified a model that had originally been constructed to study the atmospheres of Jovian planets, to reproduce the spectrum of the first observed T dwarf, Gliese 229B. The ATLAS model (Kurucz, 1970) is primarily used for objects having a temperature greater than 5 000 K. MARCS (Gustafsson and Frommhold, 2000) is mainly applied to giant stars, and SAM (Pavlenko, 2003), which is a modified version of ATLAS and has been used to model the nova-like object V4334 Sgr (Pavlenko and Geballe, 2002). Pavlenko and co-workers also used BT2 in SAM12 to model the ejected envelope surrounding V838 Mon (Pavlenko et al. 2006).

7.4.2 The PHOENIX code

PHOENIX is a versatile stellar atmosphere code that can be used to compute the atmospheres of a wide range of objects from Earth-like planets and T dwarfs at the one extreme and O-B stars, cataclysmic variables and supernovae at the other. A complete and accuate water line list is essential for PHOENIX to be able to model astrophysical situations where water molecules make a significant contribution to atmospheric opacity. The BT2 line list is now included in the standard PHOENIX database, where it is playing an important role in modelling the atmospheres of: exoplanets, brown dwarfs, M dwarfs and late-type giants.

The details of the PHOENIX code are beyond the scope of this Ph.D. thesis, but a brief introduction to the code will be useful in helping to put the inclusion of

BT2 in PHOENIX in context.

The PHOENIX code has undergone continuing development and improvement since its inception. Its basic construction and mode of application are detailed in Hauschildt et al. (1994) and Baron et al. (1994), and Allard and Hauschildt (1995) provides a useful introduction. Following the inclusion of BT2, PHOENIX now contains about 800 million lines, with BT2 making up more than 60% of this total. Because of demands on computing time, it will normally be the case that a typical model run will include no more than half of this number of lines.

Table 3 of Ferguson et al. (2005), gives a summary of the available line data for major molecules in PHOENIX (Table 4 gives the same information for minor molecules). This list, which predates the publication of BT2, shows that the next most important species, in terms of number of lines, is TiO. Models of cool stars and brown dwarfs are particularly sensitive to the accuracy of the TiO line list and this has been a long-standing problem in the modelling of M dwarfs. Allard et al. (2000), demonstrate that the AMES-TiO list (Schwenke, 1998) containing 174 million TiO lines is an improvement on the earlier SCAN-TiO list Jørgensen, (1994a), but points to the continuing problems of modelling of M dwarfs using the AMES-H_2O list (Partridge and Schwenke, 1997). However, by testing the effect of including BT2 instead of AMES-H_2O in PHOENIX, Barber et al. (2006d) demonstrates , that contrary to what was previously thought, H_2O is unlikely to be a major cause of the residual errors in M dwarf models.

7.4.3 Other models

In addition to the above applications of BT2, the line list was used by Pavlenko et al. (2006) to compute the theoretical spectral energy distribution (SED) of an L supergiant, for the purpose of comparison with the observed spectrum of V838 in the 0.45–1.0 μm range (see Section 5.3). They employed NextGen model atmospheres (Hauschildt et al. 1999) with T_{eff}=2 000–2 200 K. Their list of ∼100 species was assembled from a variety of sources, with the H_2O line data being taken from BT2. With the exception of the 0.75 μm region, they obtained a good fit with the spectrum of V838 Mon using a model atmosphere temperature of T_{eff}=2 000 K

Jones et al. (2005a) compare observed CO 2-0 bands in the 2.297-2.310 μm region of several M and L dwarfs with opacity calculations using the PS and BT2 line lists. They conclude that for this particular wavelength range 'While the Partridge-Schwenke line list is a reasonable spectroscopic match [for the BT2 line list] at 2 000 K, by 4 000 K [which is above the temperature of these objects] it is missing around 25% of the water vapour opacity'.

Chapter 8

Laboratory spectra and water in sunspots

The first high resolution oxy-acetylene torch spectra of water were recorded by J.-P. Maillard using a Fourier transform spectrometer. The data are reported in Flaud et al. (1976) and Camy-Peyret et al. (1977). By the standards of modern Fourier transform spectroscopy, an oxy-acetylene torch produces spectra of only modest resolution as the lines are pressure-broadened by 0.05–0.1 cm^{-1} due to the ambient atmospheric pressure. In addition, Doppler-broadening at 3 000 K contributes a further 0.09 cm^{-1} to the line width at a frequency of 10 000 cm^{-1}. This means that many transitions appear as blends, which complicates the identification process.

The BT1 and BT2 line lists (which have identical energy levels) have been used by a number of researchers to analyse laboratory torch spectra at various wavelengths, thereby adding to the existing database of experimentally-known energy levels and transitions for water. Laboratory flame spectra of water are of astronomical importance as the temperatures achieved in these flames (3 000– 3 200 K) are similar to those of mid-to-late M type stars and large sunspots.

We describe below some of the recent analyses of laboratory flame spectra, that have used the BT1/BT2 line list.

Coheur et al. (2005) obtained laboratory oxy-acetylene torch spectra of water at 3 000 K in the range 0.77–20 μm using a Bruker IFS 120 M Fourier transform spectrometer. They analysed spectra in the 5 to 20 μm range. Using BT1 they determined ~600 energy levels that had previously not been identified experimentally. These were used as the basis for assigning observed transitions, and in total they assigned 8 500 of the 10 100 lines that they observed in this spectral region. Most of the states that were determined by Coheur et al. were either high J states, having

low bending excitation, or else lower J states with higher bending excitation. These states had defied earlier analysis because the previous line lists used in earlier work, were unable to accurately predict the energies of states above 15 000 cm^{-1} or to treat accurately the high bending mode states, even those below 15 000 cm^{-1}.

In the case of transitions involving high J and low K_a they note that unlike low J states, where the agreement between the BT1 line list and observation is generally within 0.1 cm^{-1}, disagreement can be as great as 0.8 cm^{-1}. Nevertheless, they comment that since for a given vibrational and K_a state the difference between the BT1 list and experiment increases smoothly with J, they were able to use BT1 to predict the positions of higher J levels with an accuracy of 0.02 cm^{-1}. This is considerably less than the experimentally- determined line widths.

The actual method of assigning transitions is not relevant to this Ph.D. thesis. However, for completeness, it is noted that the authors used three different methods depending on the values J, K_a and ν_3, and that for transitions involving high J, low K_a levels, the method of branches (Polyansky et al. 1997b and 1997c) was used.

After completing their work on the torch spectra, Coheur et al. (2005) re-analysed the sunspot absorption spectra of Wallace & Livingston (1992) and were able to assign several hundred previously unidentified water lines. As in the case of the torch spectra, these assignments were only possible through their use of the BT1 line list.

In a follow-up paper, Zobov et al. (2006) analysed the 2.00–4.75 μm region of the Coheur et al. (2005) torch spectra. They used BT2 to determine approximately 800 experimentally previously unidentified ro-vibrational energy levels for water. These cover 15 vibrational states with rotations up to $J = 32$. Once the energy levels had been identified it was a trivial exercise to compute line positions. However, as a simple check, the theoretical line intensities at 3 000 K (computed using the BT2 Einstein A coefficients) were compared with the experimentally observed intensities to ensure that the intensity of each assigned transition was consistent with observation. It was possible to assign 12 431 lines in this fashion, leaving only 2 965 lines unassigned in this wavelength range. The greatest number of new energy levels belong to the (002) state; transitions involving this level appear to be have been under-represented in the analysis of previous hot water spectra. The energy levels that they identify include many with high J values (up to J=36) and they claim an accuracy of 0.02 cm^{-1} for these energies (derived from BT2) which is similar to the error in determining the line positions in the laboratory emission spectra.

Zobov et al. used two different methods in assigning new lines. For transitions involving states with high J but low K_a, the method of branches was used to follow

a series of transitions with quantum numbers which simply differ by one in J. This method was used for 18 low-lying vibrational levels and yielded about 300 new energy levels.

For transitions with J in the range of 15 – 25 and intermediate values of K_a, the error (obs. – calc.) obtained using the BT2 predictions varies smoothly with K_a and K_c. This means that the positions of experimentally-determined energy levels could be predicted with sufficient accuracy for new assignments to be made. This method was used for 15 vibrational states associated with stretching transitions (Δv_1 or $\Delta v_3 = 1$) to yield about 500 new energy levels.

After using BT2 to identify lines in the torch spectra, Zobov et al. also examined the sunspot absorption spectra of Wallace and Livingston (1992), in a similar way to Coheur et al. and were able to assign 581 previously unidentified water lines in the L band and 67 in the N band. The L band sunspot spectrum contains a total of 2 723 transitions compared to 4 593 in the torch emission spectrum, and by using their torch assignments, Zobov et al. were able to identify 1 579 of these as water lines (up from 998 previously), with a further 199 being known to be OH lines and 10 due to HCl. In contrast, the N band sunspot spectrum is very dense and only 67 previously unknown water lines were assigned.

Zobov et al.'s data has been posted on:

http://mas.lib.ohio-state.edu/jmsa_hp.htm

Figure 8.1 is reproduced from Wallace and Livingston (1992). The wavelength region selected $\sim$11.45 μm is longward of the regions investigated by Coheur et al., or Zobov et al., but illustrates the congested nature of the sunspot spectrum. Some of the stronger transitions are assigned, but many of the weaker ones in this region have still to be identified. All of the transitions that have been identified in this region are pure rotational transitions. We would expect that many of the unassigned features involve changes in both the rotational and vibrational states and are consequently less easily identified. Polyansky et al. (1997c), indicate the manner in which three observed transitions between a total of four ro-vibrational states can be used to predict the frequency of a fourth, rotational difference transition, between two of these four states. An observation of this fourth transition is therefore confirmation of the assignments of all four transitions

Tolchenov et al. (2005) analysed long-pathlength room temperature spectra. They used three separate line lists in their work. However, only the BT2 list was found to be reliable over all transition frequencies and in the case of lines having frequencies above 16 000 cm^{-1} it is the only one used. In addition, Tolchenov et al. encountered difficulties with the labelling adopted in previous studies, finding, for

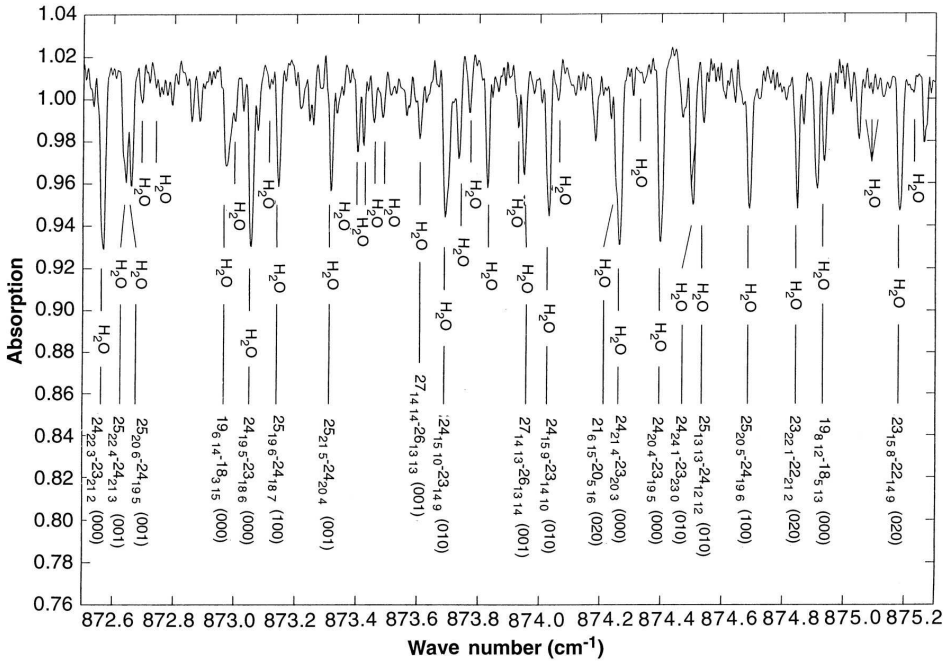

Figure 8.1: Extract from the sunspot spectrum of Wallace and Livingston (1992), with the addition of some pure rotational line assignments. The rotational angular momentum quantum numbers are given as: $J_{K_a K_c}$(upper)–$J_{K_a K_c}$(lower) and the vibrational quantum numbers (ν_1 ν_2 ν_3) are in brackets.

example, that in some cases different states have been labelled with the same quantum numbers. They therefore undertook a systematic re-labelling exercise using the BT2 energies. These labels are incorporated into the BT2 list for states with $J \leq 9$ (see Section 3.3).

Dupré et al. (2005) found BT2 similarly reliable for predictions of long-pathlength room temperature spectra in the near ultra-violet. They observed 62 R-branch transitions in the 8ν polyad and were able to determine 36 energy levels, previously unknown experimentally.

Chapter 9

Summary

The Barber-Tennyson synthetic water line list (BT2) gives the energies of 221 097 ro-vibrationalstates with cut-offs of J=50 and E=30 000 cm^{-1}. 25 870 of the lower energy levels have been labelled with a full set of three rotational and three vibrational quantum numbers. BT2 lists 505 806 202 transitions. It has been extensively tested against experimental observations and also compared with other lists. It has been shown to be the most complete and accurate water line list in existence.

A range of different applications is described in which the BT1 or BT2 line lists have been used to identify spectral features, determine physical parameters such as temperature and column density, and model cool stellar atmospheres and the chemical evolution of a circumstellar envelope.

These applications have provided an extremely important demonstration of both the accuracy and versatility of BT2 and it is hoped that the astronomical community at large will adopt it as the standard H_2O line list. If so, our labours will have been fully rewarded.

The BT2 line list and the program spectra-BT2.f90, which is capable of generating water spectra from our database using a wide range of input parameters, are freely available in electronic form via:
http://www.tampa.phys.ucl.ac.uk/ftp/astrodata/water/BT2
and also via: *ftp://cdsarc.u-strasbg.fr/cats/VI/119*

Chapter 10

Future Work

It will be seen from the foregoing that the BT2 line list is finding application in many astronomical situations. In most cases we have not actively sought these projects - rather, the reputation of BT2 has brought the interested parties to us. Moreover, we anticipate that there will continue to be requests for us to collaborate on a range of projects.

10.1 Opacity in brown dwarfs

Molecules are the principal source of opacity in cool stellar atmospheres. Nevertheless, it is only 20 years since one of the leaders in the field was able to state that, in contrast to atomic spectroscopy, which had its origins in the nineteenth century, molecular spectroscopy was playing a very minor role in our understanding of stellar objects (Tsuji, 1986).

This is no longer true. Improved knowledge of molecular spectra is leading to a better understanding of the nature of a wide range of astrophysical objects, particularly cool stars and brown dwarfs, and it is this latter area with which we are here concerned.

Molecular abundances in stellar atmospheres can be well predicted by classical thermo-chemistry and it is known that there is a major change in the chemical equilibrium at the stellar/brown dwarf boundary (Tsuji, 1995). Specifically, CO, which because of its great stability is important in controlling the chemical equilibrium, is no longer the major carbon species at temperatures below $\sim$1 000 K (the precise temperature depends on pressure), and this role is taken over by CH_4, even in the oxygen rich case. Similarly, N_2 which is the major form of nitrogen in stellar atmospheres at higher temperatures is replaced by NH_3 in late T and Y dwarfs, and

other species such as SiH_4, PH_3, and H_2S also become abundant. However, spectroscopic data for these species is meagre and is the main constraint in understanding late brown dwarfs. It is against this background that we now discuss the specific requirement for further line lists.

10.2 An Ammonia line list

Despite the interest that BT2 has generated, we are being pro-active in identifying other molecules where there is a requirement for high accuracy line lists and where we might profitably apply the expertise that we have developed in computing BT2. Specifically, we have been awarded a Leverhulme Trust Research Project Grant to produce an *ab initio* line list for the ammonia molecule. These data are required, *inter alia*, by researchers who are seeking to discover, and understand the nature of, Y dwarfs. These objects are ultra-cool brown dwarfs with a temperature between late T dwarfs and planetary gas giants (in the region of 600–800K). It is predicted that their atmospheres will consist principally of clouds of ammonia and methane, and that these two molecules will therefore dominate their spectra However, neither of these two molecules has a line list that is complete or accurate enough to permit atmospheric modelling.

We have decided to compute an ammonia line list because we believe the task, which we estimate to be in the region of 20 times more demanding in terms of computational requirements than the H_2O project (see Section 10.3.2), and currently lies outside UCL's computing capabilities, will be able to be performed using the next generation of computer that is due to be installed in the Department of Physics and Astronomy next year.

Below, we outline the reasons why, and the method by which, we are now embarking on the very substantial undertaking of generating an ammonia line list. We regard this as being suitable material for inclusion in this Ph.D. thesis as it is part of the author's wider remit of producing high accuracy synthetic molecular opacities with astronomical applications.

10.3 Requirement for an NH_3 opacity

Ammonia is an important molecule in astronomy. It is observed in such varied environments as: the interstellar medium (Ho and Townes, 1983) comets, planetary atmospheres, cold dense molecular clouds (Larsson et al., 2003; Liseau et al., 2003), circumstellar envelopes (Betz et al., 1979), mass outflows from star forming regions

(Ho et al., 1983) and the atmospheres of brown dwarfs, later than T5 (Burrows et al., 2003). It is also an important constituent of the atmospheres of gas giants.

Astrophysicists have predicted the existence of a new class of object, a brown dwarf cooler than T dwarfs. Models suggest that these objects, which have been termed 'Y dwarfs', will have temperatures below 800 K (the precise figure will be determined once there is a proper opacity function) and masses less than 25 times that of Jupiter. Their spectra will be dominated by methane, ammonia and water bands (Burrows et al., 2003).

To-date, no Y dwarfs have been identified. However, recent observations have produced many candidates for the new class of brown dwarf, based on measurements of mass (Lodieu et al., 2005; Lucas et al., 2005) but so far, follow-up IR spectroscopic observations undertaken by M. Tamura on Subaru and by H. R. A. Jones on Gemini South, have failed to confirm any of these candidates as being Y dwarfs.

Once spectra of Y dwarfs have been obtained, it will be important to analyse them in order to understand the nature of their atmospheres (which is fundamental to understanding the development of these objects). This will involve the construction of model atmospheres to try and replicate observations. However, the sparsity of data on the spectrum of hot ammonia will be a major constraint on such work.

We anticipate that an ammonia line list will be of value in a wide variety of other astronomical research including, *inter alia*, comet comas, the atmospheres of solar and extra-solar planets and possibly in the chemistry of the ISM.

10.3.1 The nature of the spectrum of ammonia

Ammonia is a 'floppy', pyramidal, symmetric top molecule. Its rotational energy is a function of the total angular momentum, J, of the molecule and its projection, K, onto the axis of symmetry. In the absence of vibrational motion perpendicular to the axis of symmetry, the electric dipole moment is in the direction of this axis and in this case the dipole selection rules are ΔJ=0,$\pm$1 and ΔK=0. However, vibrational motions produce dipole moments perpendicular to the axis of symmetry and these give rise to Δk=$\pm$3 transitions, where K=$\mid k \mid$. States where J > K decay rapidly via pure rotational transitions in the far infrared, whilst the J=K states decay via the slower Δk=$\pm$3 transitions.

The floppy, pyramidal, structure of the molecule makes it possible for the nitrogen nucleus to tunnel quantum mechanically through the plane of H atoms via a high amplitude stretch parallel to the axis of symmetry. That is to say, there are two distinct C_{3v} minima connected by a D_{3h} transition state. The barrier to this tunnelling, or flipping, of the molecule between one configuration and its mirror

image (the so-called ν_2 umbrella mode) is approximately 1 800 cm^{-1}, which is low enough for inversion to occur easily. Consequently, all rotational states, with the exception of those for which K = 0, are split into inversion doublets. The quantum tunnelling poses particular problems in the generation of synthetic ro-vibrational energy levels.

It should be noted that, as is the case with H_2O, the first stable electronically excited state for ammonia lies above the ground state dissociation limit. This means that for astrophysical purposes ammonia is in its electronic ground state and its spectrum is determined by rotation-vibration transitions.

10.3.2 Computation of an ammonia line list

Because it has four atoms, ammonia has nine degrees of internal freedom, three more than the triatomic molecule, H_2O. To a good approximation, each additional degree of vibrational freedom increases the demands on computational time by an order of magnitude, hence it would seem logical to assume that the computation of an ammonia line list would be 1 000 more demanding in terms of computer time than was the case for H_2O. Moreover, as in excess of 50 000 mainframe processor hours were used in calculating BT2, it would appear at first sight that the ammonia problem lies beyond current computing capabilities. However, the scope of the problem is reduced by the fact that astronomical applications are limited to temperatures below 1 500 K and wavelengths longer than 1 μm. In order for the ammonia line list to be accurate at these limits of temperature and wavelength, we calculate that the maximum ro-vibration energy that we will need to compute is 17 000 cm^{-1}, compared to 30 000 cm^{-1} for H_2O, and that the maximum required J will be 35 (in the case of BT2, J_{max} was 50). We estimate that the adoption of these less-demanding limits, will reduce the necessary computing time by about 80%. Also, the high degree of symmetry in the ammonia molecule should enable us to make additional computational savings. Finally, although we plan to use the best available potential energy surface and computational programs, we do not expect to achieve an accuracy of better than 0.5 cm^{-1} for most of the transitions (compares 0.1 cm^{-1} for BT2). This will enable us to adopt less rigorous convergence criteria for our computations, which will in turn result in time savings.

Taking all of these factors into account, we estimate that we will need to compute in the region of 1 million energy levels and 10 billion transitions, compared to 221 000 levels and 505 million transitions for our H_2O line list. Consequently we expect the task to be approximately 20 times more demanding in terms of computer processing and storage requirements than was the BT2 line list, which is the most demanding

tri-atomic molecular computation performed to-date.

Some eigenvalue solutions of the Schrödinger equation for the nuclear motion of NH_3 have been generated and tested against experiment (see for example Lin et al., 2002). In particular cases, wavefunctions generated in the nuclear motion part of the problem (see below) have subsequently been employed in calculating the intensity of some of the lines in a small number of ro-vibrational bands (see for example Yurchenko et al., 2005a). However, in every case the work has been performed within very constrained parameters. The energy levels computed are numbered in hundreds and the transitions (lines) generated, at the most, in thousands. No attempt has been made to produce a full systematic line list capable of generating synthetic spectra that are suitable for stellar atmospheric modelling. However, we believe we are now in position to accept this challenge.

10.3.3 Prerequisites

In addition to having adequate computing facilities, there are five key elements in generating any synthetic line list. These are:

- An accurate potential energy surface.
- An accurate dipole moment surface.
- A model to solve the Schrödinger equation for the nuclear motion.
- A model to calculate dipole transition moments and line intensities.
- Experimental data to test against.

We discuss each of these below.

10.3.4 Potential Energy Surface (PES)

We plan to use an existing PES. We have considered four surfaces. Each has as its starting point a high quality *ab initio* calculation. We consider first the Complete basics set (CBS*) surface produced by the Wuppertal group (Lin et al., 2002). The *ab initio* points were generated using coupled-cluster calculations. 14 400 points were evaluated and the accuracy of 1 480 of these points was enhanced by complete basis extrapolation techniques and by adding corrections for core-valence electron correlation (Schwenke and Partridge, 2000) and relativistic effects. The resulting 6-D PES was represented by analytic functions containing 75 parameters and involving Morse variables for the stretches, symmetry-adapted bending co-ordinates and a

specially designed inversion co-ordinate. Lin et al. computed vibrational energies for J = 0 up to 15 000 cm^{-1} using a variational model. They report that vibrational energy levels produced using CBS* in the 15 000 cm^{-1} region have an rms deviation of 4.4 cm^{-1} compared with experiment. We mention this surface because it has been published. However, CBS* has already been superseded (see below).

The second PES, CBS**-45760 is a yet-to-be published development by the Wuppertal group. Like CBS* it is computed using coupled-cluster theory with all single and double substitutions and a perturbative treatment of connected triple substitutions. However, it represents an improvement on their earlier surface. This PES and an associated DMS developed by this group, are discussed in Yurchenko et al. (2005a,b). In the second of these papers the authors report that the frequencies of the lowest 33, J = 0 vibrational levels have an rms deviation of 4.7 cm^{-1} compared to experiment. The authors also tested the accuracy of the rotation-vibration energies for the vibrational ground states and the ν_2, ν_4 and $2\nu_2$ vibrational states for J = 1 and 2 (44 states in all). The rms deviation with experiment is 1.2 cm^{-1}.

The third surface is that of the Helsinki group (Rajamäki et al., 2004). Like the two Wuppertal surfaces, this has been computed using coupled-cluster theory, but differs in that it uses explicitly correlated wavefunctions. The surface incorporates adjustments for relativistic and non-Born-Oppenheimer effects. The Helsinki group has aimed at achieving convergence at high energies and claims an accuracy of 1 cm^{-1} for the surface.

The fourth PES to be considered was produced by the Zurich group (Marquardt et al., 2005). Unlike the other three surfaces, after making analytical fits to the *ab initio* data, further adjustments are made to the parameter values to give better agreement with experiment. The quartic force field in this study is significantly different from that of the other potential surfaces mentioned, although the vibrational structures that the authors obtain from computations based on perturbation theory have similarities to those produced by the other groups that we have mentioned. Their methodology has enabled the Zurich group to give a 'qualitatively correct' description of the potential energy for large amplitude displacements. However, the group acknowledges shortcomings in its perturbational approach to solving the nuclear motion problem - energies differ from experiment by 2–30 cm^{-1}, and further work is underway.

Based on the currently published information, the Helsinki PES would appear to be capable of achieving the greatest accuracy. However, the second Wuppertal surface has the advantage that its output is compatable with the Wuppertal DMS (see next section). Our final decision will be determined by testing.

10.3.5 Dipole Moment Surface (DMS)

We outline below how wavefunction solutions to the Schrödinger equation are used in the calculation of the intensities of the allowed transitions. The computation requires knowledge of the dipole transition moments for the upper and lower states, which in turn requires a dipole moment surface (DMS). It has been shown for water (Lynas-Gray et al., 1995) that *ab initio* DMS give better results than ones fitted to experimental data. This, perhaps surprising, finding is a consequence of the difficulty of measuring absolute intensities accurately.

The best *ab initio* DMS for NH_3 is that of the Wuppertal group (Yurchenko et al., 2005a,b). This DMS was determined on the same six-dimensional grid used to generate the two Wuppertal PES discussed above. Yurchenko et al. used finite difference procedures at 14 400 points to obtain discrete *ab initio* values of the components of the electronic dipole moments. Parameterised analytic functions were fitted through these values to define the DMS. It is our intention to collaborate with the Wuppertal group with respect to the use of their DMS and possibly also in other areas of the computation.

10.3.6 Calculation of ro-vibration energies

Variational techniques represent the best approach to solving the nuclear motion problem (Handy et al., 1999) and they are examined in detail in Bačić and Light (1989).

Rotation-vibration motions of pyramidal molecules of the form XY_3 present a particular problem to theoretical spectroscopists related to the large amplitude inversion (see above). There are several available nuclear motion programs including ones developed by the Helsinki and Wuppertal groups, one by Handy and Carter specifically for the ammonia problem (Handy et al., 1999) and the more general WAVR4 suite (Kozin et al., 2004), which we believe is capable of being developed for application to the ammonia molecule. These models are discussed below.

The Wuppertal group (Lin et al., 2002), used a variational model employing an Eckart frame kinetic operator to calculate a number of vibrational band centres. The energy calculations are performed by variationally diagonalising a matrix representation of the inversion-vibrational Hamiltonian. The matrix representation is constructed in a basis set whose functions are obtained as products of: Morse oscillator functions for the local stretching mode, two-dimensional isotropic harmonic oscillator functions for the bending modes and inversion functions.

Handy et al. (1999) also used variational calculations. Vibrations were specified

in a D_{3h} point group. The kinetic energy integrals were evaluated separately for the radial, umbrella, angular and bending motions and their solutions to the nuclear motion within the PES were expressed as multiples of these integrals. The Handy et al. method is consequently not capable of being used with a flexible high accuracy potential energy function, which precludes its use in the ammonia opacity project.

We plan to test a modified version of WAVR4 against the Wuppertal nuclear motion and make our choice accordingly. We expect that the selected program will be accurate to better than 1 cm^{-1}.

10.3.7 Calculation of the transition intensities

The intensities of the allowed transitions between rotation-vibration states are determined by the dipole transition moments for these pairs of states. They are: $\langle \Psi_i | \overline{\mu} | \Psi_f \rangle$ where Ψ_i and Ψ_f are the wavefunctions of the two states and are solutions to the Schrödinger equation for rotation-vibrational motion obtained using the selected PES, and $\overline{\mu}$ is the electronic dipole moment vector and is dependent on the DMS selected.

In principle, two approaches are possible: an explicit calculation which has the merit of greater accuracy, but may not be computationally feasible, and a less-accurate, but tractable, approach based on band vibrational intensities and Höln-London factors. Our preferred route is the explicit calculation. However, if this proves to be computationally too demanding our alternative plan is to develop a Höln-London based methodology.

10.3.8 Experimental data to test against

We are in an excellent position to test the accuracy of the various PES, DMS and computational methodologies. We are fortunate in having access to unpublished laboratory emission spectra of hot ammonia produced by P. Bernath et al. at the University of Waterloo, Canada. The Bernath spectrum complements and extends the published sources of experimental data. It has remained unanalysed for some time, since none of the available theory is capable of modelling it. Consequently, the Bernath spectrum will provide a good test of our calculations in conditions close to those for which they are designed, that is to say, at temperatures in excess of 800 K. Our aim will be to eventually perform an analysis of this spectrum.

10.4 Line broadening

The uncertainties in interpreting (solar) spectra, that result from line broadening due to collisions between an absorbing atom and a hydrogen atom, were highlighted many years ago (Blackwell et al., 1972; Gurtovenko, 1980). Despite the passage of time, there is no satisfactory theory of line broadening although progress is being made in developing semi-empirical approaches (see Section7.4).

The line broadening resulting from collisions of molecules with the molecular hydrogen in the atmospheres of cool stars and brown dwarfs limits the accuracy of cool star modelling. The phenomenon is more significant for strong lines than for weak ones as the strengths of weak absorption lines are determined more by the Doppler-dominated line core than by the Lorentzian wings. Nevertheless, because of their very great numbers, and line blanketing considerations, line profiles need to be correctly defined for the very large number of weak lines as well as for the strong transitions (Ryan, 1998).

Pressure broadening (and shifts) arise from collisions which couple nearby states. These couplings obey dipole selection rules. Previous methods have used models to give these couplings but N.N. Lavrentieva (Institute of Atmospheric Optics, Russian Academy of Science, Tomsk) is using BT2, which should give much better results. Based on her work, we plan to include line broadening parameters in our line list.

10.5 Non-LTE modelling of Betelgeuse

Water has been detected in the spectra of early M supergiants (Jennings and Sada, 1998; Tsuji, 2000; Ryde et al., 2006). However the origin of the water absorption features is not properly understood. Synthetic spectra based on a spherical hydrostatic model photosphere with T_{eff}=3 600 K (the one normally assumed for this class of star), fail to model the observed lines (Ryde et al., 2006). It has been suggested (Tsuji et al.,1997a, 1997b; Matsuura et al., 1999; Tsuji, 2000) that in the case of M supergiants, such as Betelgeuse, the H_2O absorption features are formed in a stationary warm envelope situated above the photosphere, but inside the cool, expanding circumstellar region. Tsuji (2000) calls this region containing H_2O vapour the 'MOLsphere'. However, the MOLspere hypothesis is not universally accepted. It is suggested by Ryde et al. (2006), that the observed lines may be photospheric in origin and Ryde et al. demonstrate that a better synthetic fit can be achieved by assuming a photospheric temperature of T_{mod}=3 250 K.

One likely reason why synthetic spectra have failed to reproduce the observed water features in Betelgeuse is that the water-containing regions are not in LTE

as the number densities are too low. In order to resolve the uncertainty about the nature of the region where water absorption is occurring, it is necessary to produce a non-LTE model of the evolved envelope around Betelguse.

The author has agreed to collaborate with G.M. Harper of the Center for Astrophysics and Space Astronomy (CASA), Boulder, Colorado, N. Ryde of Université Montpellier, France and Jonathan Tennyson in producing an appropriate non-LTE model. This model will include the BT2 data, but will require major statistical analysis to compute the intensities of transitions from levels that are not populated in accordance with a Boltzmann distribution.

10.6 Temperature scale for M dwarfs

Although the IMF is not accurately constrained, it is undoubtedly the case that low mass stars (LMS), defined as stars with a mass < 0.8 $M_{\odot}$, account for a substantial proportion (probably in excess of 50% by number) of all the stars in our stellar neighbourhood. Despite this, the effective temperatures of LMS are not well determined. In particular, there is not a close correlation between spectral type and effective temperature. Improved data on the effective temperatures of LMS are required in order to better understand and define the boundary between stellar and sub-stellar objects, which will in turn give a better understanding of main sequence stellar evolution.

We plan to collaborate with S. Viti of UCL in using BT2 to derive an effective temperature scale for M dwarfs. We have been awarded observing time on Gemini North to obtain high resolution spectra of M dwarfs in the 12 μm region using the Texas Echalon Cross Echelle Spectrograph (TEXES), a 'special visiting instrument' on Gemini in the 2006b semester. We will obtain spectra of 3 M dwarfs spanning a range of spectral classes M2 to M7 on three nights in November using two grating positions: 11.17–11.22 μm and 12.46–12.54 μm at a resolution of $\sim$80 000.

These spectra will be examined for pure rotational transitions, using synthetic spectra generated with BT2. We calculate that we will be able to identify approximately 35 H_2O rotational transitions in each of the two spectral regions, which will provide a statistically significant number of lines of varying intensities.

In order to construct a scale of effective temperature, it will be necessary to combine spectral analysis and assignments with estimates of line strengths obtained using BT2 in PHOENIX models (see Section 7.4.2) of LMS. In this, and in other projects concerned with stellar atmospheric modelling, we plan to collaborate with P. Hauschildt of Hamburger Sternwarte, the University of Hamburg.

Bibliography

A'Hearn M.F., Belton M.J.S., Delamere W.A., Kissel J., Klaasen K.P., et al., 2005, Science 310, 258

Alexander D.R., Ferguson J.W., Tamanai A., Bodnarik J., Allard F., Hauschildt P.H., 2003, in Hubeny I., ASP Conf. Series, 288, 289

Allard F., Hauschildt P.H., Miller S., Tennyson J., 1994 ApJ, 426, L39

Allard F., Hauschildt P.H., 1995, ApJ, 445, 433

Allard F., Hauschildt P.H., Baraffe I., Chabrier G., 1996 ApJ, 465, L123

Allard F., Hauschildt P.H., Schwenke D., 2000, ApJ, 540, 1005

Allard F., Guillot T., Ludwig H-G., Hauschildt P.H., Schweitzer A., Alexander D.R., Ferguson J.W., 2003, IAU Symposium, ed. Martín E.L, Vol. 211, 325

Allen P.R., Koerner D.W., Reid I.N., Trilling D.E., 2005, ApJ, 625, 385

Asplund M., Grevesse N., Sauval A.J., 2005, ASP Conference Series, Vol 336, ed: Barnes III, T.G., Bash F.N.

Bačić Z., Light J.C., 1989, Annu. Rev. Phys. Chem., 40, 469

Banerjee D.P.K., Ashok N.M., 2002, A&A, 395, 161

Banerjee D.P.K., Varricatt W.P., Ahok N.M., Launila O., 2003, ApJ, 598, L31

Banerjee D.P.K, Ashok N.M., 2004, ApJ, 604, L57

Banerjee D.P.K., Barber R.J. Ashok N.M., Tennyson J., 2005, ApJ, 627, L141

Banerjee D.P.K., Su K.Y.L., Misselt K.A., Ashok N.M., 2006, 'Spitzer observations of V838 Mon: Detection of a rare infrared light echo' (submitted)

Baraffe I., Chabrier G., Allard F., Hauschildt P., 1998, A&A, 337, 403

Barber R.J., Harris G.J., Tennyson J., 2002, J. Chem. Phys., 117, 11239

Barber R.J., Tennyson J., Harris G.J., Tolchenov R., 2006a, MNRAS, 368, 1087

Barber R.J., Banerjee D.P.K., Ashok N.M., Tennyson J., 2006b, 'Measurement of temperature and H_2O column density of V838 Mon., using the BT2 line list' ASP Conference Series (V838 Mon.) ed. Corradi R.L.M.C & Munari U., (submitted)

Barber R.J., Miller S., Stallard T.S., Tennyson J. et al., 2006c, 'UKIRT Deep Impact obsesrvations: light curve, ejecta expansion rates and water spectral features' Icarus, (in press)

Barber R.J., Jones H.R.A., Hauschildt P., Tennyson J., 2006d, (in preparation)

Barber R.J., Miller S, Stallard T.S., Tennyson J., 2006e, 'The BT2 water line list reveals interesting changes in the post-impact near IR spectrum' Springer-Verlag ESO Astrophysics Symposia Series (Deep Impact as a World Observatory Event - Synergies in Space, Time), ed. Ulrich Käufl H., & Sterken S., (in press)

Barletta P., 2002, Ph.D. Thesis, University of London.

Barlow M.J., et al., 1996 A&A, 315, L241

Baron E., Hauschildt P.H., Branch D., 1994, ApJ, 426, 334

Beardsworth R., Bunker P.R., Jensen P., Kraemer W.P., 1986, J. Mol. Spectrosc., 118, 50

Bensch F., Melnick G.J., Neufeld D.A., Harwit M., Snell., R.L., Patten B.M., 2006, 'Submillimeter Wave Astronomy Satellite observations of comet 9P/Tempel 1 and Deep Impact' Springer-Verlag ESO Astrophysics Symposia Series (Deep Impact as a World Observatory Event - Synergies in Space, Time), ed. Ulrich Käufl H., & Sterken S. (submitted)

Bernath P.F., 1996, Chem. Soc. Rev., 25, 111

Bernath P.F., 2002, Phys. Chem. Chem. Phys., 4, 1501

Bernath P.F., 2005, , 'Spectra of Atoms and Molecules', second ed., OUP.

Betz A.L., McLaren R., Spears, D.L., 1979, ApJ., 229, L97

Bird M.K., Janardhan P., Wilson T.L., Huchtmeier W.K., Gensheimer P., Lemme C., 1999, Earth Moon and Planets, 78, 21

Blackwell D.E., Calamai G., Willis R.B., 1972, MNRAS, 160, 121

Bond H.E., Henden A., Levay Z.G. et al., 2003, Nature, 422, 405

Born M., Oppenheimer R., 1927, Ann. Phys., 84, 457

Brown N.J., 2002, IAU Circ, 7785

Bunker P.R., Jensen P., 2005, 'Fundamentals of Molecular Symmetry', IoP Series in Chemical Physics

Burch D.E., France W.L., Williams D., 1963, Appl. Opt., 2, 585

Burgasser A., Kirkpatrick J.D., Cutri R.M., McCallon H., Kopan G., Gizis J.E., et al., 2000, ApJ, 531, L57

Burgasser A., 2002, Ph.D. Thesis, California Institute of Technology

Burrows A., Marley M., Hubbard W.B., Lunine J., Guillot T., et al., 1997, ApJ, 491, 856

Burrows A., Marley M.S., Sharp C.M., 2000, ApJ, 531, 438

Burrows A., Hubbard W.B., Lunine J.I., Liebert J., 2001, Rev. Mod. Phys., 73, 719

Burrows A., Sudarsky D., Lunine J.I., 2003, ApJ., 596, 587

Bykov A.D., Lavrentieva N.N., Sinitsa L.N., 2004, Mol. Phys. 102, 1653

Camy-Peyret C., Flaud J.-M., Maillard J.-P., Guelachvili G., 1977, Mol. Phys., 33, 1641

Carr J.S., Tokunaga A.T., Najita J., 2004, ApJ, 603, 213

Carter S., Handy N.S., 1987 J. Chem. Phys., 87, 4294

Cernicharo J., González-Alfonso E., Alcolea J., Bachiller R., John D., 1994, ApJ, 432, L59

Chabrier G., Baraffe I., 1997, A&A, 327, 1054

Chabrier G., Baraffe I., Allard F., Hauschildt P., 2000, ApJ., 542, L119

Cheung A.C., Rank D.M., Townes C.H., Thornton D.D., Welch W.J., 1969, Nature, 221, 626

Child M.S., Halonen L., 1984, Adv. Chem. Phys., 57,1

Child M.S., Weston T., Tennyson J., Mol. Phys., 96, 371

Coheur P.-F., Bernath P.F., Caleer M., Colin R., et al., 2005, J. Chem. Phys., 122, 074307

Collinge M.J., Knapp G.R., Fan X., Lupton R.H., Narayanan V., et al., 2002, AAS, 34, 1125

Crause L.A., Lawson W.A., Warrick A., Dilkenny D., van Wyk F., Marang F., Jones A.F., 2003, MNRAS, 341, 785

Császár A.G., Kain J.S., Polyansky O.L., Zobov N.F., Tennyson J., 1998a, Chem. Phys. Let., 293, 317

Császár A.G., Allen W.D., Schaefer H.F. III, 1998b, J. Chem. Phys., 108, 9751

Darling B.T., Dennison D.M., 1940, Phys. Rev., 57, 128

Delfosse X., Tinney C.G., Forveille T., Epchtein N., et al., 1997, A&A, 327, L25

Dickinson A.S., Ceratin P.R., 1968, J. Chem. Phys., 49, 4209

Dello Russo N., Mumma M.J., DiSanti M.A. Magee-Sauer K., Novak R., Rettig T.W., 2000, Icarus, 143, 324

Dello Russo N., DiSanti M.A., Magee-Sauer K., Gibb E.L., Mumma M.J., Barber R.J., Tennyson J., 2004, Icarus, 168, 186

Dello Russo N., Bonev B.P., DiSanti M.A., Mumma M.J., Gibb E.L., Magee-Sauer K., Barber R.J., Tennyson J., 2005, ApJ, 621, 537

Desidera S., et al., 2004, A&A, 414, 591

Dodeldon S., 1986, J.Phys. B, 19, 2871

Duncan M., Levison H., Dones L., 2005, in 'Comets II', ed. Festu M., Keller H.U., Weaver H.A., Univ. Arizona Press, pp 153-174

Dupré P., Gherman T., Zobov N.F., Tolchenov R.N., Tennyson J., 2005, J. Chem. Phys, 123, 154307

EPAPS Document No. E-JCPSA6-122-010506
(http://www.aip.org/pubservs/epaps.html)

Epchtein N., 1997, in 'The impact of large-scale near-infrared surveys', Garzón, Epchtein N., et al. eds., Kluwer, Dordrecht, p25

Evans A., Geballe T.R., Rushton M.T., Smalley B., et al., 2003, MNRAS, 343, 1054

Feldman P.D., Weaver H.A., A'Hearn M.F., Belton M.J.S., Meech K.J., 2005, Bull. A. Astron. Soc., 37.3, 42.04

Ferguson J.W., Alexander D.R., Allard F., Barman T., Bodnarik J.G., Hauschildt P.H., Heffner-Wong A., Tamanai A., 2005, ApJ, 623, 585

Firriso C.C., Ludwig C.B., 1964, J. Ghem. Phys., 41, 1668

Ferriso C.C., Ludwig C.B., Thomson A.L., 1966, J. Quant. Spectrosc. Radiat. Transfer, 6, 241

Flaud J.-M., Camy-Peyret C., Maillard J.-P., 1976, Mol. Phys., 32, 499

Fulton N.G., 1994, Ph.D. Thesis, University of London

Geballe T.R., Kulkarni S.R., Woodward C.E., Sloan G.C., 1996, ApJ, 467, L101

Gensheimer P.D., Mauersberger R., Wilson T.L., 1996, A&A, 314, 281

González-Alfonso E., Cernicharo J., Bachiller R., Fuente A., 1995, A&A, 293, L9

Gurtovenko E.A., Kondrashova N.N., 1980, Solar Phys., 68, 17

Gustaffson M., Frommhold L, 2001, ApJ 546, 1168

Halonen L., 1998, Adv Chem Phys. 104, 41

Handy N.C., Yamaguchi Y., Schaefer III H.F., 1986, J. Chem. Phys., 84, 4481

Handy N.C., Lee A.M., 1996, Chem. Phys. Let., 252, 425

Handy N.C., Carter S., Colwell S.M., 1999, Mol. Phys., 96, 477

Harris G.J., 2002, Ph.D. Thesis, University of London

Hauschildt P.H., Starrfield S., Austin S., Wagner R.M., Shore S.N., Sonneborn G., 1994, ApJ, 422, 831

Hauschildt P.H., Allard F., Baron E., 1999, ApJ, 512, 377

Henden A., Munari U., Schwartz M., 2002, IAU Circ., 7859

Hinkle K.H., Barnes T.G., 1979, ApJ, 227, 923

Ho P., Townes C.H., 1983, Ann. Rev., A&A, 21, 239

Hottel H.C., Smith V.C., 1935, Trans. Amer. Soc. Mech. Engrs., 57, 463

Hoy A.R., Mills I.M., Strey G., 1972, Mol. Phys., 24, 1265

Jennings D.E., Sada P.V., 1998, Science, 279, 844

Jensen P., 1988, J. Mol. Spec., 132, 429

Jensen P., 2000, Mol. Phys., 98, 1253

Jones H.R.A., Longmore A.J., Jameson R.F., Mountain C.M., 1994, MNRAS, 267, 413

Jones H.R.A., Longmore A.J., Allard F., Hauschildt P.H., Miller S., Tennyson J., 1995, MNRAS, 277, 767

Jones H.R.A., Pavlenko Y., Viti S., Tennyson J., 2002, MNRAS, 330, 675

Jones H.R.A., Pavlenko Y., Viti S., Tennyson J., 2003 in 'Proceedings of 12th Cambridge Workshop on Cool Stars', eds. Brown A., Harper G.M., Ayres T.R., p899

Jones H.R.A., Pavleko Y., Viti S., Barber R.J., Yakovina L.A., Pinfield D., Tennyson J., 2005a, MNRAS, 358, 105

Jones H.R.A., Viti S., Tennyson J., Barber R.J., Harris G. et al., 2005b, Astron. Nachr., 326, 920

Jørgensen U.G., 1994a, A&A, 284, 179

Jørgensen U.G., 1994b, in 'Molecules in the Stellar Environment' (Springer), p29

Jørgensen U.G., 1997, Proceedings of IAU: 'Molecules in Astrophysics:Probes and Processses' ed. van Dishoeck F.E., 441

Jørgensen U.G., Jensen P., Sørensen G.O., Aringer B., 2001, A&A, 372, 249

Kain J.S., Polyansky O.L., Tennyson J., 2000, Chem. Phys. Let., 317, 365

Kaminsky B.M., Pavlenko Y.V., 2005, MNRAS, 357, 38

Kawakita H., Dello Russo N., Furusho R., Fuse T., Watanabe J-I., et al., 2006., ApJ, 643, 1337

Kedziora G.S., Shavitt I., 1997, J. Chem. Phys., 106, 8733

Kirkpatrick J.D., Reid I.N., Liebert J, Cutri R.M., Nelson B., 1999, ApJ, 519, 802

Kipper T., et al., 2004, A&A, 416, 1107

Kozin I.N., Law M.M., Tennyson J., Hutson J.M., 2004, Comp. Phys. Comm., 163, 117

Kupka F., Piskunov N.E., Ryabchikova T.A., Stempels H.C., Weiss W.W., 1999, A&AS, 138, 199

Kurucz R.L., 1970, Smithsonian Astrophysical Observatory, Special Report: 309

Kutzelnig W., 1997, Mol. Phys., 90, 909

Lançon A., Rocca-Volmerange B., 1992, A&AS, 96, 593

Lane B.F., Retter A., Thompson R.R., Eisner J.A., 2005, ApJ, 622, L137

Larsson B., Liseau R., Bergman P., Bernath P. et al., 2003, A&A, 402, L69

Le Teuff Y.H., Millar T.J., Markwick A.J., 2000, 'UMIST Database for Astrochemistry, 1999' A&A Supp. Ser. 146, 157

Leggett S.K., Golimowski D.A., Fan X., Geballe T.R., Knapp G.R., et al., 2002a, ApJ, 564, 452

Leggett S.K., Hauschildt P.H., Allard F., Geballe T.R., Baron E., 2002b, MNRAS, 332, 78

Lin H., Thiel W., Yurchenko S., Carvajal M., Jensen P., 2002, J. Chem. Phys., 117, 11265

Liseau R., Larsson B., Brandeker A., Bergman P., et al., 2003, A&A, 402, L73

Lodieu N., McCaughrean M.J., Barado y Navascués D., et al., 2005, A&A, 436, 853

Lucas P.W., Roche P.F., Tamura M., 2005, MNRAS, 361, 211

Ludwig C.B, 1971, Appl. Opt., 10, 1057

Lynch D.K., Rudy R.J., Russell R.W., Mazuk S., et al., 2004, ApJ, 607, 460

Lynas-Gray A.E., Miller S.,Tennyson J., 1995 J. Mol. Spec., 169, 458

Lyubchik Y., Jones H.R.A., Pavlenko Y.V., Martín E., Mclean I., Prato L., Barber R.J., Tennyson J., 2006, 'Spectral analysis of high resolution near-infrared spectra of ultracool dwarfs', A&A (in press)

Magazzù A., Martín E., Rebolo R., 1991, A&A 249, 149

Marley M.S., Saumon D., Guillot T., Freedman R.S., Hubbard W.B., Burrows A., Lunine J.I., 1996, Science, 272, 1919

Marley M.S., 2001, ASP Conference Series, eds.: Jayawardhana R., Greene T.P., 244, 316

Marquardt R., Sagui K., Klopper W., Quack M., 2005, J. Phys. Chem. B 109, 8439

Martín E., Delfosse X., Barsi G., Goldman B., Forveille T., 1999, AJ, 118, 2466

Matsuura M., Yamamura I., Murakami H., Freund M.M., Tanaka M., 1999, A&A, 348, 579

Matthews K., Nakajima T., Kulkarni S.R., Oppenheimer B.R., 1996, AJ, 112, 1678

McCaughrean M.J., Close L.M., Scholz R.-D., Lenzen R., Biller B., et al., 2004, A&A, 413, 1029

Meech K.J., Ageorges N., A'Hearn M.F., Arpingy C., et al., 2005, Science, 310, 265

Miani A., Tennyson J., 2004, J. Chem. Phys., 120, 2732

Miller S., Tennyson J., Jones H.R.A., Longmore A.J., 1994, in Proc. IAU Symp. 146, 'Molecules in the stellar environment', ed. Thejll P., Jørgensen U.G, Springer-Verlag, Berlin.

Moont B., 2005, 'A spectroscopic analysis of the 11 μm region for M stars', MSci report, University College London.

Morbidelli A., Brown M.E., in 'Comets II', ed. Festu M., Keller H.U., Weaver H.A., Univ. Arizona Press, Tuscon, pp 175-191

Mumma M.J., Blass W.E., Weaver H.A., Larson H.P., 1983, in 'Formation and Evolution of Planetary Systems' ed., Weaver H.A., Danly L. (CUP), 157

Mumma M.J., Weissman P.R., Stern S.A., 1993, 'Protostars and Planets' III, ed., Levy E.H. & Lunine J.I. (Univ. Arizona Press, Tuscon), 1177

Mumma M.J., DiSanti M.A., Dello Russo N., Fomenkova M., Magee-Sauer K., Kaminski C.D., Xie D.X., 1996, Science 272 1310

Mumma M.J., DiSanti M.A., Magee-Sauer K., Bonev B.P., Villanueva G.L. Kawakita H., et al., 2005, Science, 310, 270

Munari U., et al, 2002, A&A, 389, L51

Mussa H.Y., Tennyson J., 1998, J. Chem. Phys., 109, 10885

Nela N., Permogorov D., Miani A., Halonen L., 2000, J. Chem. Phys., 113, 1795

Neale L., Miller S., Tennyson J., 1996, ApJ, 464, 516

Noll K.S., Geballe T.R., Leggett S.K., Marley M.S., 2000, ApJ, 541, L75

Opacity Project Team, 'The Opacity Project', 1995, IoP Publishing.

Oppenheimer B.R., Kulkarni S.R., Matthews K., Natajima T., 1995, Science 270, 1478

Oppenheimer B.R., Kulkarni S.R., Matthews K., van Kerkwijk M.H., 1998, ApJ, 502, 932

Partridge H., Schwenke D.W., 1997, J. Chem. Phys., 106, 4618

Pavlenko Y.V., 2000, Astron. Rept., 44, 219

Pavlenko Y.V., Zapatero Osorio M.R., Rebolo R., 2000, A&A, 355, 245

Pavlenko Y.V., Geballe T.R., 2002, A&A, 390, 621

Pavlenko Y.V., 2003, Astron. Rept. 47, 59

Pavlenko Y.V., van Loon J.T., Evans., A., Rushton M., et al., 2006, A&A (in press)

Pinfield D.J., Jones H.R.A, Lucas P.W., Kendall, T.R., Folkes S.L., Day-Jones A.C., Chappelle R.J., Steele I.A., 2006, MNRAS, 368, 1281

Pinfield D.J. and 'Cool Dwarf Science Working Group', Gemini South observing proposal, 2006B semester

Polyansky O.L., Jensen P., Tennyson J., 1994, J. Chem. Phys., 101, 7651

Polyansky O.L., Jensen P., Tennyson J., 1996, J. Chem. Phys., 105, 6490

Polyansky O.L., Zobov N.F., Viti S., Tennyson J., Bernath P.F., Wallace L, 1997a, J. Mol. Spec., 186, 422

Polyansky O.L., Zobov N.F., Viti S., Tennyson J., Bernath P.F., Wallace L, 1997b, ApJ, 489, L205

Polyansky O.L., Zobov N.F., Viti S., Tennyson J., Bernath P.F., Wallace L, 1997c, Science, 277, 346

Polyansky O.L., Tennyson J., Bernath P.F., 1997d, J Mol Spec, 186, 213

Polyansky O.L., Zobov N.F., Viti S., Tennyson J., 1998, J. Mol. Spec., 189, 291

Polyansky O.L., Tennyson J., Zobov N.F., 1999, Spectrochimica Acta Part A, 55, 659

Pyykkö P., Dyall K.G., Császár A.G., Tarczay G., Polyansky O.L., Tennyson J., 2001, Phys. Rev. A., 63, 24502

Rajamäki T., Kállay M., Noga J., Valiron P., Halonen L., 2004, Mol. Phys., 102, 2297

Rawlings J.M.C., Barber R.J., Tennyson J, 2006, (in preparation)

Rose J.P., Kellman M.E., 1994, J. Chem. Phys., 105, 7348

Reid I.N., Gizis J.E., Hawley S.L., 2002, AJ, 124, 2721

Retter A., Marom A., 2003, MNRAS, 345, L25

Retter A., Zhang B., Siess L., Levinson A., 2006, 'The planets capture model of V838 Mon: conclusions for the penetration depth of planet/s', MNRAS (submitted)

Ryan S.G., 1998, A&A, 331, 1051

Ryde N., Lambert D.L., Richter M.J., Lacy J.H., 2002, ApJ, 580 447

Ryde N., Harper G.M., Richter M.J., Greathouse T.K., Lacy J.H., 2006, ApJ, 637, 1040

Saltpeter E.E., 1955, ApJ 121, 161

Saumon D., Geballe T.R., Leggett S.K., Marley M.S., Freedman R.S., et al., ApJ, 541, 374

Scholz R.D., McCaughrean M.J., Lodieu N., Kuhlbrodt B., 2003, A&A, 398, L29

Schryer J.J., Miller S., Tennyson J., 1995, J. Quant. Spectrosc. Radiat. Transfer, 53, 373

Schultz P.H., Ernst C., A'Hearn M.F., Eberhardy C., Sunshine J.M., et al., 2006, 37th Annual Lunar and Planetary Science Conference (League City, Texas), abstract no. 229

Schwenke D.W., 1998, Faraday Discussion, 109, 321

Schwenke D.W., Partridge H., 2000, J. Chem. Phys., 113, 6592

Schwenke D.W., 2001, J. Phys. Chem., 2001, 105, 2352

Schwenke D.W., 2003, J. Chem. Phys., 118, 6898

Shiba H., Sato S., Yamashita T., Kobayashi Y., Takami H., 1993, ApJ Sup., 89, 299

Shirin S.V., Polyansky O.L., Zobov N.F., Barletta P., Tennyson J., 2003, J. Chem. Phys., 118, 2124

Skrutskie M.F, Cutri R.M., Stiening R., Weindberg M.D., Schneider S., et al., 2006, AJ, 131, 1163

Smith P.L., Yoshino K., Greisinger H.E., Black J.H., 1981, ApJ, 250, 166

Smith V.V., Tsuji T., Hinkle K.H., Cunha K., et al., 2003, ApJ, 582, L105

Soker N., Tylenda R., 2003, ApJ, 582, L105

Soker N., Tylenda R., 2006, 'Modelling V838 Monocerotis: Discussion' ASP Conference Series, Ed. Corradi R.L.M., Munari U. (submitted)

Sparks W.B., 2005, ASP Conference Series, 343, 452

Stern S.A., 2003, Nature, 424, 639

Sutcliffe B.T., Tennyson J., 1986, in 'International Journal of Quantum Chemistry:Quantum Chemistry Symposium' (Wiley)

Sutcliffe B.T., Tennyson J.,1987, J. Chem. Soc. Faraday Trans., 83, 1663

Sutcliffe B.T., 1999, Int. J. Quantum. Chem.,74, 681

Tarczay G., Császár A.G., Klopper W., Quiney H.M., 2001, Mol. Phys., 99, 1769

Tennyson J., Sutcliffe B.T., 1982, J. Chem. Phys., 77, 4061

Tennyson J., 1992, J. Chem. Soc. Faraday Transactions, 88, 3271

Tennyson J., Sutcliffe B.T., 1992, Int. J. Quant. Chem., 42, 941

Tennyson J., Henderson J.R., Fulton N.G., 1995, Computer Physics Communications, 86, 175

Tennyson J., Zobov. N.F., Williamson R., Polyansky O.L., Bernath P.F., 2001, J. Phys. Chem. Ref. Data, 30, 735

Tennyson J., Barletta P., Kostin M.A., Polyansky O.L. Zobov N.F., 2002 Spectrochimica Acta A, 58, 663

Tennyson J., Kostin M., Barletta P., Harris G.J., Poyansky O.L., Ramanlal J., Zobov N.F., 2004, Comp. Phys. Comm., 163, 85

Tennyson J., 2006a, Physica Scripta, (Royal Swedish Academy of Sciences), 73, 1

Tennyson J., Harris G.J., Barber R.J., La Delfa S., Voronin B.A., Kaminsk B.M., Pavlenko Y.V., 2006b, Mol. Phys. (submitted)

Tielens A.G.G.M., Allamandola L.J., 1987, in 'Interstellar Processes' ed., Hollenbach D.J., Thronson Jr. H.A. (Dordrecht: Reidel), p397

Tolchenov R.N. et al., 2005, J. Mol. Spec., 233, 68

Tourin R.H., Henry P.M., 1959, AFCRC-TR-60-203, The Warner and Swasey Company, Control Instrument Division

Tsuji T., 1986, Ann. Rev. Astrophys., 24, 89

Tsuji T., 1995, ASP Conference Series, ed. Sauval A.J. et a., 81, 566

Tsuji T., Ohnaka K., Aoki W., Nakajima T, 1996a, A&A, 308, L29

Tsuji T., Ohnaka K., Aoki W., Nakajima T, 1997a, A&A, 320, L1

Tsuji T., Ohnaka K., Aoki W., Yamamura I., 1997b, Ap&SS, 255, 293

Tsuji T., 2000, ApJ, 538, 801

Tsuji T., 2001, A&A, 376, L1

Tsuji T., 2002, ApJ, 575, L26

Tylenda R., 2004, A&A, 414, 223

Tylenda R., 2005 A&A, 436, 1009

Tylenda R., Soker N., Szczerba R., 2005, A&A, 441, 1099

Van Loon J.T., Evans A., Rushton M.T., Smalley B., 2004, A&A, 438, 273

Vidler M., Tennyson J., 2000, J. Chem Phys. 113, 9766

Villanueva G.L., Bonev B.P., Mumma M.J., DiSanti M.A., Magee-Sauer K., 2006, 'Infrared spectral survey of the ejecta of comet Tempel 1 using NIRSPEC/Keck-2' Springer-Verlag ESO Astrophysics Symposia Series (Deep Impact as a World Observatory Event - Synergies in Space, Time), ed. Ulrich Käufl H., & Sterken S. (in preparation)

Viti S., Tennyson J., Polyansky O.L., 1997, MNRAS, 287, 79

Viti S., 1997, Ph.D. Thesis, University of London

Volk K., Blum R., Walker G., Puxley P., 2003, IAU Circ. 8188

Wallace L., Bernath P., Livingston W., Hinkle K., Busler J., Guo B., Zhang K.-Q., 1995, Science, 268, 1155

Wallace L., Livingston W., 1992, An Atlas of a Dark Sunspot Umbral Spectrum. (Nat. Optical Astron. Observatories, Tucson, AZ)

Wisniewski J.P., Bjorkman K.S., Magalhães A.M, 2003, ApJ598, L43

Yeomans D.K., 2005, 'Comet' World Book Online Reference Center, World Book Inc., http://www.worldbookonline.com/wb/Article?id=ar125580

Yurchenko S.N., Thiel W., Carvajal M., et al., 2005a, Adv. Quant. Chem., 48, 209

Yurchenko S.N., Caravajal M., Lin H., et al., 2005b J. Chem. Phys., 122, 104317

Zeninari V., Parvitte B., Courtois D., Lavrentieva N.N., Ponomarev Y.N., Durry G., 2004, Mol. Phys. 102 (16-17), 1697

Zobov N.F., Polyansky O.L., Le Sueur C.R., Tennyson J., 1996, Chem. Phys. Lett. 260, 381

Zobov N.F., Polyansky O.L., Tennyson J., Lotoski J.A., Colarusso P., Zhang K-Q., Bernath P.F., 1999, J. Mol. Spec., 193, 188

Zobov N.F., Polyansky O.L., Savin V. A., Shirin S.V., 2000a, Atmos. Oceanic Opt.,13, 1024

Zobov N.F., Belmiloud D., Polyansky O.L., Tennyson J., 2000b, J. Chem. Phys., 113, 1546

Zobov N.F., Shirin S.V., Polyansky O.L., Barber R.J., et al., 2006, J. Mol. Spec, 237, 115